January 2018

Effects Of Friction Stir Welding Parameters On The Mechanical Properties Of Am60 And Al-Si Cast Alloys

Sara Richmire-Kint

EFFECTS OF FRICTION STIR WELDING PARAMETERS ON THE MECHANICAL PROPERTIES OF AM60 AND AL-10%SI CAST ALLOYS

by

Sara Elizabeth Richmire-Kint
Bachelor of Science, University of North Dakota, 2006
Master of Business Administration, University of Phoenix, 2010

A Thesis
Submitted to the Graduate Facility

of the

University of North Dakota

in partial fulfillment of the requirements

for the degree of

Master of Science

Grand Forks, North Dakota

August
2018

This thesis, submitted by Sara Richmire-Kint in partial fulfillment of the requirements for the Degree of Master of Mechanical Engineering from the University of North Dakota, has been read by the Faculty Advisory Committee under whom the work has been done and is hereby approved.

_____
Dr. Meysam Haghshenas

_____
Dr. Clement Tang

_____
Dr. Cai Xia Yang

This thesis (or dissertation) is being submitted by the appointed advisory committee as having met all of the requirements of the School of Graduate Studies at the University of North Dakota and is hereby approved.

_____
Grant McGimpsey
Dean of the School of Graduate Studies

_____
Date:

PERMISSION

Title Effects of Friction Stir Welding Parameters on the Mechanical Properties of AM60 and AL-10%Si Cast Alloys

Department Mechanical Engineering

Degree Master of Science

In presenting this thesis in partial fulfillment of the requirements for a graduate degree from the University of North Dakota, I agree that the library of this University shall make it freely available for inspection. I further agree that permission for extensive copying for scholarly purposes may be granted by the professor who supervised my thesis work or, in her (or his) absence, by the Chairperson of the department or the Dean of the School of Graduate Studies. It is understood that any copying or publication or other use of this thesis or part thereof for financial gain shall not be allowed without my written permission. It is also understood that due recognition shall be given to me and to the University of North Dakota in any scholarly use which may be made of any material in my thesis.

Sara Richmire-Kint
7/23/201

TABLE OF CONTENTS

LIST OF FIGURES

Figure Page

LIST OF TABLES

Table Page

ACKNOWLEDGMENTS

I wish to express my sincere appreciation to:

Assistant Prof. Dr. Meysam Haghshenas, my supervisor, for his continual support throughout my study, the insightful discussion on my research, and for his unwavering patience and motivation.

The members of my advisory Committee, Dr. Yang and Dr. Tang, for their time, guidance and support during my time in the master's program at the University of North Dakota.

My professors in the School of Engineering and Mines at the University of North Dakota for all the aid and support I received during my masters.

ND EPSCoR and the Department of Mechanical Engineering at UND for giving me financial support throughout my graduate studies.

The members of my research group, Muztahid, Rezwana and Farwan, for their assistance, teamwork and insightful discussions.

My parents, Barbara and Clarke, for all their love and support through the years. Without their sacrifices I wouldn't have been able to get to this stage in my life.

And finally, my husband, Kristian, his unending support, level-headedness and love helped me through all hard days and long hours; I wouldn't have completed this journey without him.

To Killian and Kodi, you are the future.

ABSTRACT

Friction stir welding, as a solid-state joining method, seems a viable joining/assembly method for difficult-to-weld cast magnesium and cast aluminum alloys. Due to the high flammability of Mg alloys, and the brittle joints of welded Al alloys, fusion based welding techniques may not be successful to join Mg or Al made component. Therefore, a solid-state operation, in which applied heat input and induced temperature within the work piece are below the melting temperature of the base alloys, can be considered as a viable method to join so-called unweldable Mg and Al alloys. To this end, friction stir welding, as one of the most common solid-state joining and processing methods, has been extensively studied for similar/dissimilar welding of different grades of magnesium alloys.

In this thesis, the effects of FSW parameters (*i.e.* tool traverse speed and tool rotational speed) have been examined on two different cast alloys with particular focus on microstructure, hardness distribution and fatigue life:

i) AM60 as-cast magnesium alloy

ii) Al-10%Si as-cast hypoeutectic aluminum alloy

The influence of different processing parameters has been explored at a vital level. Hardness and fatigue testing were performed to determine how the changes in parameters influence the mechanical properties. Fractography was carried out on the fatigue fracture surface to determine the means of failure and crack initiation points; optical microscopy

and scanning electron microscopy were performed on the FSW joint to observe the microstructural changes with varying weld parameters.

Upon the FSW process, the microstructure of both alloys was greatly refined due to the severe plastic deformation imposed by the rotating tool. The hardness for the AM60 Mg alloy was higher in the SZ, compared with the base metal, while for the Al-10%Si alloy the hardness value was lower in the SZ than the parent materials with the lowest value being seen in the HAZ and TMAZ.

The resulting stress amplitude vs. cycles to failure (S-N) curves show an increase in fatigue life with a decrease in stress amplitude. SEM fracture surface observations show crack initiation occurring from the imperfections on the surface and internally. The fracture for AM60 was a combination of both brittle and ductile while the Al-Si10% alloy showed pure ductile fracture (collection of dimples on the fracture surface). The fracture surfaces also exhibited features unique to fatigue failure, including fatigue striations and beach marks

In Chapter V a summary of the present work along with recommended future research have been provided. Also, various properties of the FSWed AM60 have been compared against those of FSWed Al-10%Si alloy and the differences have been explained.

CHAPTER I

1. INTRODUCTION

1.1 Background Information and Motivation

Given the growing concern with greenhouse gas emissions, minimizing the carbon dioxide emissions, and decreasing fuel consumption in the automotive and aerospace industries, it is becoming a progressively important topic of discussion for many nations. Many industries, including the automotive and aerospace, are assessing ways to reduce the overall weight of their vehicles. There has been a shift from ferrous materials and high strength steels to lower density materials like aluminum and magnesium. Given low density and excellent mechanical strength of both magnesium and aluminum alloys, these materials give promising responses to replace steel in both aerospace and automotive vehicles to reduce the overall weight. This reduction in weight leads to lower fuel consumption and in turn lowering the impact of the carbon dioxide emissions on the environment.

One of the challenges with casting of magnesium and some aluminum products (such as Al-10%Si) is that it is not always possible or economical to cast complex parts [1]. In these cases, there needs to be a method of joining and assembly of the materials for various structural applications. However, traditional joining techniques (*i.e.* fusion-based welding) may not necessarily work on cast Mg alloys (*i.e.* AM60) and cast Al alloys (*i.e.* Al-10%Si) due to the formation of porosity in the weld zone [2, 3], microstructural changes and welding defects generated, which lead to weakening of the materials properties. Besides this, Mg is highly flammable (fairly low ignition temperature) with a large coefficient of

expansion (25.6 μm/m.K at 20 to 100 °C) [4]). On the other side, fusion welding of Al-10%Si alloy results in a brittle joint due to the presence of large density of Si in the weldment. Therefore, it is important to explore and understand the microstructure, hardness, and fatigue behaviors of the welding process to be able to use magnesium and aluminum alloys in structural applications.

It is worth mentioning that using mechanical assembly methods like bolts or rivets adds weight to the parts, taking away from the benefits of using Mg and Al as light weight material for automotive and aerospace applications [5]. Besides, mechanical fasteners create stress concentration points in the assembled structure which adversely affect the fatigue life. This leaves solid-state friction-based welding techniques (*i.e.* friction stir welding (FSW)) as a potential choice for joining cast Mg alloys like AM60 [6, 7, 8, 9] and cast Al alloys like Al-10%Si. In the solid-state techniques like friction stir welding, in which no melting occurs in the base metal(s), could be considered as effective methods for joining hard-to-weld metals (i.e. Mg and Mg alloys and Al and Al alloys).

1.2 Problem Statement and Scope of Thesis

Structural components in the aerospace and automotive industries are subjected to large cyclic loadings during their life. This makes it crucial to understand the behavior of the material under these conditions. This cyclic failure is referred to as fatigue, and fatigue failure accounts for almost 90% of all mechanical service failures of components in the automotive industry [10]. Fatigue failure is different than tensile failure or single application failures in that it happens at low stresses, normally well below the ultimate tensile strength of the material [10]. When fatigue failure occurs, it does quickly and most often without any warning which make it potentially catastrophic failure. This makes it

vital to research and understand the fatigue behaviors of materials, particularly in the automotive and aerospace industries as any failure in these industries can result in safety concerns for the occupants of the vehicles.

The vision of this research is to ultimately improve the fuel efficiency of vehicles by reducing their weight. More precisely, this research focuses on looking at two specific materials, cast magnesium alloy AM60 and cast aluminum alloy Al-10%Si and friction stir weldability of them. The purpose of this is to see if it is a viable option before looking at large scale application for the actual components in the transportation industries. The present study will evaluate the fatigue life in cyclic tensile-tensile loading-unloading, axial load-controlled conditions of friction stir welded AM60 and Al-10%Si. It will also look at understanding the correlations between fatigue life, hardness, and microstructure of the FSWed cast magnesium and aluminum alloys.

1.3 Thesis Organization

The thesis has been separated into five chapters which are as follows: The first chapter provides a short introduction to the topic and states the motivation and objectives of the work. Chapter two introduces magnesium, magnesium alloys and their physical and mechanical properties. It furthers discusses the established theories and studies regarding the effect of features on the microstructural mechanical properties. Chapter two also introduces aluminum, cast aluminum alloys and their physical and mechanical properties. It furthers discusses the established theories and studies regarding the effect of features on the microstructural mechanical properties. Chapter two describes the background of friction stir welding which was used in this study as well. Chapter three presents the various experimental methods used in this study. Chapter four describes the experimentally

observed results and correlation established between the local mechanical properties and microstructural features of as-casting AM60 magnesium alloy and Al-10%Si aluminum alloy. The experimental results were determined via Vickers hardness testing and fatigue testing. The relationship between microstructures and mechanical properties for each alloy examined are reported. Finally, Chapter 5 provides conclusions of the research results and recommendations to further understanding the relationship between microstructural features and local mechanical properties.

CHAPTER II

2 LITERATURE REVIEW

This chapter consists of four sections. The first two are to introduce magnesium and aluminum, including their physical and mechanical properties. The third part is to describe the factors that affect mechanical properties including the microstructure, grain size, porosity, and defects. The final section is to present the background of friction stir welding which was used in this study.

2.1 Magnesium

2.1.1 Physical and mechanical Properties of Magnesium

Magnesium is a metallic element which makes up 2% of the earth's crust. It is one of the most abundant elements in the earth's crust and makes up 0.13% of the Earth's ocean water making it the third most abundant mineral dissolved in the earth's sea water. Magnesium occurs naturally only in combinations with other elements such as carbon, calcium, and oxygen. Magnesium has an atomic number of 12 and the atomic weight (average mass of the atom) is 24.31 g/mol [11, 12, 13]. The physical properties of pure magnesium are shown in table 2-1.

Table 2-1: Physical properties of pure magnesium [14]

Physical Property	Density (g/cm^3)	Melting Point (^oC)	Specific Heat (Cal/g^oC)	Electrical conductivity (%IACS)	Thermal Conductivity (W/mK)	Crystal Structure	Young's Modulus (GPa)
Pure Mg	1.74	650	0.24	39	155	h.c.p	45

2.1.2 Magnesium Alloys

Like other metals, pure, unalloyed, magnesium is rarely used for engineering applications. The purpose of alloying is to improve the mechanical properties and formability of magnesium in both wrought and cast products. There are two types of magnesium alloys, the first of which has a main alloying element of Aluminum at 2 – 10%, these all contain zinc or manganese in minor quantities. These magnesium alloys are available widely, at moderate costs. They also show good mechanical properties between 95 and 120 °C, above this the properties will deteriorate as the temperature increases. The other types of magnesium alloys are those in which the magnesium is alloyed with various other elements except for aluminum. These could include rare earth, zinc, thorium, silver, and silicon. The second group also contains a small amount of zirconium which creates a fine grain structure and improves the mechanical properties of the metal [14]. Table 2-2 shows the effects of different alloying elements on the mechanical properties of magnesium.

Table 2-2: The effect of alloying elements on Magnesium [15, 16].

Alloying Element	Effect on the Mechanical Properties
Aluminum (Al)	• Increases tensile strength and hardness • Forms precipitation of intermetallic phase (Mg17Al12) • Improves castability • Increases corrosion resistance
Zinc (Zn)	• Increases tensile strength and hardness • Refines grain structure • Improves castability • Increases corrosion resistance
Manganese (Mn)	• Increases yield strength • Increase corrosion resistance while reducing the effect of iron
Silicon (Si)	• Improves creep resistance • Forms Mg_2Si particles • Increases molten metal viscosity • Reduces castability • Reduces corrosion resistance
Rare Earth Metals	• Reduces the freezing range • Increase tensile strength and hardness

2.1.3 Cast Magnesium Alloys

The development of Magnesium casting began in 1921 when Dow started to produce pistons made of magnesium. Casting of magnesium grew in popularity and became further developed through out World War II with the production of parts for aerospace, defense, and automotive application. This development was in gravity sand, permanent mold, and high-pressure die casting (HPDC). The latest technology has developed excellent castability [5] on modern magnesium alloys and the focus has been on thin-walled die casting for applications in the automotive industry. Magnesium casting has continued to expand in the automotive industry, defense, aerospace, electronics, and power tools. Currently casting is the dominant manufacturing process for magnesium components and represents approximately 98% of all structural applications of magnesium [17]

There are several unique characteristics that magnesium possesses, including solidification which give it an advantage over other cast metals including aluminum and copper. These include excellent fluidity and a low susceptibility to hydrogen porosity [17].

The most common casting method for magnesium alloys is high-pressure die casting (HPDC) [16, 17]. For this process liquid metal is injected at high speed and high pressure into a metal mold. Figure 2-1 depicts this process.

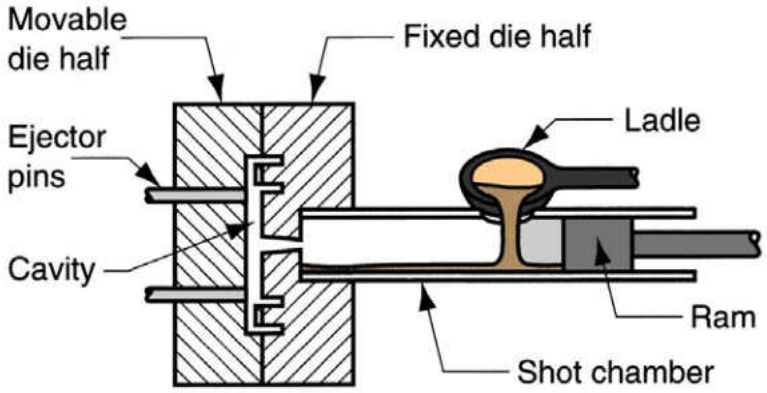

Figure 2-1: Schematic of the HPDC technique [18]

During casting of magnesium alloys the molten magnesium alloys can be held in containers made of ferrous materials; this is because the melted magnesium does not attack iron as molten aluminum does. Because of this, it is common for the magnesium alloy to be melted and transported in steel crucibles, tools and devices.

High pressure die casting is excellent for manufacturing light metal components. It provides excellent flexibility in the design and is extremely economical to produce parts though this process. Because magnesium alloys are great for die filling, the parts produced from high pressure die casting can be large, thin walled, and complexed. This allows for the replacement of steel parts, which have been made of multiple parts welded or joined together, with the solid magnesium parts. An advantage of magnesium die casting is that it can be designed with both thin and thick walls, thinner walls where the strength is not important and thicker walls where there are strength requirements. As well it is possible to cast magnesium alloys with thinner walls than aluminum alloys. As well, magnesium has a shorter casting cycle time than aluminum [17]. Table 2-3 below shows the design parameters and manufacturing characteristics for magnesium die casting.

There are two types of high pressure die casting that exist, these are hot chamber die casting and cold chamber die casting. In the automotive industry most of the magnesium die casting parts are produced by cold chamber die casting process [17].

One of the problems with casting magnesium alloys is the formation of defects (porosity and inclusions) that can happen during the casting process. These defects can act as stress concentrations which in turn can lead to crack initiation points. This can facilitate the fatigue crack initiation which in turn can reduce the life of the component and lead to a reduced cyclic strength [19].

Table 2-3: Design parameters and manufacturing characteristics for magnesium die casting [17]

Design Parameter	
Dimensional Tolerance (mm/min)	±0.001
Draft angle (°)	0–1.5
Minimum wall thickness (mm)	1–1.5
Casting/molding cycle time (unit)	1.0–1.4
Typical die life (×1000 shots)	250–300
Trimming cycle time (unit)	1
Machinability	Excellent
Welding/joining	Fair
Surface finishing	Excellent
Recyclability	Good

2.1.4 Magnesium-Aluminum Alloys

Aluminum is an alloying element used in Magnesium. Aluminum is soluble in magnesium; the solubility increases with increasing temperatures. Aluminum helps to increase the tensile strength and hardness, as well as improves the castability of the alloy and increases corrosion resistance. Aluminum also formed $Mg_{17}Al_{12}$ precipitates throughout the grain boundaries [15] which are shown in figure 2-1. Figure 2-2 below shows the phase diagram for Mg alloys. Al is soluble in Mg from 2.1 wt% at room temperature up to 12.6 wt% at the eutectic temperature of 437 ^{o}C. [15].

In the current project a cast Mg alloy (AM60) was used as one of the investigated materials. The main alloying element in AM60 Mg alloy is aluminum with the secondary alloying element being Manganese (Mn). Table 2-4 shows the nominal composition (wt%) of the AM60 alloy. The addition of aluminum increases the tensile strength and hardness of the magnesium which improves the castability. AM60 is also very strong making it excellent for support functions. Table 2-5 shows the mechanical properties of AM60 alloys.

Table 2-4: Nominal composition (wt%) of the AM60 alloy [20]

Al	Mn	Si	Zn	Fe	Cu	Ni	Others	Mg
5.50-6.50	0.25	0.10	0.22	0.005	0.01	0.002	0.003	BAL.

Table 2-5: Mechanical properties of the AM60 Mg alloy [20]

Tensile strength (MPa)	Yield Strength (MPa)	Elastic Modulus (GPa)	Elongation (%)	Hardness (VHN)
225-240	130	45	8-13	65

Magnesium aluminum alloys are made up of a primary course grain magnesium phase (α-Mg) and an intermetallic β phase ($Mg_{17}Al_{12}$). The intermetallic β-phase particles are distributed through the grain boundaries. The β-phase is formed by the fast cooling conditions seen in the casting process, during which non-equilibrium solidification occurs and the intermetallic β-phase (which has a higher aluminum concentration than the α-Mg) is formed and distributed along the grain boundaries [15]. These different phases are depicted in the optical microscopy image of AM60 as cast magnesium alloy in figure 2-2. The intermetallic β-phase precipitates are very hard and brittle. This leads to a reduction in the ductility of the magnesium alloy, but it also improves the strength. The amount of the β-phase that is present in the Magnesium alloy depends on the cooling rate of casting as well as the amount of aluminum which is present (AM60 contains 5.5-6.5 wt% Al). It can be noted that the higher the content of aluminum in the magnesium alloy, the greater the ultimate tensile strength and the yield strengths. In a comparison of AM60 (with approximately 6 wt% Al) with AZ91 (approximately 9 wt% Al), the AM60 shows a much lower tensile strength but it is more ductile giving it a higher elongation to fracture, alloying the AM60 alloy to absorb more energy prior to fracture than AZ91 can [15]. Table 2-6 shows how the mechanical properties vary with different aluminum content.

Table 2-6: Aluminum content effect on mechanical properties of Magnesium alloys [15]

Alloy	Al Content (Wt%)	Density (g/cm^3)	Ultimate Tensile Strength (MPa)	Tensile Yield Strength (MPa)	Compressive Yield Strength (MPa)	Elongation to Fracture (%)
Pure Mg		1.745	90	21		2-6
AZ91	8.3-9.7	1.81	240	160	165	3
AM60*	5.5-6.5	1.8	225	130	130	8
AM50	4.4-4.5	1.77	210	125	110	10
AS20	1.7-2.5	1.78	190	90	90	12.6

*AM60 is the Mg alloy used in this project.

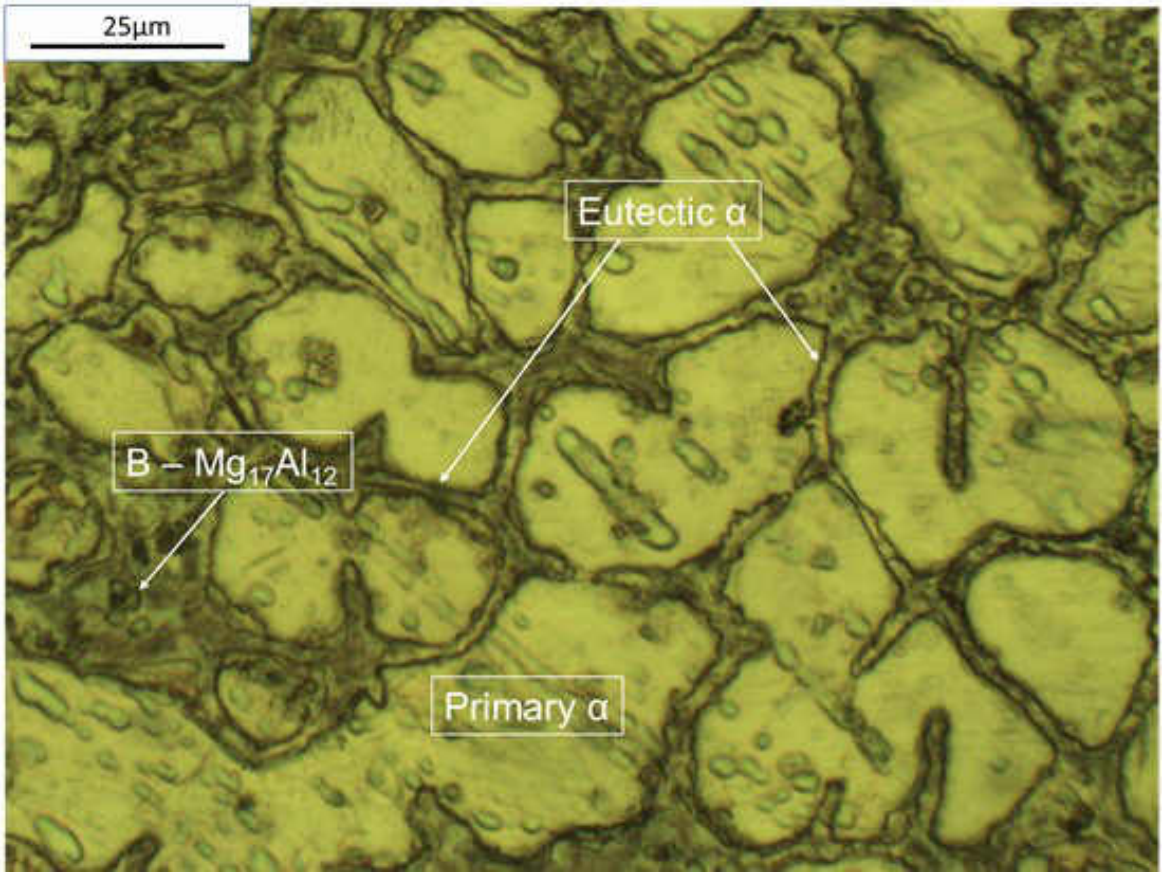

Figure 2-2: The optical microscopy image of the microstructure of as-received AM60 alloy showing the β phase $Mg_{17}Al_{12}$ precipitates along the grain boundaries.

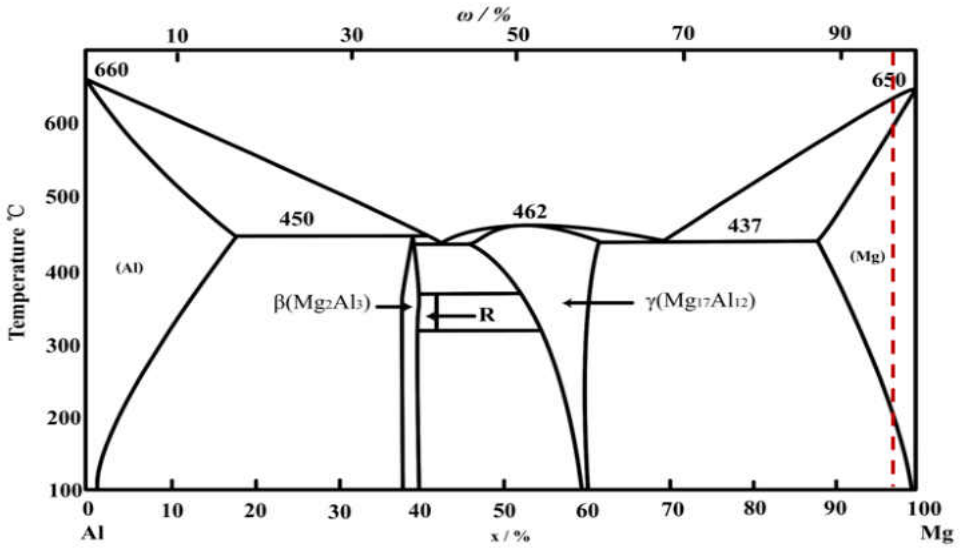

Figure 2-3: Al-Mg binary phase diagram [21]. The dashed line, schematically, shows the position of the AM60 alloy.

2.1.5 Applications

Magnesium is only behind steel and aluminum as the third most common metal used in structural applications. It has many uses in automotive, aerospace, defense, electronics, and power tool industries [17, 22].

Aerospace Industry

Magnesium began as one of the most used materials for aerospace construction. In World War I and World War II magnesium was used extensively for the German and US military aircrafts. The US B-36 has been reported to be composed of have 12,200 lbs. of magnesium sheets, 1200 lbs. of magnesium forgings, and 660 lbs. of magnesium castings [23]. In commercial aircrafts the Boeing 727 build between 1962 and 1984 had 1200 components made of magnesium alloys [17]. However, most of the application for magnesium parts has been removed from aircrafts because of the concerns with the hazard associated with the flammability of magnesium and corrosion problems [24].

Currently the use of magnesium alloys in aerospace industry is limited to engine and transmission related castings and landing gear. Magnesium alloys are not currently used for structural application in major aircraft manufacturers [25] but is being used in the helicopter industry. Below is a list of current aerospace applications [17]:

- Sikorsky UH60 Family (Blackhawk) main transmission, ZE41 alloy;
- Sikorsky S92 main transmission, WE43A alloy;
- Thrust reverser cascade casting in AZ92A alloy found on Boeing 737, 747, 757 and 767;
- Pratt & Whitney F119 auxiliary casing, WE43 alloy;
- Pratt & Whitney Canada PW305 turbofan in ZE41 alloy;
- Rolls Royce tray in ELEKTRON ZRE1 alloy

There are current researchers working with the aerospace industry on developing new magnesium alloys and manufacturing processing for aerospace applications and it is expected that magnesium alloys will begin to increase in use as structural applications for the aerospace industry [17, 26].

Figure 2-4: Applications for magnesium alloys in the aircraft industry [27]

Automotive Applications

In the automotive industry there is a continual and increasing interest in creating light weight vehicles aiming to achieve a large reduction in the fuel consumption of new vehicles [17, 28, 29] and in turn decreasing the carbon footprint. Magnesium was first use in the automotive industry in 1921 with the development of racing engine pistons developed by Dow Chemical [17, 30] in the US and in 1925 magnesium alloys were used for pistons in Germany. In 1931 General Motors used magnesium alloys in their crankcase on the Chevrolair [17, 30]. The use of magnesium alloys in the automotive industry grew throughout the 1930 and World War II and again grew with the introduction of the Volkswagen Beetle. In the 1970's the use of magnesium alloys in the automotive industry for powertrain applications began to decrease as power requirements and operating temperatures grew [17, 26]. Today, the interest of using magnesium in automotive industry is increasing [31, 32] but there is still not a great deal of actual applications as compared to steel, aluminum, and plastics [17]. Currently the average amount of magnesium in a vehicle is less than 1% of the total vehicle weight. Most of the applications for magnesium in the automotive industry are interior as the possibility of galvanic corrosion is much less. These interior applications include instrument panels, steering and seat structures. There are limited applications in the car bodies using cast magnesium alloys and still some application for powertrain parts which are restricted to lower temperature applications [28]. Figure 2-4 shows examples of Mg powertrain components.

Since currently there is a limited amount of automotive parts and components made from magnesium alloys there is a great opportunity to expand the applications for magnesium in light weight vehicle construction [17].

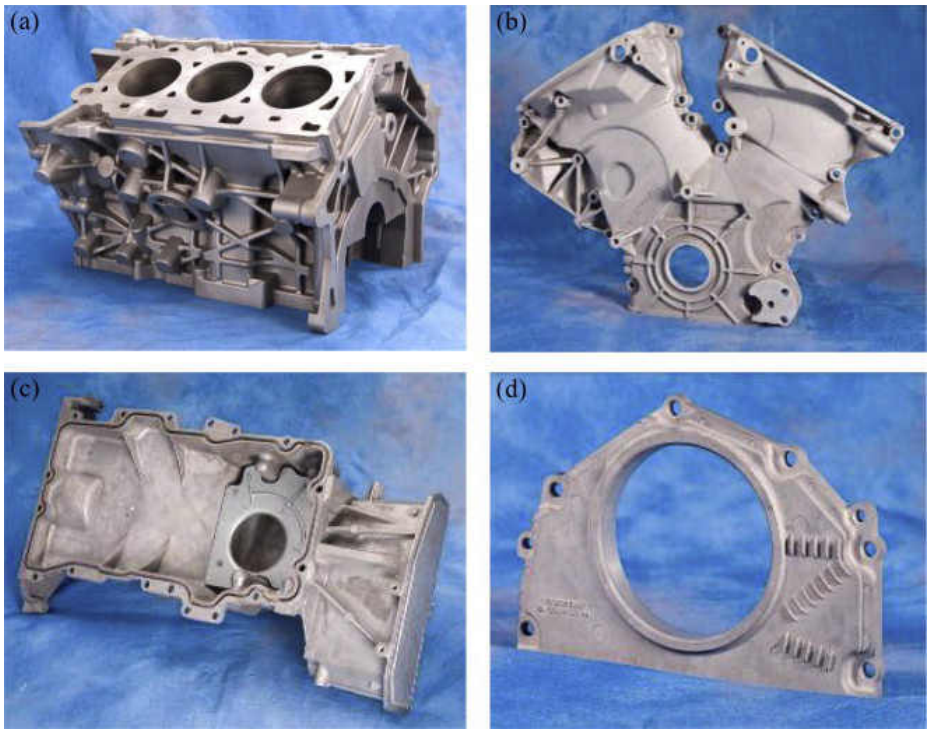

Figure 2-5: Magnesium powertrain components from the USCAR magnesium powertrain cast components project; (a) LPDC cylinder block, (b) Thixomolded front engine cover, (c) HPDC oil pan and (d) HPDC rear seal carrier [17].

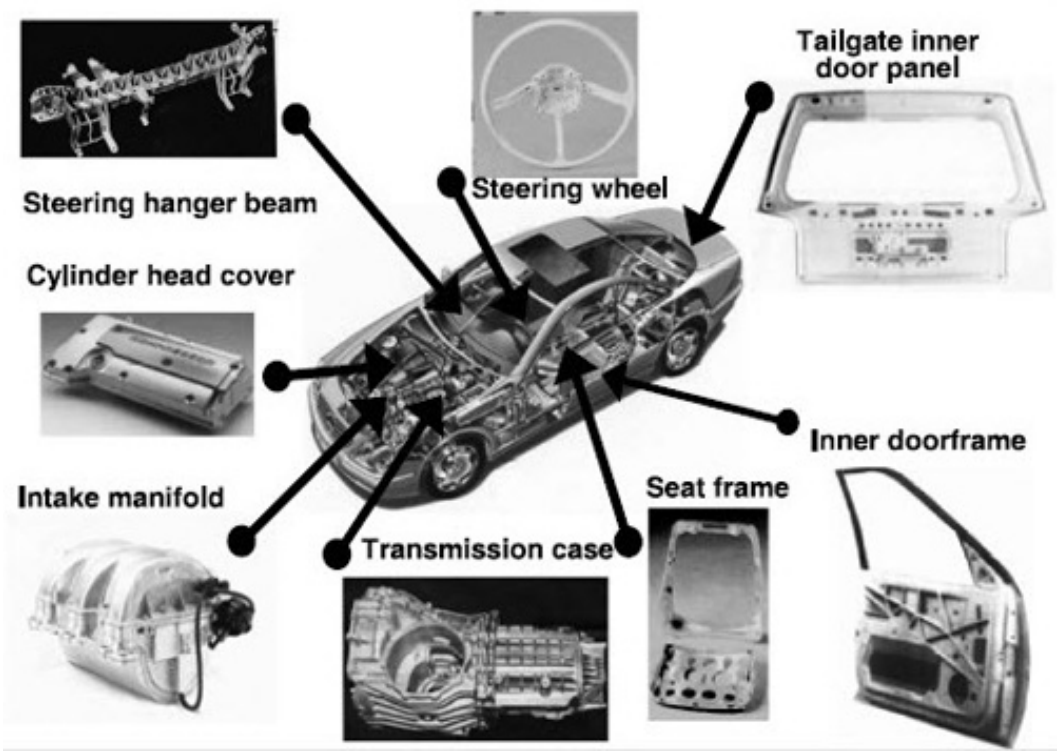

Figure 2-6: Examples of applications for magnesium alloys in the automotive industry [33].

Other Applications

Aside from being lightweight and strong magnesium alloys also have excellent heat dissipation (100 times better than plastics), better vibration dampening than any other metal, excellent machinability, and is environmentally friendly and easy to recycle [17, 34, 35, 36]. This gives it multiple benefits for other industries including electronic and power tools.

The electron industry has a need for light weight, tough, environmentally friendly materials and manufacturers are using magnesium alloys to achieve all these requirements to manufacture everything from digital cameras to notebooks and more [34]. The excellent castablity of magnesium allows for the design challenges of these devices to easily be met creating products for consumers that are lighter, thinner and more mobile. The strength of magnesium allows for the protection of the sensitive electronics inside the devices and gives them the strength and durability to withstand the abuse consumers put on these devises daily [34].

More specifically AM60 Mg alloy is used in the automotive industry in uses for wheels such as with Porsche [37] and preferentially in automotive structural applications [38] including engine components, door and seat frames, and instrument panels [39] because of its greater toughness and ductility than other Mg alloys [38].

Die cast magnesium parts are used in the power tool industry because it provides more durable, light weight designs, making them easier to use for people working with the tools for long periods of time. This greatly helps those in the construction field.

2.2 Aluminum

2.2.1 Physical and mechanical Properties of Aluminum

Aluminum is the most abundant metallic element on the earth's crust and the third most abundant element behind oxygen and silicon. [40, 41, 42]. Aluminum makes up 8% of the earth's crust. Aluminum most often occurs as alum, which is Potassium Aluminum Sulphate [41]. Aluminum has an atomic number of 13 and the atomic weight (average mass of the atom) is 26.98 g/mol. Aluminum is part of the periodic table group 13 and is the second lightest metal (density 2700 kg/m^3) next to Magnesium. Table 2-7 shows the physical properties of pure aluminum.

Table 2-7: Physical properties of pure aluminum [40, 43, 44, 45]

Physical Property	Density (g/cm^3)	Melting Point (^{o}C)	Specific Heat (Cal/g^{o}C)	Thermal Conductivity (W/mK)	Crystal Structure	Youngs Modulus (GPa)
Pure Aluminum	2.70	660	0.22	235	FCC	70

Aluminum is the second most commonly used structural metal only behind iron [46]. Aluminum crystallizes into a face centered cubic (f.c.c.) structure [43] making it a closed packed structure.

2.2.2 Aluminum Alloys

Aluminum is almost always used as an alloy even if it is more than 99% aluminum [41]. The most common aluminum alloys are Zinc, Copper, Silicon, Magnesium and Manganese [41]. Like Magnesium, the purpose of alloying aluminum is to improve its mechanical properties. Aluminum and aluminum alloys have a unique combination of properties which make aluminum a versatile, economical, and attractive metallic material that can be used in a wide range of applications from soft, extremely ductile foil, to highly demanding

engineering applications such as strong, lightweight structures. Aluminum alloys are only second to steel in use as a structural material [47]. Table 2-8 shows the effects of different alloying elements on the mechanical properties of aluminum.

Table 2-8: The effects of alloying elements on Aluminum [48, 49, 50]

Alloying Element	**Effect on the Mechanical Properties**
Zinc (Zn)	• Increases strength
Copper (Cu)	• Increase strength and hardness • Facilitates precipitation hardening • Reduce ductility, and elongation • Reduce corrosion resistance • Increase susceptibility to corrosion cracking
Silicon (Si)	• Reduces melting temperature • Improves fluidity • Increase strength • Reduces specific gravity • Reduces coefficient of thermal expansion
Magnesium (Mg)	• Increase strength without noticeable decreasing ductility • Improves corrosion resistance • Improves weldability and machinability
Manganese (Mn)	• Increase strength • Decreases resistivity • Does not affect corrosion resistance

2.2.3 Cast Aluminum Alloys

Aluminum alloys have two major categories, wrought and cast. Since the aluminum material studied in this thesis is a cast aluminum alloy, this section of the literature review is mainly based on aluminum casting and cast alloys. Cast aluminum alloys are the most adaptable of all cast alloys and commonly have the highest castability rating [47]. Cast aluminum alloys can be produced with a wide variety of characteristic. There are over 100 different alloys registered with the Aluminum Association (AA) and over 300 alloys in international use [50].

Aluminum possesses a low melting point and excellent castability which makes it naturally attractive for casting purposes. This leads to the development of the existing casting processes which allow for complex engineered shaped being produced through melting and casting of aluminum alloys [50].

One of the common casting techniques for aluminum and aluminum alloys is pressure die casting which was developed in the 1820's [50]. It began as a mechanical process where the molten metal was pumped under pressure into the molds using a hand crank. Pneumatic and hydraulic systems were eventually developed and complex parts including bicycle frames were manufactured. Aluminum can be cast using all the existing casting processes including pressure die casting, permanent mold, clay/water bonded sand, chemically bonded sand, plaster mold, and investment casting. There are several variations to these casting processes that are important to the development of cast aluminum parts, these include: molding and pattern distinctions (lost-foam, evaporative pattern), shell and V-mold, and process derivatives (squeeze casting, low-pressure permanent mold, vacuum riser-less casting, and semisolid forming) [50].

There are several advantageous characteristics of cast aluminum [47, 50]:

- Good fluidity (advantageous for filling thin sections)
- Low melting point (relative to other metals), don't require refractory materials to cast
- Short casting cycle because of the rapid heat transfer from molten aluminum to the mold

- Hydrogen is the only gas that is soluble in aluminum and that can be controlled through processing
- Most aluminum alloys are free from hot-short cracking and tearing tendencies
- Chemically stable
- Good as-cast surface finish with few to no blemishes and lustrous surface finish
- Cost effective
- High mechanical properties and resistance to fatigue without heat treatment because of the fine microstructure produced by rapid solidification during casting process
- Ability to produce near-net-shape parts with dimensional accuracy, controlled surface finish, complex geometries including internal passages, and properties consistent with specified engineering requirements

Pressure die casting is used for high volume production casting. In this process the molten aluminum is injected into cavities of steel dies. It is pressurized up to 140 MPa. Most parts manufactured using die casting weigh around 5 kg, however it is possible to produce parts weighing over 50 kg. The size of the part is limited by the machine capacity. It is also possible to create parts with extremely thin cross-sections as compared with other casting methods. There is very little post process machining required after die casting because the as-cast surface is extremely smooth and detailed. Table 2-9 below shows the design parameters and manufacturing characteristics for magnesium die casting.

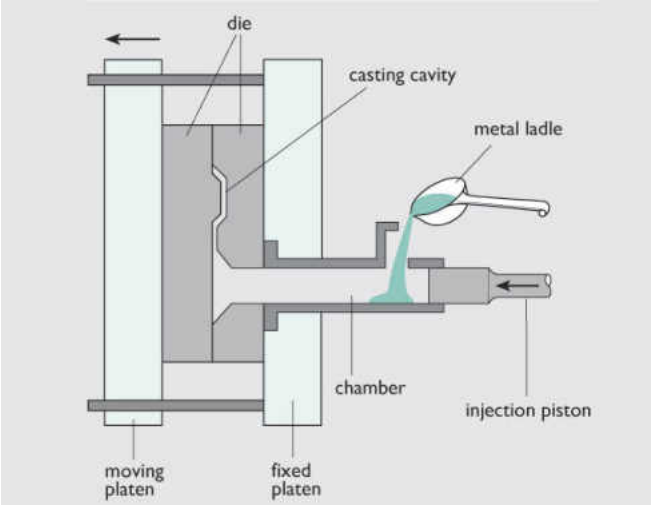

Figure 2-7: Pressure die casting [51]

Table 2-9: Design parameters and manufacturing characteristics for aluminum die casting [17]

Design Parameter	
Dimensional Tolerance (mm/min)	±0.002
Draft angle (°)	2-3
Minimum wall thickness (mm)	2-2.5
Casting/molding cycle time (unit)	1.4-1.6
Typical die life (×1000 shots)	100-150
Trimming cycle time (unit)	1
Machinability	Good
Welding/joining	Good
Surface finishing	Excellent
Recyclability	Good

There are several limitations to casting of aluminum alloys. For instance, there are limitations on the size of the parts for the different casting processes. Solidification of complex shapes can lead to surface discontinuities and internal microstructural features with different levels of quality that can affect the mechanical properties and performance of the part [50]. Internal porosity can form during the solidification of parts with complex geometries and varying thicknesses. The internal porosities can cause stress concentrations

at the voids which in turn can lead to premature failure of the part. This internal porosity in aluminum is caused by the precipitation of hydrogen from a liquid and/or through shrinking of the molten metal during solidification. Although most internal voids are formed from the hydrogen precipitation and/or shrinkage during solidification there are a few other causes of these internal voids: mold reactions, high-temperature oxidation, blowholes, and entrapped gas [50]. As mentioned previously, these voids can facilitate the fatigue crack initiation which in turn can reduce the life of the component and lead to a reduced cyclic strength.

2.2.4 Aluminum-Silicon Alloys

Aluminum-silicon alloys are a group of materials which provide the most substantial portion of all manufactured casting aluminum materials [52]. Aluminum-silicon alloys are used in a large variety of applications in both the automotive and aerospace industries. This is due, in part, to the combination of excellent mechanical properties and castability, along with the alloy's affinity for wear and corrosion resistance [52]. The addition of silicon to the aluminum alloy helps to improve fluidity, increases strength and reduces the melting temperature of the alloy [48, 50].

Silicon is the main alloying element in Aluminum-Silicon alloys. In a hypoeutectic aluminum-silicon alloy the silicon content varies from 5 to 12 wt%. In a eutectic alloy the silicon is typically around 12 weight %, and in a hypereutectic alloy the silicon content is greater than 12 weight %. The addition of silicon in aluminum is what aids the alloy in improving its castability. The silicon helps to improve the fluidity of the metal which increases its ability to ability to easily fill dies and to solidify castings with no hot tearing or hot cracking issues. The greater the amount of silicon an alloy contains the lower the

thermal expansion coefficient is, which helps minimize any shrinkage during solidification. Silicon is also very hard which helps to improve the aluminum-silicon alloys hardness and wear resistance. Silicon can also be combined with other alloying elements to improve the alloy's strength [50, 52]. By increasing the silicon content from 7 wt% to 12 wt%, the yield strength and the ultimate tensile strength (UTS) are increased by 22 and 25 MPa at 250ºC, respectively [50].

The silicon content in the cast aluminum-silicon alloys is what influences the tensile properties of the alloy at both ambient (room) and elevated temperatures. This increase in strength can be contributed to the transfer of the load to the unyielding and extremely interconnected silicon plates from the α-Al matrix [50]. The strength and load carry capacity of the eutectic silicon can be reduced through spheroidization (see Fig. 2-8), this helps to improve the machinability, ductility, and fatigue strength of the alloy [50]. During this process the temperature of the cast AlSi alloy is brought up to just under the eutectic temperature and allowed to cool slowly. This results in a loss of the interconnectivity of the eutectic phases. The rate that the interconnectivity is lost at depends on the temperature and the time it is exposed to these temperatures.

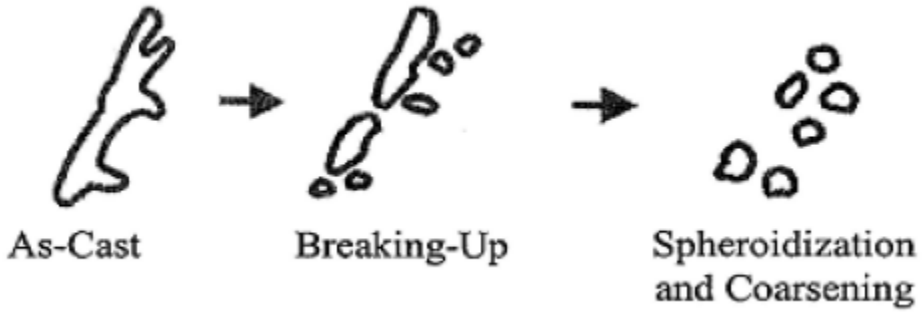

Figure 2-8: Schematic of Si spheroidization in cast Al-Si alloys [53]

This study was done with cast aluminum alloy Al-10%Si which is a hypo-eutectic alloy (see Al-Si phase diagram in Fig. 2-10). The main alloying element is silicon with a secondary alloying element of magnesium. Table 2-10 shows the nominal composition (wt%) of the Al-10%Si alloy. In addition to improving the castablity and hardness with the addition of silicon, the secondary alloy, magnesium, also improves the strength, weldability, castability, and corrosion resistance. Al-10%Si is very strong which makes it an excellent alloy for support functions. Table 2-11 shows the mechanical properties of Al-10%Si.

The addition of magnesium to the Al-Si alloy helps to increase the tensile strength at higher temperatures (up to 200 ^{o}C), increases creep resistance, and decreases the rate of strength loss at higher temperatures. This increase in strength is from precipitation of the secondary phase β-Mg_2Si [52].

Table 2-10: Nominal composition (wt%) of the Al-10%Si alloy [54]

Al	Si	Fe	Cu	Mn	Mg	Ni	Zn	Others
BAL.	9-11	Max 0.55	Max 0.05	Max 0.45	0.2-.045	Max 0.05	Max 0.10	Max 0.25

Table 2-11: Mechanical properties of the Al-10%Si Mg alloy [54]

Tensile strength (MPa)	Yield Strength (MPa)	Elongation (%)	Hardness (HBW)
340 +/- 40	250 +/- 15	1.5 +/- 0.5	120 +/- 5

Aluminum-silicon alloys are comprised of aluminum dendrites, α-Al phase structure, which are precipitated along the Al-Si eutectic phase. This is shown in figure 2-9. In hypereutectic Al-Si alloys (such as those with a Si concentration of less than 12wt%), the α-Al solidifies dendritically. The dendrites will often have four secondary arms which grow around the primary stem at each junction, this is true for all cubic structures [52].

The formation of the Al-Si eutectic mixture continues as the aluminum-silicon alloy further solidifies. Two phases of Al and Si precipitates at the same time from the liquid as eutectic solidification occurs at a constant temperature [52]. Figure 2-10 is a schematic of a phase diagram for Al-Si alloys. The eutectic point of Al-Si is at 12.6 wt% with a temperature of 577 °C. The silicon is soluble in aluminum up to 1.6 wt% while aluminum in silicon is almost zero [52, 55]. Most commercially used aluminum-silicon alloys also contain additional alloying elements such as Copper (Cu) or Magnesium (Mg). These eutectics may be more complex then when simply looking at the aluminum-silicon systems [52].

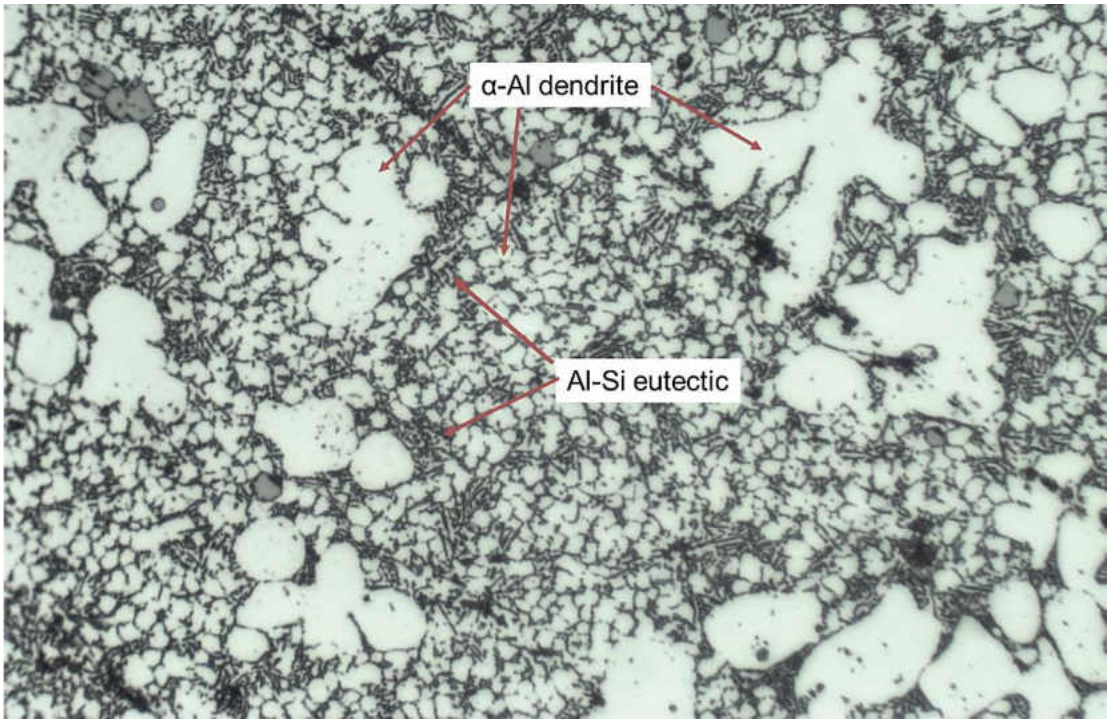

Figure 2-9: Solidification structure of hypoeutectic Al-Si alloy

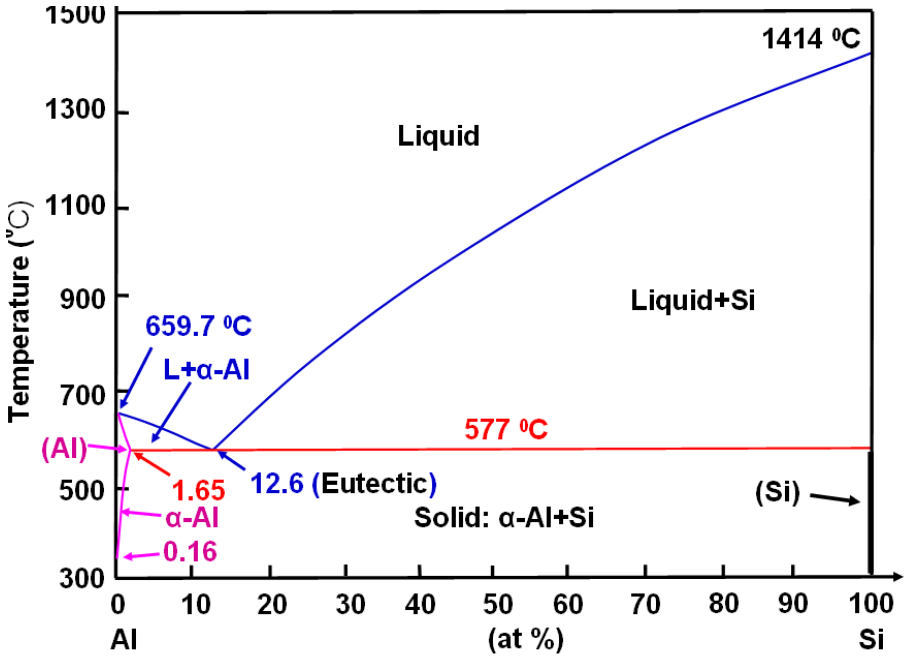

Figure 2-10: Aluminum-silicon phase diagram [56]. Alloys with less than 12% Si are referred to as hypoeutectic, those with close to 12% Si as eutectic, and those with over 12% Si as hypereutectic [57]

2.2.5 Applications

Aluminum alloys are second behind steel as the most common metal used in structural applications. There are many uses for aluminum in aerospace and automotive industries.

Aerospace Industry

For aircrafts to perform they must be reliable, this involves the material they are made from must work consistently. Aircraft performances have advanced so rapidly that the material must meet these structural requirements. Aluminum alloys have met these strength requirements and then some. The main properties of aluminum alloys which make it idea for aircraft construction include [42]:

- light weight as compared to steel components with equal strength
- good corrosion resistance

- easy to fabricate
- aesthetically pleasing

Aluminum alloys have been used for structural components in aircrafts since the 1930's as the material of choice. Though polymer matrix components are being used in some aircraft components, aluminum alloys are the main choice for the fuselage, wings, and support structures in commercial aircrafts, military cargo and transportation. The main reasons for the use of aluminum alloys in aircrafts is because of the known costs associated with their fabrication (low costs), the historical design experience and manufacturing methods, as well as the excellent mechanical characteristics. All these qualities guarantee the continual use of aluminum alloys in substantial qualities well into the future. On top of these, there are continuing to be major advances in aluminum aircrafts that keep the aluminum alloys competitive with other materials [58].

Automotive Industry

The increasing concern for air pollution put a large demand on the automotive industry to reduce the weight of their vehicles. Aluminum alloys' properties (high stiffness to weight ratio, formability, corrosion resistance, and recycling potential) make it an excellent candidate to replace the heavier materials used in the automotive industry to aid in the reduction of energy consumption and air pollution. Steel has been dominant in the automotive industry since the 1920's [59] but the concerns about global warming has triggered the industry to reevaluate the materials being used to improve their fuel economy. A decrease of 10% in the weight is equivalent to approximately 5.5% reduction in fuel economy [59].

Recent applications of aluminum alloys, and Al-Si cast alloys, in the automotive industry include vehicle power trains, chassis, body structures, and air conditioning [60]. Engine blocks are being switched from cast iron to aluminum [59, 61]. Engine blocks are subject to high mechanical and thermal cyclic stresses. It is imperative that these parts have high fatigue strength and wear resistance. The cycle stresses can cause microcracks to initiate at stress concentration points and will cause premature failure [61]. In powertrains, aluminum alloy castings are being used for 100% of the pistons, 75% of cylinder heads, and 85% of intake manifolds and transmissions [59]. Cast aluminum alloys are being used for wheels, where the loading conditions are higher requiring better mechanical properties. There have also been extensive studies to use aluminum alloys for the vehicle bodies. The use of aluminum also allows for high recycling rates in cars with little energy consumption (only 5% of the original energy consumption is required) [60]. Figure 2-11 shows a number of products produced from aluminum for the automotive industry.

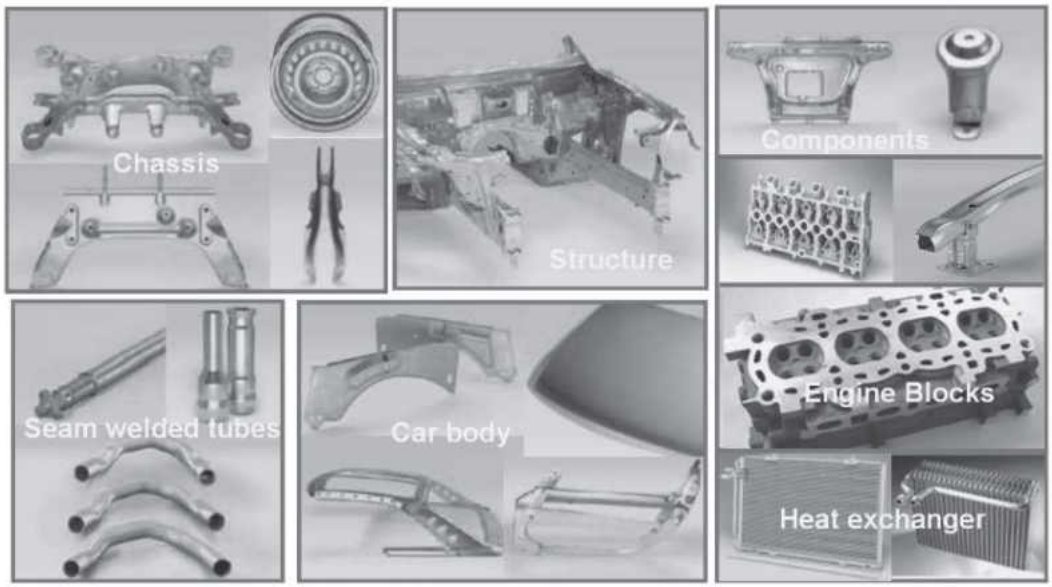

Figure 2-11: Aluminum products for automotive applications [60]

These aluminum applications are mostly being used for high class vehicles. They are currently being used in, Austin Martin Vanquish, BMW Z8 Roadster, Audi A8, and the Jaguar XJ [60] to name a few. Aluminum is being used to produce state of the art Body in White (BIW), shown in figure 2-12. BIW is the heaviest part of conventional steel cars with up to 30% of the weight and has the largest weight saving potential by using aluminum in place of steel [60]. Aluminum is being used in applications such as vehicle structures, doors, closures, and outer panels [60]. Cast aluminum components are being implemented in engine blocks, cylinder heads, wheels and special chassis parts. They are also being used in frames, axial parts and structural components. High integrity casting allows for complex parts and ensured optimal mechanical properties and enhances functional integration [60]. Figure 2-13 is an image of an Audi Al2 body structure made of all aluminum alloys.

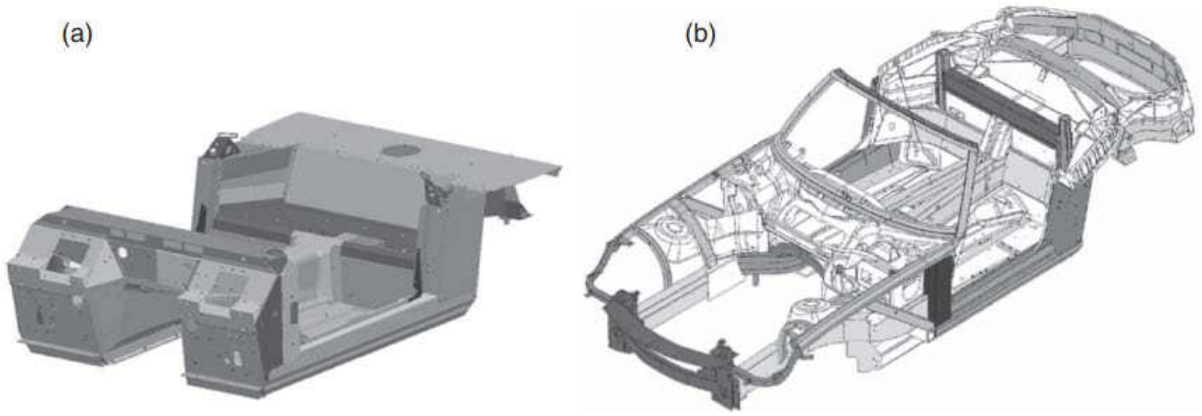

Figure 2-12: State of the art BIW design [60]

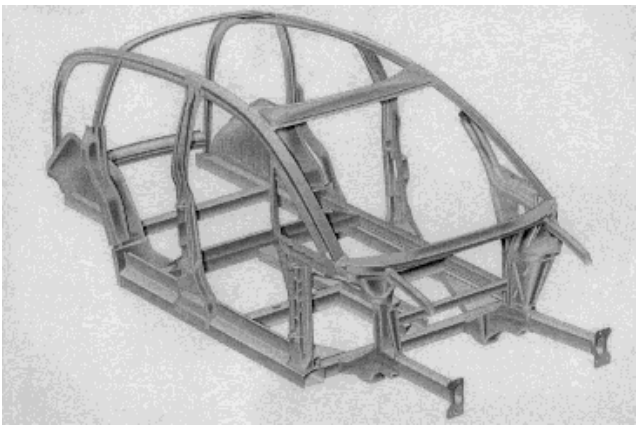

Figure 2-13: Audi AL2 with an all-aluminum body structure [59]

Military

Because of the high ballistic performance and static strength of high strength aluminum alloys, they are being used for armor purposes. The UK has been using aluminum alloys on their armor since the 1970's. The US is using aluminum alloys as the main structural alloy for their Advanced Amphibious Assault Vehicles (AAAVs). AAAVs are armored personal carriers that are currently under development of the US Marine Corps. The aluminum alloys structure carries more than 18 fully outfitted marines at highspeed across land and sea [21, 62].

2.3 Microstructural Influences on Mechanical Properties

The mechanical properties of magnesium and aluminum alloys are affected by their microstructure. There are three main microstructural features which greatly impact the mechanical properties of these alloys; these features include the grain size, dendrite arm spacing, and porosity (size and distribution).

2.3.1 Microstructure of Mg Alloy AM60 and Al Alloy Al-10%Si

AM60 Mg alloy is a cast magnesium alloy with aluminum (Al) as the main alloying element (6 wt% Al). Aluminum improves the tensile strength, hardness, and enhances the castability of the alloy. The microstructure of AM60 Mg alloy consists of course grains of alpha magnesium (α-Mg), and an intermetallic beta phase (β-phase) distributed through the grain boundaries (see Fig 2-12). The β-phase consists of $Mg_{17}Al_{12}$ and is formed due to the fast cooling conditions, which are typical of the casting process. Non-equilibrium solidification occurs and the intermetallic β-phase, which possesses a higher Al concentration than the α-Mg phase, forms and is distributed along the grain boundaries. The hard and brittle nature of the β-phase leads to decreased ductility but improved strength of the cast Mg alloy [63]. The magnesium AM60 cast alloy, with greater toughness and ductility than AZ91 and slightly lower strength, is largely used in several components, such as brackets, seat frames, instrument panels, and steering wheels for the automotive structural applications [64, 65, 66]. Moreover, AM series show excellent damping properties for external impact and vibration applications [4, 63, 67, 68].

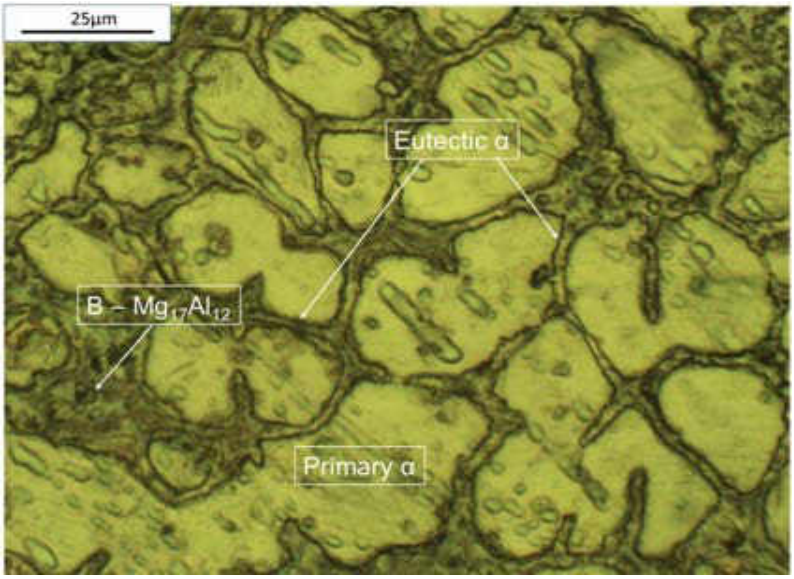

Figure 2-14: Microstructure of the AM60 Mg alloy

Cast aluminum-silicon alloy Al-10%Si is a hypoeutectic Al-Si alloy. The microstructure is made up of a primary phase (α-Al) dendrites and eutectic mixture of Al-Si [69]. The percentage of Si in the alloy dictates the microstructural eutectic mixture. The eutectic mixture comprises a soft Al matrix containing Si particles. The shape of the Si particles are plate-like and they can be changed with different treatments. Secondary alloying elements such as Cu, Mg and Fe in the Al-Si alloys form different intermetallic compounds in the alloy's microstructure. The most common intermetallic compounds in the Al-Si alloys are Al_2Cu, Mg_2Si, α-$Al_{12}(Fe,Mn)_3Si_2$ and β-Al_5FeSi [52]. Aluminum-silicon alloys can be divided into three separate categories based on their Si weight percentages. These categories are hypoeutectic (< 12.6 wt % Si), eutectic (= 12.6 wt % Si), and hypereutectic (> 12.6 wt % Si) (figure 2-X) [57].

The microstructure of eutectic as-cast Al-12%Si is show in figure 2-14. The eutectic alloy contains eutectic Si particles which have a fibrous morphology in the shape of needle like plates, an α-Al phase, and some coarse primary Si particles which are formed because of non-equilibrium cooling and a slight variation in the eutectic composition. The eutectic Si particles are spread through the α-Al matrix. This microstructure is characteristic of as-cast eutectic Al-Si alloy [70].

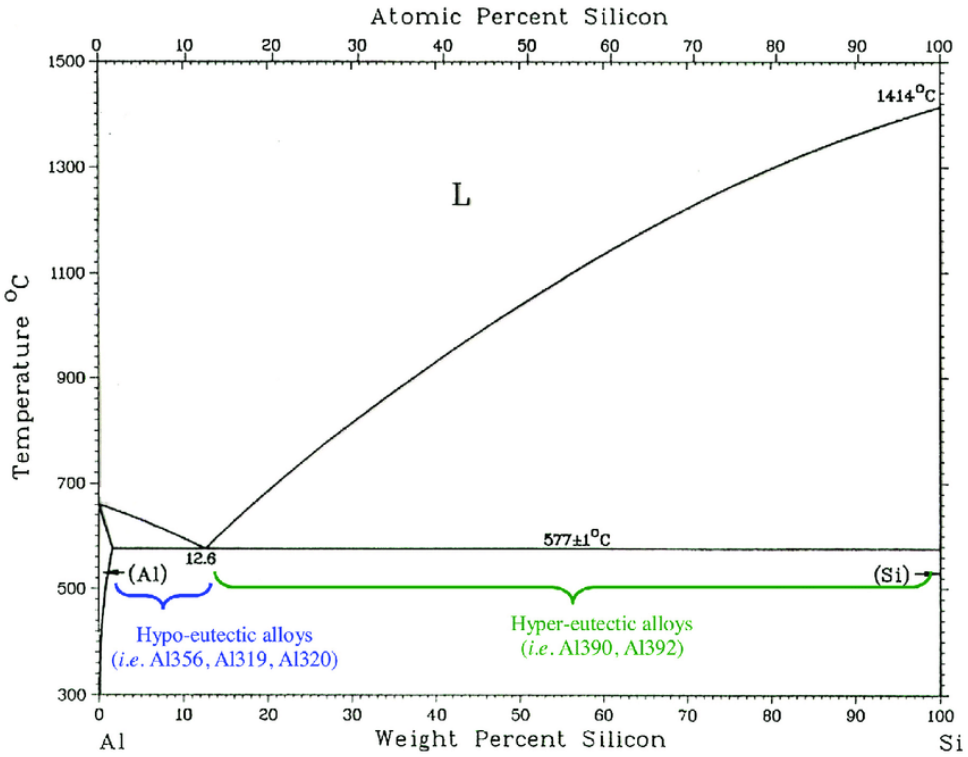

Figure 2-15: Al-Si phase diagram showing the hypoeutectic and hypereutectic Si-Al alloys [56]

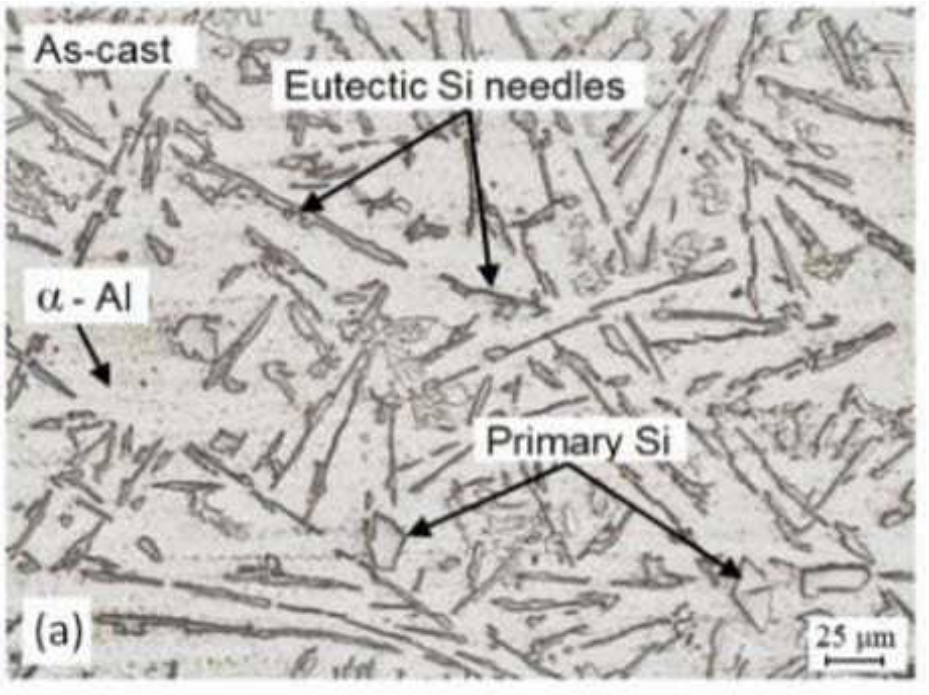

Figure 2-16: Eutectic as cast Al-Si alloy [70].

2.3.2 Effects of Grain Size

The mechanical properties (i.e. yield stress, and hardness) of alloys are largely dependent on the average grain size, d. The relationship between the grain size and the yield strength is known as the Hall-Petch equation. This equation is:

$$\sigma = \sigma^0 + k(d)^{-1/2} \qquad \text{Eq. 2-1}$$

This equation specifies that the strength of the material is equal to the intercept/frictional stress (σ^0) plus a factor (k, slope) time the inverse of the square root of the grain size (d). The intercept stress (σ^0) and the Hall-Patch slope (k) are known as the Hall-Patch parameters. This equation indicated that by decreasing the grain since the strength of the material will increase and by increasing the grain size the strength of the material will decrease [15].

Figure 2-15 shows the variation of yield strength with respect to the inverse square of grain size for austenite grain steel.

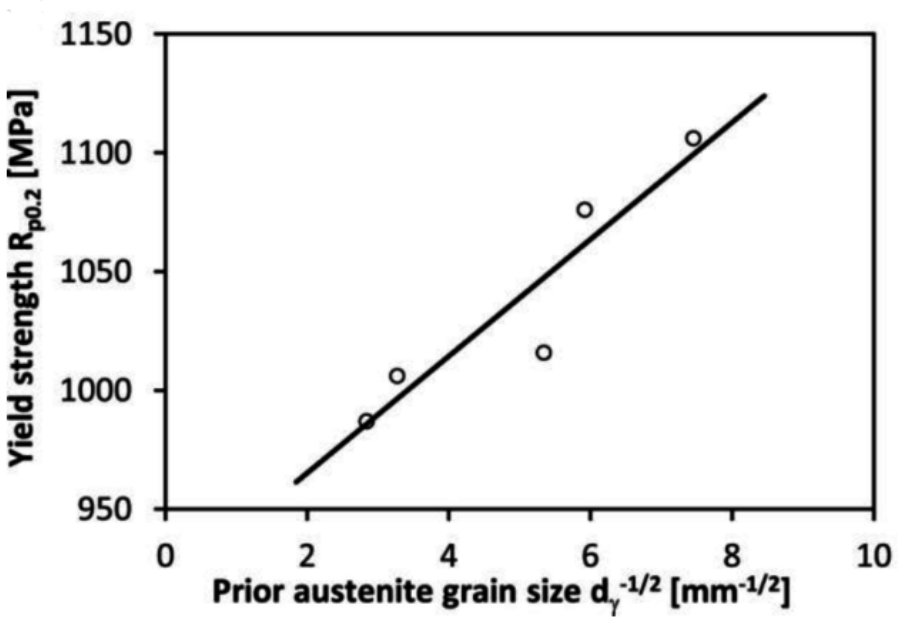

Figure 2-17: The influence of grain size on yield stress [71]

One common explanation to the Hall-Petch relationship is the dislocation pile-up model. This can be attributed to the dislocation pile-up against the grain boundaries. The more grains (smaller grain sizes) there are more grain boundaries which resist the dislocation motion leading to a higher yield stress. Both Al-Si and Mg-Al alloys have a limited number of active slip systems, which causes the average grain size to greatly affect the elongation to fracture [15].

2.3.3 Effects of Dendrite Arm Spacing

The dendrite arm spacing (DAS) influences the mechanical properties of metals and alloys as grain size does. There have been a few research papers on the relationship between the dendrite arm spacing and how it effects the alloys, mostly aluminum alloys, mechanical properties [72, 73, 74]. Ceschini *et al*. [74] investigated the mechanical properties at various dendrite arm spacing at ambient and elevated temperatures of cast Al-8%Si. In their examination, it was observed that the coarser dendrite arm spacing resulted in reduction in mechanical properties while the finer dendrite arm spacing led to improve mechanical propertied such as tensile strength.

Lee and Shin [73] studied the effects of the dendrite arm spacing (DAS) on the tensile properties and fracture behavior of as-cast AZ91 Mg-Al alloy. They found that the dendrite arm spacing, and the grain size possessed a Hall-Patch relationship with the yield strength but a parabolic relationship with the elongation (Fig 2-16). Below are the relationships found between the grain size and DAS with the yield strength [73].

$$\sigma_{\text{grain size}} = 74.9 + 317.7\times [\text{Grain Size}]^{-1/2} \quad \text{Eq. 2-2}$$

$$\sigma_{\text{DAS}} = 62.6 + 305.5\times [\text{DAS}]^{-1} \quad \text{Eq. 2.3}$$

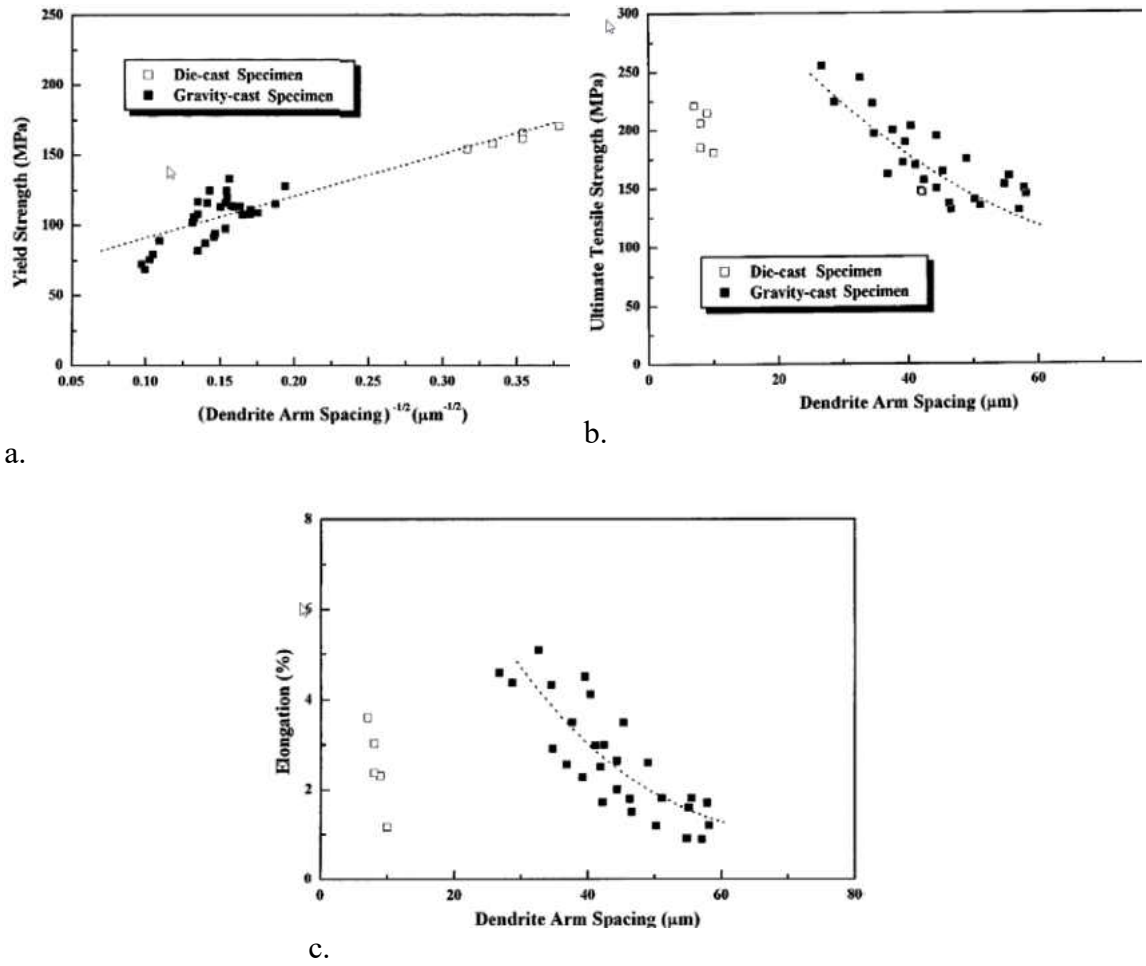

Figure 2-18: Dendrite arm spacing as it related to the a) Yield strength, b) ultimate tensile strength, and c) elongation [66]

2.3.4 Effects of Porosity

Defects in different alloys, such as porosity and voids, possess a substantial effect on the mechanical properties (tensile strength, fracture behavior, etc.) of the material. The pores and voids result in a much higher concentration of stress around them then throughout the rest of the material. This concentration of stress acts as a crack initiation point and leads to premature failure. The size and distribution of the defects determines in the fracture toughness of the alloy [75]. Both cast magnesium alloys and cast aluminum alloy have these porosity defects.

There have been several studies performed to understand the effects of porosity on the tensile and fatigue strength, and ductility of these alloys. Francis and Cantin [76] studied the effect of structural defects on the tensile failure and elongation to fracture of cast Al-7Si-Mg alloys. Surappa *et al*. [77] studied the effects of macro-porosity on the strength and ductility of cast Al-7%Si-0.3%Mg alloy. They reported that the strength and ductility of the alloy depend on the size of the macro-pores as opposed to the volume fraction of the porosity. Biswas *et al*. [78] studied the relationship between the porosity and β-precipitates ($Mg_{17}Al_{12}$) and the mechanical properties of HPDC AZ91 Mg alloy. They were able to correlate the elongation to fracture and the fracture stress to the porosity volume fracture. Hu *et al*. explained that the mechanical properties of magnesium alloy AM50 were dependent on the porosity with in the material, and the thicker materials had more porosity and hence lower strengths than the thinner alloys with fewer pores [79]. Lee [26] investigated the effects that the micropososity and grain size affected the tensile properties of HPDC magnesium alloy AM60. He concluded that the changes in microporosity content significantly change the ultimate tensile strength (UTS) and the elongation. Figure 2-17 shows the relationship between the microporosity and the UTS and elongation for different grain sizes.

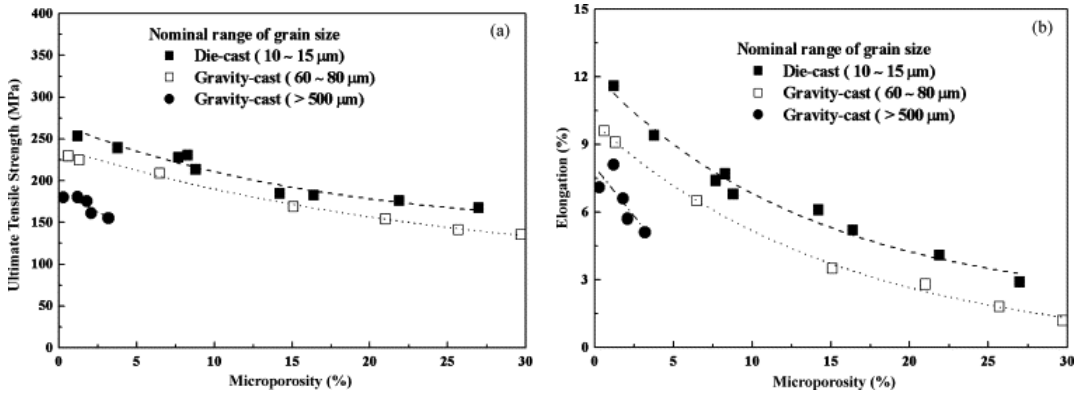

Figure 2-19: Dependence of UTS (a) and elongation (b) on the variation of microporosity for each nominal grain size [26]

2.3.5 FSW Microstructure

The high temperature and powerful plastic deformation contribute to the recrystallization and development of the grains in the stirred zone as well as changes in the microstructure around the stirred zone of FSW joints [21]. The microstructure of FSW joints can be broken down into distinct zones. These microstructural zones of FSWing are: the stirred zone (SZ), thermomechanically affected zone (TMAZ), and the heat-affected zone (HAZ). These distinct zones are schematically shown in figure 2-20 [80]. The different microstructural changes within the weld have a substantial effect on the mechanical properties of the post welded material [21]. The SZ is subjected to frictional heating and plastic deformation. This leads to recrystallized equiaxed, fine grains with in this zone. The border between the SZ and the TMAZ is relatively diffused on the retreating side of the weld but much sharper and more defined on the advancing side. There are many factors that affect the shape (figure 2-21) and grain formation in the SZ including, processing parameters, tool geometry, material (thermal conductivity) [21].

TMAZ is a unique transition zone between the SZ and the HAZ. The TMAZ is subjected to high temperatures and plastic deformation during FSW [21]. However, the TMAZ does not undergo recrystallization because of a lack of deformation strain. The TMAZ is characterized by highly deformed grain structure where the grains are stretched in an upward flowing pattern around the SZ [21]. A typical grain structure of the TMAZ is shown in figure 2-22. Just past the TMAZ is the HAZ. The HAZ does not experience plastic deformation but does go through a heat cycle. This causes the HAZ to keep the same grain structure as the parent metal but there is an effect on the precipitate structure which can cause weakening in this zone [21].

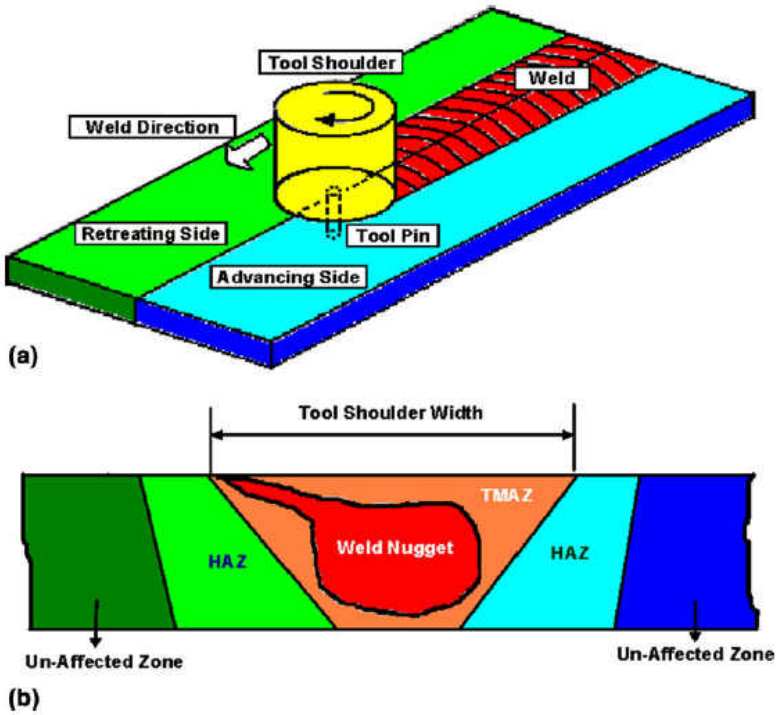

Figure 2-20: (a) A schematic of the friction stir welding (FSW) process, and (b) the main microstructural zones associated with the typical FSW joint [80]

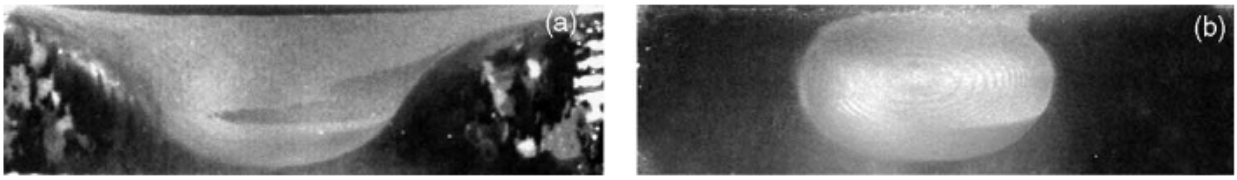

Figure 2-21: Effects of processing parameters on SZ shape a) basin-shaped SZ, b) elliptical SZ [21]

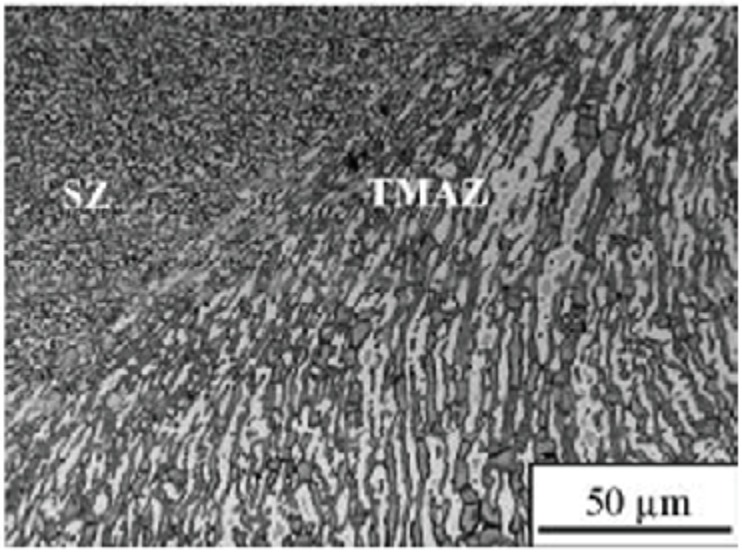

Figure 2-22: TMAZ microstructure of stainless steel [81]

2.4 Friction Stir Welding

2.4.1 Introduction to Friction Stir Welding

Friction Stir Welding (FSW) is considered a solid state joining process because the heat generated by the process does not reach the melting temperature of the materials being joined. FSW has been around for more than 25 years, it was developed in 1991 at The Welding Institute (TWI) in the UK [21]. FSW allows for the joining of materials that, by traditional welding technologies, are considered to be non-weldable, these are materials that traditional welding would have poor solidification microstructure, porosity in the fusion zone, and a significant loss of mechanical properties as compared to the base materials (*i.e.* dissimilar material, Mg alloys, some aluminum alloys, copper, titanium etc.) [82]. In the FSW process (see Fig. 2-23), a non-consumable cylindrical tool with a shoulder and pin is used as a stirrer. The tool is fixed to a milling machine chuck and is rotated along the longitudinal axis (figure 2-24 shows the modified milling machine used in this study). The work pieces to be welded can be butted up or overlapped to one another and are then clamped to stay stationary and withstand the large applied forces (Fig. 2-25 shows the clamping system used in this study). The clamping prevents the workpiece from spreading. The rotating tool pin is then inserted into the work piece at the joint, and the shoulder is forced into contact with the work piece surface. The contact between the workpiece surface and the tool shoulder causes friction heating of the material being joined. The tool is then moved transversely along the joint. As the tool rotates and moves along the joint, the combination of the friction heating and the pin stirring causes the material is softened and stirred together forming a weld. This is done all while keeping the temperature below the melting point of the base materials [21] [83]. Once the tool reaches the end of the joint the

tool is retracted out of the work piece. Four steps of the FSW have been shown in Fig. 2-26.

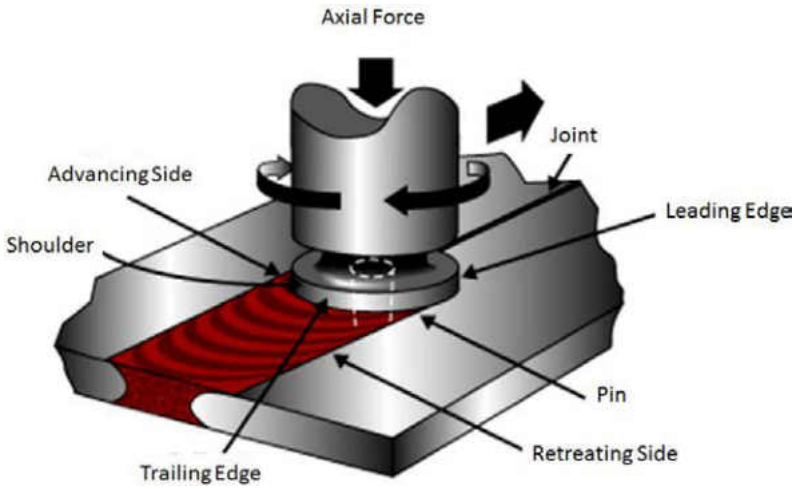

Figure 2-23: Schematic of the FSW [84]


Figure 2-24: Modified milling machine

Figure 2-25: Clamping system

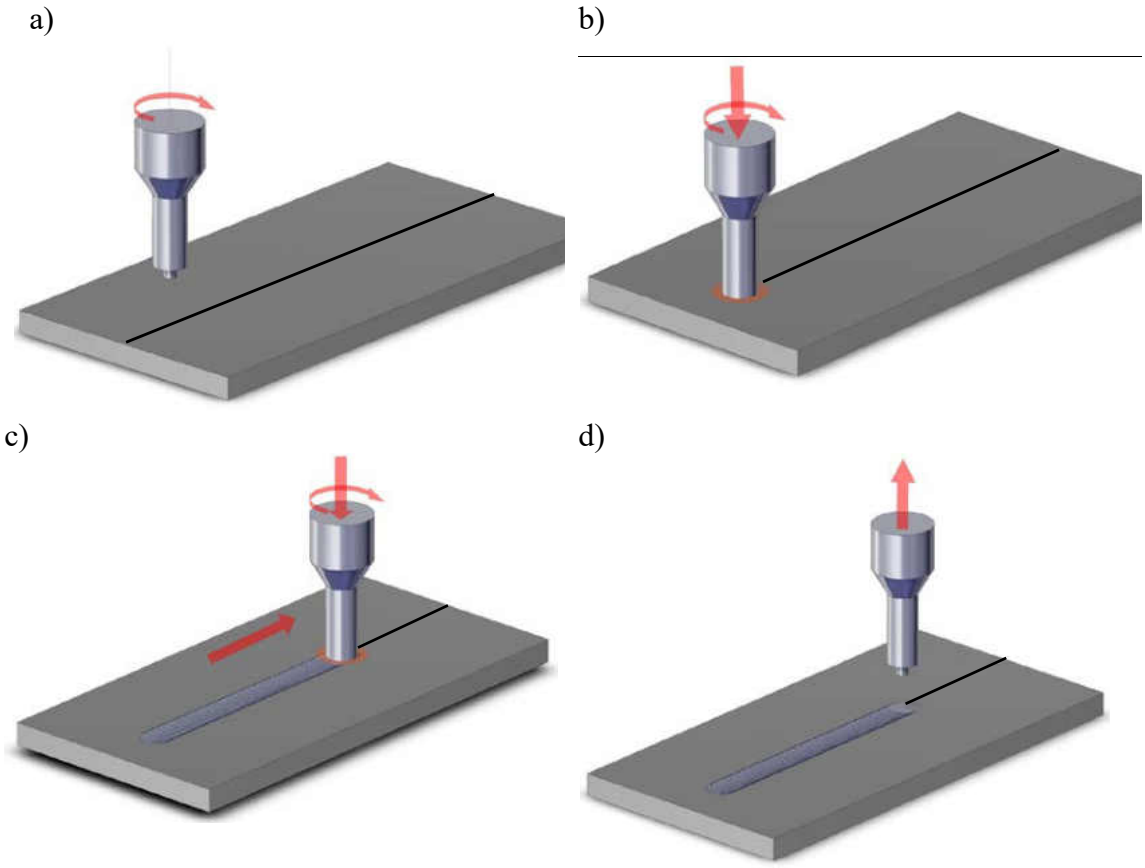

Figure 2-26: Four steps of the FSW including a) initial set up, b) tool plunging, c) traverse, d) tool withdrawal.

Generated heat and mechanical work results different welding zone in FSW (see Fig. 2-27). These zones are as follows [21]:

- Parent metal (PM): where material not deformed, also may be subjected to thermal cycles but there is no microstructural or mechanical change.
- Heat affected zone (HAZ): in this zone the metal goes through a thermal cycle which changes the microstructure and mechanical properties but it does not go through any plastic deformation or dynamic recrystallization and keeps the same grain structure as the parent metal.
- Thermo-mechanical affected zone (TMAZ): this zone is subjected to a thermal cycle and plastic deformation, this causes the microstructure to be highly deformed. The grains from the parent metal are deformed and stretched in an upward flowing design around the stirred zone. Because there is not enough plastic strain there is no dynamic recrystallization, only plastic deformation.
- Stir zone (SZ): dynamic recrystallization has completely occurred. Fine grain size is seen because of severe deformation at high temperature. These fine grain sizes lead to increased strength and hardness of the welded metal.

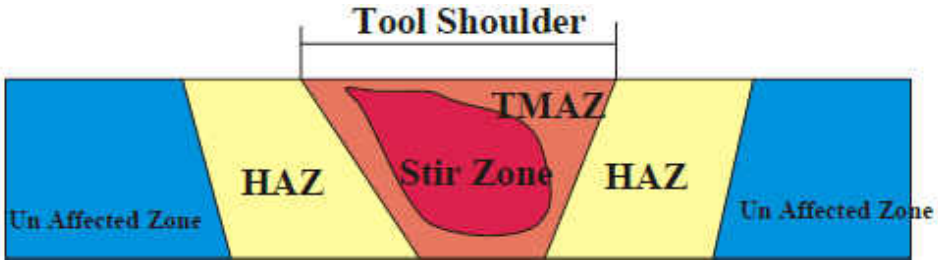

Figure 2-27: Various zones generated in the FSW process [85]

The material flow and movement in the FSW can be quite complex (see Fig. 2-28). The material around the tool is heated, this is accomplished by two methods, friction heating between the tool and the workpiece (mostly the shoulder), and the plastic deformation of

movement of the workpiece material (a.k.a. stirring). The localized heating softens the material around the tool. The rotation of the tool and the translation along the length of the joint causes the movement of the material from the front to the back of the pin [21]. There have been several studies done on the flow of the material using markers and etching, the tool design has a large influence on the material flow [21].

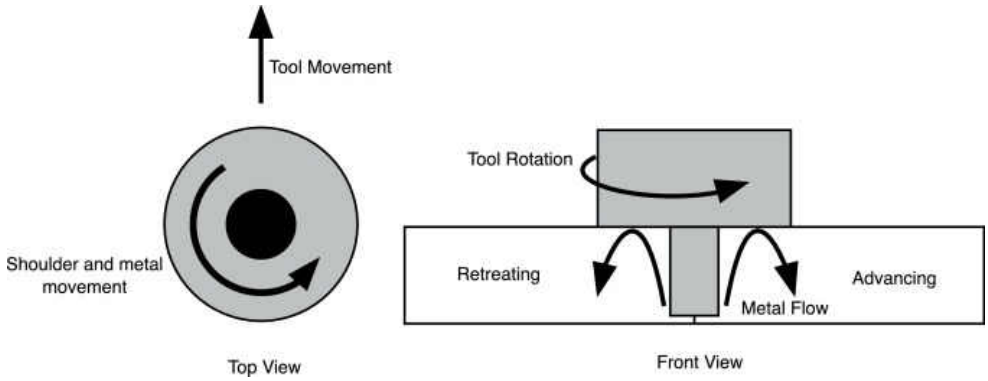

Figure 2-28: Material Flow during FSW [86]

FSW is a multifaceted physical process that involves many inter-related variables which can directly or indirectly affect the weld quality and the performance (see table 2-12). These variables, in the FSW process, are classified as tool related, joint design related, and machine (welding) related parameters as well as a few others, which do not fall into any of these categories. Tool related parameters include the tool geometry and material type of the tool. Joint design includes the joint type which can be a butt, lap, or fillet joint. Machine parameters include tool rotation speed (ω, rpm), transverse speed (V, mm/min), axial force (insertion depth), tool tilt (angle of the spindle), and the offset from the center of the joint. Other factors that could influence the weld quality include the initial temperature of the material (pre-heat or cooling), as well as the cooling rate.

As mentioned previously the FSW tool serves two purposes, to heat the work piece and to move the material. The geometry of the tool influences the heat generation, the plastic flow, and the uniformity of the weld joint. The shoulder generates the heat through friction and

prevents the plasticized material from escaping the work piece. It is important for the tool to be wear resistant, have high fracture toughness, and machinable. The important factor of the shoulder design on the surface and whether it is flat, concave or convex and the diameter of the shoulder. A concave surface creates medium amounts of flash and some defects where a convex surface creates a minimum amount of flash and no defects. The critical role the pin plays in FSW is in the material flow and in turn the welding speeds. The probe length, probe shape (tapered, cylindrical, square, triangular, tri sided, threaded) [21].

Table 2-12: FSW Process Parameters [21]

Rotational speed (RPM)
Welding (traverse) speed (mm/min)
Pin length (mm)
Tool shoulder diameter (mm)
Axial force (kN)
Tilt Angle
Pin diameter (mm)
Shoulder diameter (mm)
D/d Ratio of Tool
Tool materials
Tool profile

A summary of the advantages of FSW is outlined below [87, 21]:

- FSW joint stronger than base metal
- Green technology
- Low heat
    - Energy efficient
    - No distortion
- No shielding gas required

- No wasted materials
- Reduces weight of part leading to reduction of vehicle (decrease in fuel consumption)
- No cracking of joints
- No surface preparation required before FSW
- Good dimensional stability and repeatability
- Eliminate post processing grinding and waste created
- Replace multiple parts joined with fasteners

With advantages there come limitations [21]:

- Formation of exit hole caused by the pin being retracted at the end of the weld
- Large forces required to make the FSW, need strong clamping system (fig. 2-25)
- Can be slower than traditional welding
- Limited flexibility on the joint type that can be welded
- Harder materials cause excessive tool wear on the FSW tool, can be expensive to replace

There are several applications where FSW is current being applied. Below is a list of some of the industries and applications, this list is representative (not exhaustive), and new applications are constantly appearing [88, 69, 22, 26, 89, 62, 21, 90, 91].

- Aerospace (Fig. 2-29)
    - wings, fuselages, floor panels, aircraft landing gear doors, fuel tanks
    - SpaceX Falcon 1 and Falcon 9 rockets
    - NASA Space Shuttle external tanks
- Automotive (Fig. 2-30)

- trailer beds, door panels (Fig 30), center console (smooth design)

- Military
  - joining Armor Aluminum Alloys, such as those in AAAVs (advanced amphibious armored vehicles)
- Railway
  - Roof and side panels, bodies
- Shipbuilding (Fig 2-31) and Offshore
  - panels for decks, sides, bulkheads, floors, hulls, superstructures, heli pads, offshore accommodations, masts, booms
- Computers
  - iMac in 2012 joining the front and back panels
- Construction
  - Aluminum bridges, window frames, Al pipeline and heat exchangers, Oil and Gas pipeline

Figure 2-29: FSW used in aerospace industry [91]

Figure 2-30: FSW used in automotive industry [91]

Figure 2-31: FSW used in shipbuilding [91]

2.4.2 Friction Stir Welding of Cast Magnesium Alloys and AM60

Cavaliere and Marco [92] studied microstructure and high-temperature mechanical (175–300°C) properties of friction stir processed high pressure die cast AM60B magnesium alloy sheets (thickness of 2.5 mm). They used a steel tool with threaded pin (shoulder diameter of 20 mm) with a rotational speed of 700 RPM and a travelling speed of 2.5 mm/s. They recorded exceptional ductility in the friction stir processed samples and attributed this to the fine grain structure of the stir zone that is created due to the recrystallization phenomenon induced by that severe plastic deformation during the FSW process. In a separate study, Li *et al* [35] studied the FSW of magnesium AM60 sheets (thickness of 6 mm) by employing tool rotational speed of 375 and 450 rpm and tool traverse speed of 152.4 mm/min. They reported enhanced ductility in the stir welded samples compared with

the non-processed materials and attributed this to the grain refinement of the processed materials. Esparza *et al* [22] assessed the microstructure-property correlations in the FSWed Thixomolded AM60 Mg alloy. They observed a homogeneous, recrystallized (refined), and equiaxed grains in the microstructure of the welded zone with average grain size of 10–15 μm as compared with ~45 μm average size of the as-received material. Iwaszko *et al* [93] performed friction stir processing on AM60 Mg alloy using three different tool rotational speeds, 3500, 4000, and 4500 rpm, with a constant feed rate of 16 mm/s to refine and homogenize the microstructure of the cast Mg alloy. They reported increase in microhardness and wear resistance of the processed AM60 material compared with the non-processed alloy and attributed the changes to the microstructural evolutions.

2.4.3 Friction Stir Welding of Aluminum-Silicon Alloys and Al-10%Si

Aktarer *et al* [70] studied the microstructural, mechanical, and tribological properties of friction stir processed eutectic as-cast Al-12Si alloy. They used a threaded steel tool (shoulder diameter 16 mm) and a constant rotating speed of 1250 rpm with a travel speed of 65 mm/min. They found that the ductility and strength of the alloy was significantly improved with the FSP, this was attributed to the microstructural changes of the Si particles. In a separate study, Jana *et al* [94] looked at the effects friction stir processing has on the fatigue life of cast Al-7Si alloy. They found that FSP enhanced the mechanical properties of the alloy, improving the fatigue life of the hypoeutectic alloy by five times that of the base material. They found this improvement was due to the elimination of the porosity (cause by casting) which in turn eliminated the notch effect. Sharma *et al* [95] evaluated the mechanical and microstructural characteristics of friction stir welded Al-Si-My alloys. They used a tapered steel tool with a pin diameter 15.6 mm and welding speed

ranging from 19 mm/min to 190 mm/min and a tool rotational speed of 635 rpm. This study determined that the welding speed has a large effect on the microstructure and tensile properties of the FSW joints and that by selecting the parameters carefully any voids can be eliminated, and mechanical properties improved. Weglowski [69] performed friction stir processing on hypoeutectic cast Al-9Si alloys. He studied the microstructure and hardness of the friction stir processed material. Weglowski concluded that the microstructure of the FSP A1-9Si was significantly refined through fragmentation of the non-deforming, initially large Si particles, the Si, Fe, and Mg particles were more evenly distributed through the stir zone than the parent material and the porosity in the cast material was eliminated in the stirred area. He also determined that the hardness was lower in the stirred zone than in the base material and higher in the thermomechanically effected zone.

2.4.4 Fatigue in Friction Stir Welding

Fatigue life is critical for many applications including support structures in aerospace, automotive, platforms, and bridges in construction. Fatigue failure can be credited for the majority of structures that fail during service. According to the American Society for Testing and Materials (ASTM) fatigue is the process of progressive changes of the materials properties during repeated application of stresses or strains, which leads to crack formation or failure [96]. The repeated cycles stress on the materials cases the damage, the fatigue is also accumulated through the material life which means that the fatigue failure can occur at stresses that are still within the elastic region of the materials, this can lead to catastrophic failure with no warning that it is happening. Table 2-13 below outlines the factors that can influence the fatigue life of a material.

Table 2-13: factors that affect the fatigue life of a material [87]

Factor	**In what way**
Loading conditions	The stress state of the material, such as the stress amplitude and mean stress.
Surface Quality and Geometry	Notches and/or variations in the surface roughness along the sample leads to stress concentrators, where crack initiation can occur during loading.
Material History	Fatigue life changes with different materials, it is dependent on the history and nature of the materials. Heat treatments along with materials that have internal defects or residual stresses will change the fatigue life.
Environment	Temperature and corrosive environment surrounding the material will cause a change in the fatigue life

Fatigue testing can be performed by stress controlled or strain-controlled tests. The earliest methods of fatigue testing were performed using stress-controlled testing [97]. In stress-controlled testing a cyclic stress is applied to the test coupon until the sample fails. Failure can happen at any number of cycles and is dependent on the magnitude of the stress applied. Fatigue testing is done with either low-cycle fatigue testing or high-cycle fatigue testing. In low-cycle fatigue testing the stress applied to the sample is greater than the yield strength of the material which means that every stress cycle the material goes through plastic deformation, the plastic deformation accumulated and the material fractures a low number of cycles ($< 10^4$ cycles). Conversely, with high-cycle fatigue testing, the stress is below the yield strength of the material (in the elastic region) and the number of cycles before failure is much higher ($>10^4$ cycles) [87]. With stress-controlled loading, the fatigue endurance limit of the material is primarily influenced by the material's strength [10].

Fatigue was first systematically analyzed by August Wohler [83]. Wohler was working on analyzing the failure of railway axles. Fatigue tests plotted are known as S-N diagrams or

Wohler curves, they are plotted with the stress applied (σ_a) versus the number of cycles to failure (N_f), with a logarithmic scale being used for the number of cycles to failure. Typically, for an S-N curve there are between 6 – 12 samples tested at varying stress amplitudes, the number of cycles to failure is recorded [83]. Microscopic changed in the material can cause the fatigue behavior of different samples to vary greatly (even if tested at the same stress level), this can lead to a considerable amount of scattering with the fatigue data. The S-N curve provides the fatigue or endurance limit. This is the stress amplitude where the material can be subjected to an infinite number of cycles without failure. Since it is not possible to test to an infinite number of cycles, the stress amplitude which the material can reach 10^7 cycles is considered the fatigue limit.

Because there is a wide range of engineering applications for the FSW, it is imperative to understand the fatigue characteristics of the FSW process. There have been several studies on fatigue in FSW, these studies came up with several conclusions. It was observed that the fatigue strength of FSW joint (10^7 cycles) was lower than that of the base metal but the FSW welds had a higher fatigue strength than that of a wire feed and laser welded joint. As well studies done comparing the transverse fatigue strength to the longitudinal fatigue strength showed that the FSW transverse specimen had a lower fatigue strength than the longitudinal specimen. The surface quality of the FSW greatly effects the fatigue life of the joint. This is because the FSW welds have stress concentration which act as fatigue crack initiation points. A study by Hori *et al* showed that as the tool transverse speed/rotational speed (ν/ω) ratio increased the fatigue life decreased. This is because as the ν/ω ratio increases it caused an increase in non-welded grooves on the root side of the weld which form stress concentration points and lead to crack initiation points. Once these grooves are

removed (through sanding and polishing) the fatigue strength is no longer affected by the changing ratio. As well removing 0.5 mm from both the top of bottom of the FSW weld there is not difference between the longitudinal and transverse fatigue strength, these observations reveal that the fatigue life is limited by the surface defects and once they have been removed there is no significant defects, voids, or flaws with in successful FSW welds [21]. Fatigue life is also dependent on the microstructure of the material including the grain size, second phase particles, and its precipitates [98, 99]. Current research shows that in the FSW, fatigue strength is complicated and there have been no constant trends reported in literature up to this point [87, 100].

CHAPTER III

3 EXPERIMENTAL TECHNIQUES

3.1 Friction Stir Welding Sample Preparation

The materials used in this study were AM60 magnesium alloy and Al-10%Si aluminum alloy. These materials were FSWed together in AM60-AM60 and Al-10%Si-Al-10%Si butt welds. The chemical composition of these metals is outlined in Tables 2-4 and 2-10. The AM60 material was received as 4 mm thick plates which were produced by cold-chamber high pressure die cast (HPDC) technique. Figure 2-1 schematically shows the HPDC method in which the molten metal is injected at high speed and high pressure into the mold. The Al-10%Si material was received as 4 mm thick plate which was produced by a die casting method as well.

Prior to the FSW process of the plates, the materials (AM60 and Al-10%Si) were cleaned with ethanol and then dried. The FSW samples were then prepared by butt welding two similar sheet of material (either high pressure die-cast AM60 to AM60 or Al-10%Si to Al-10%Si) using a modified milling machine (Fig 2-20) and a proper clamping system (Fig 2-21).

The FSW tool used for both the AM60 and Al-10%Si welds was a three flat sided and tapered tool with a shoulder diameter of 15 mm and a pin length of 4 mm, made up of H13 tool steel with a slightly concave non-patterned shoulder (Fig. 3-1). Two similar tools were used, one specifically for the AM60 joints and the other specifically for the Al-10%Si joints.

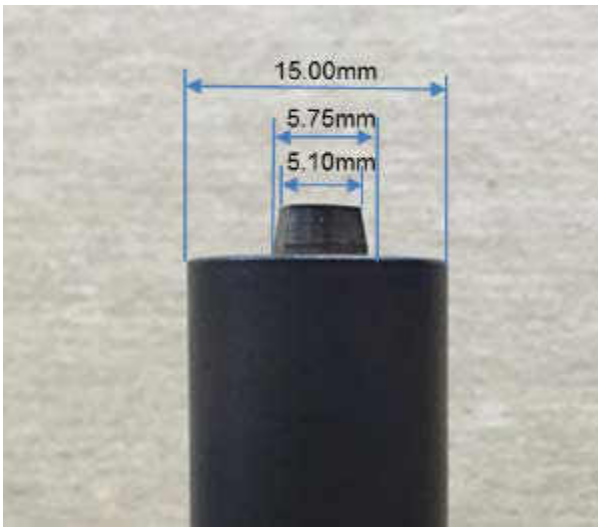

a b

Figure 3-1: The FSW tool, made from H13 tool steel, used in this study, a) isometric view, b) side view

To assess the effects of the FSW parameters for both the AM60 and the Al-10%Si butt joints, the welds were performed at several different tool rotational speeds and traverse speeds. Table 3-1 provides parameters used in this study for the AM60 butt weld joints and table 3-2 provides the parameters used in this study for Al-10%Si butt weld joints.

For each of these parameters, microstructural assessments, hardness measurements, fatigue tests, and fracture surface analysis were performed as described in this section. Figure 3-2 shows an image of a successful friction stir weld in the study.

Upon completion of the FSW tests, various samples were prepared for metallographic, hardness, and fatigue experiments.

Table 3-1: The FSW parameters, rotational and transverse speeds of AM60

Rotational speed (rpm)	Traverse speed (mm/min)
635	48
635	114
635	220
635	420
1200	48
1200	60
1200	114
1200	220
1200	420
1530	24
1530	48
1530	114
1530	220
1530	420

Table 3-2: The FSW parameters, rotational and transverse speeds of Al-10%Si

Rotational speed (rpm)	Traverse speed (mm/min)
635	114
635	420
1200	114
1530	114
1530	220
1530	420

Figure 3-2: An example of a successful FSW joint produced in this study (1200 RPM, and 420 mm/min).

Sample Geometry

To conduct the fatigue experiments, the welded materials were machined into dog-bone fatigue coupons with an orientation shown in Fig. 3-3. The dimensions of the fatigue coupons were used in accordance to the ASTM standard E466-15 [101]. The coupons were computer numeric controlled (CNC) machined from each weld, and for each of the parameters welded six to seven coupons were cut. The computer program AutoCAD was used to create the drawing, in accordance to ASTM standard E466-15, which the computer numeric controlled machine then used to cut the coupons. Figure 3-4 is an example of a coupon after it has been cut with the CNC machine. The full length of the test coupons is 65.8 mm (2.5917 in) with a gauge length of 6.0 mm (0.2362 in). The width of the gage area was 6.0 mm (0.2350 in). The transition from the grip section to the gage is machined as a gentle curvature to avoid any sharp changes in thickness, this is done to avoid any stress concentrators that would affect the results.

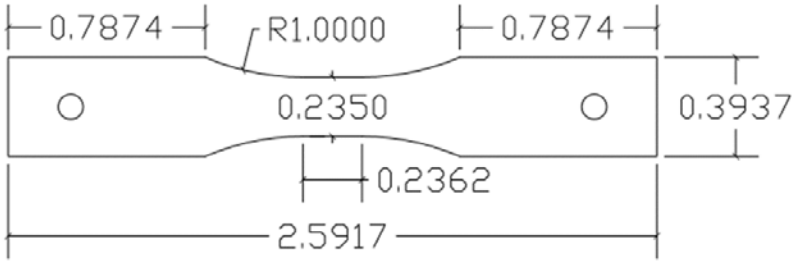

Figure 3-3: Shape and dimensions of the fatigue specimens in inches

Figure 3-4: Fatigue Coupon

The Metallographic samples were cut from the welds for the microstructural studies. These samples were cut along the cross section of the weld and were trimmed to 2 cm in width. Figure 3-5 is an example of how the metallographic sample was cut from the FSW joint. Similarly, to the metallographic samples, a small cross-section of each welded sample was cut for hardness measurements.

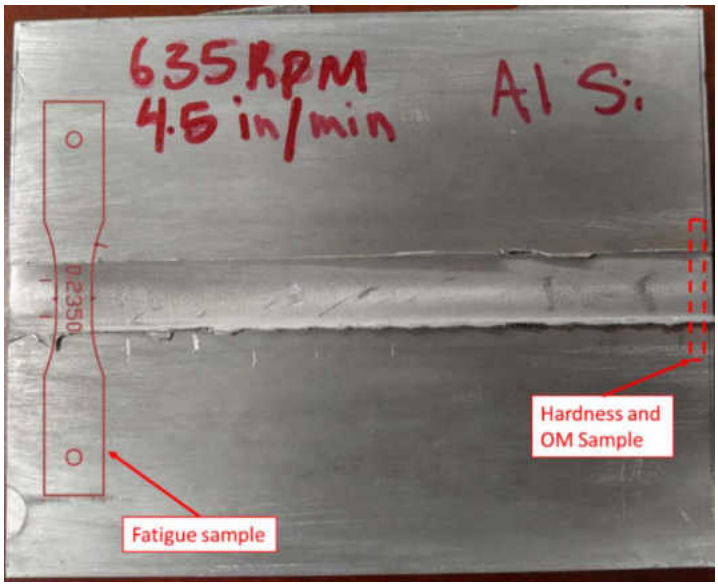

Figure 3-5: Schematic of how the metallographic samples were cut

Figure 3-6: Cutting the sample for hardness testing

3.2 Metallographic Analysis

3.2.1 Preparation of Surface Samples

As mentioned previously the metallographic samples were cut from the welds for the microstructural studies. The samples were mechanically polished according to the standard procedures using a range of sand paper from 80 grit to 1200 grit, followed by alumina paste and diamond on a cloth polisher. Once the manual polishing was completed and automatic polisher was used for 4 min, 5 lb. force and a speed of 10 for AM60 magnesium alloy and 10 min 5 lb. force and a speed of 10 for Al-10%Si aluminum alloy. All samples were polished until the surface was free of any scratches and had a mirror like finish (Fig. 3-7).

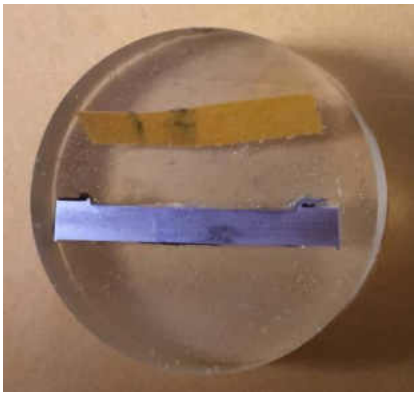

Figure 3-7: Mounted metallographic and hardness sample

3.2.2 Chemical etching

Upon polishing, the AM60 magnesium samples were etched using an etchant of 4.2 g Picric Acid, 10 ml distilled water, 10 ml acetic acid and 70 ml ethanol with etching time between 5 and 20 seconds. The Al-10%Si aluminum samples were etched using Keller's reagent (95 mL water, 2.5 mL HNO_3, 1.5 mL HCl, 1.0 mL HF). The polished Al-Si samples were immersed in the etchant for 35 seconds.

3.2.3 Optical Examination

Once the metallographic samples were etched they were observed using metallurgical light optical microscopy (OM). This was done using an Advanced Metallurgical Microscope EQ-MM-500T. For each AM60 magnesium sample and Al-10%Si aluminum sample, optical images of the microstructure were taken across the cross-section of the friction stir welded joint at different magnifications.

3.3 Hardness Testing

The hardness samples were prepared similarly to the metallographic samples. A small cross-section was cut from each welded sample which was 2 cm wide. The samples were mounted using the epoxy resin and then mechanically polished in accordance to the standard procedures (mentioned in the previous section) and seen in the preparation of the surface samples section. Once the samples were free of any scratches and had a mirror finish they were ready for the hardness measurements. Using a Vickers hardness tester at 300 g force and a dwell time of 15 seconds, the hardness numbers were recorded across the center line of the cross-section of the weld at successive intervals of 0.4 mm. Two other sets of hardness values were recorded above and below the centerline at an interval of 0.4 mm.

3.4 Fatigue Testing

Once the fatigue coupons were cut using the CNC machine, they were then polished with sand paper to remove any surface artifacts (burrs) and get a smooth surface finish. This helps to create a surface free of any stress concentrations which could cause initiation points for the fractures. This was done to be able to study the fatigue properties of the weld as a function of the tool traverse speed and the rotational speed (the FSW parameters)

unaffected by the surface artifacts induced by the FSW process. Figure 3-8 shows an example of the surface artifacts that can influence the outcome of the fatigue properties.

The fatigue tests were performed using a Bose ElectroForce 3510 with a 7.5kN load cell. The samples were all loaded the same into the fatigue machines with the advancing side upward. All fatigue tests were performed using a value of R = 0.1 (Fig. 3-8) and 50 Hz. The forces used were calculated as a percentage of the yield stress for a FSW joint of that material. The yield stress was taken from online resources and other studies using FSW AM60 [92, 5] and Al-10%Si [102, 103, 70] and was 230MPa and 230 MPa for both materials. Once the yield stress was known the average cross-sectional area of all six fatigue coupons from one FSWed sample was taken using a digital caliper. Equation 3-1 was used to calculate the force required to be at 100% of the yield stress.

$$F = \sigma A \qquad \text{Eq. 3-1}$$

From this value different percentages were taken for the force and the S-N curve was developed for each FSWed parameter of each type of material (AM60 and Al-10%Si). It was important to determine when the sample fails so the machine would stop running the fatigue test. It was programmed to stop if the displacement was greater than 1 mm; at this point the grips would not move and the cycles will no longer be counted. Tests were stopped upon reaching 10^7 cycles considering this as the fatigue endurance limit.

The fatigue specimen was subjected to load-controlled, tension-tension sinusoidal stress profile. This profile implies that it uses a stress ratio on R=0.1.

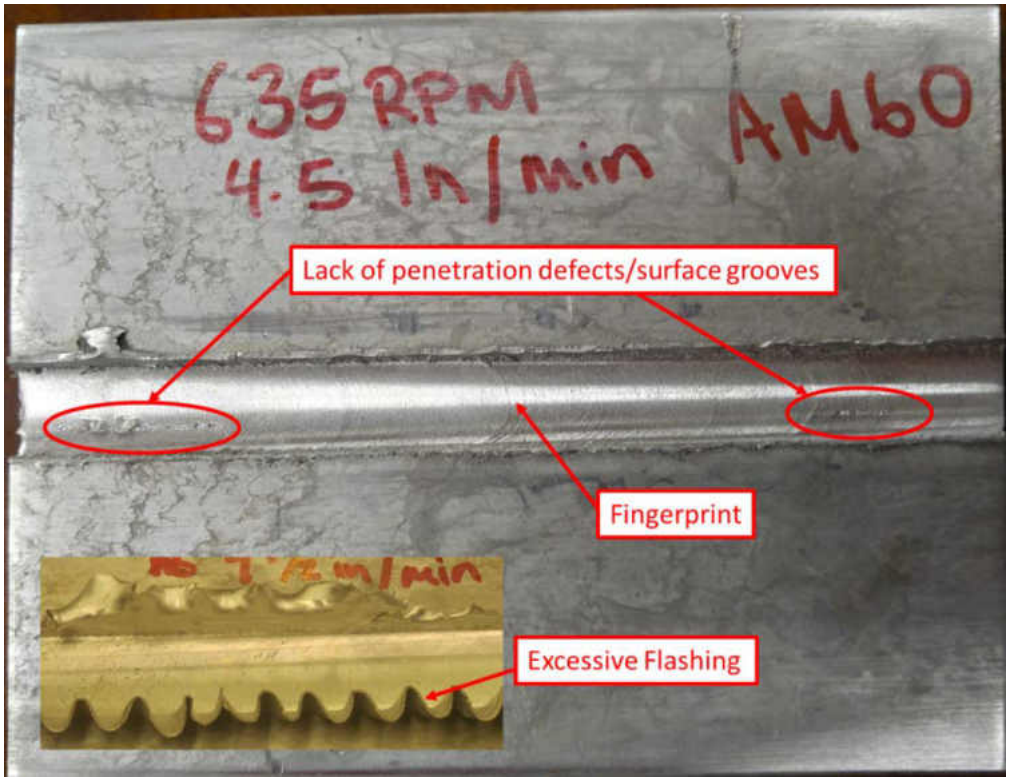

Figure 3-8: Surface artifacts from FSW 635 RPM, 114 mm/min

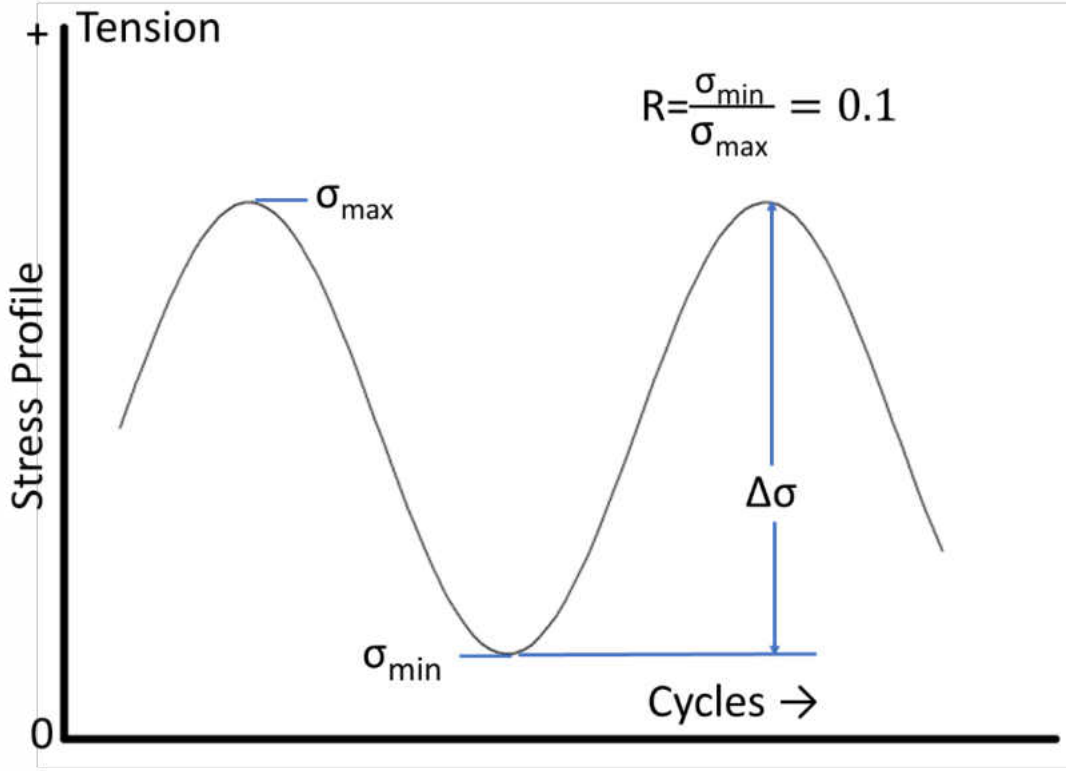

Figure 3-9: R=0.1 Stress profile schematic.

3.5 Fracture Surface Analysis

Once the fracture had occurred on the fatigue samples, fracture surface analysis was performed using scanning electron microscopy (SEM model FEI FEG 650). The fractography evaluations were performed to further look at fracture surface features and to establish the correspondence between fatigue response and the fracture surface. The samples were mounted on a stub using double-sided carbon tape. EDXS (energy dispersion X-ray spectrometry) measurements of composition were also performed.

CHAPTER IV

4 RESULTS AND DISCUSSION

The purpose of this chapter is to present and discuss the experimental results of this study. The results of the experiments include microstructural characterization, hardness distribution, fatigue response and SEM fracture analysis. The chapter is broken up into two sections investigation the following as cast alloys:

1: Magnesium Alloy AM60

2: Aluminum Alloy Al-10%Si

4.1 AM60 Mg Alloy

4.1.1 Microstructure Analysis

First a comparison of the microstructure of the non-processed (as-received) base alloy against the processed microstructures is performed to assess the microstructural evolutions. Figure 4-1 shows the microstructure, OM image and SEM micrograph, of the as-received high-pressure die cast (HPDC) AM60 alloy used in this study. Cast Mg alloys, including AM60, possess in-homogeneous microstructure including dendrites, second phases, intermetallic structures, and porosities at numerous length scales ranging from nanometers up to millimeters. The microstructure consists of α-Mg grains having an average grain size of 25 to 50 μm and a network-like eutectic β-$Mg_{17}Al_{12}$ phase and eutectic α along the grain boundaries. This is the expected microstructure for the alloy at ambient temperature based on the Al-Mg binary phase diagram presented in Fig. 4-3.

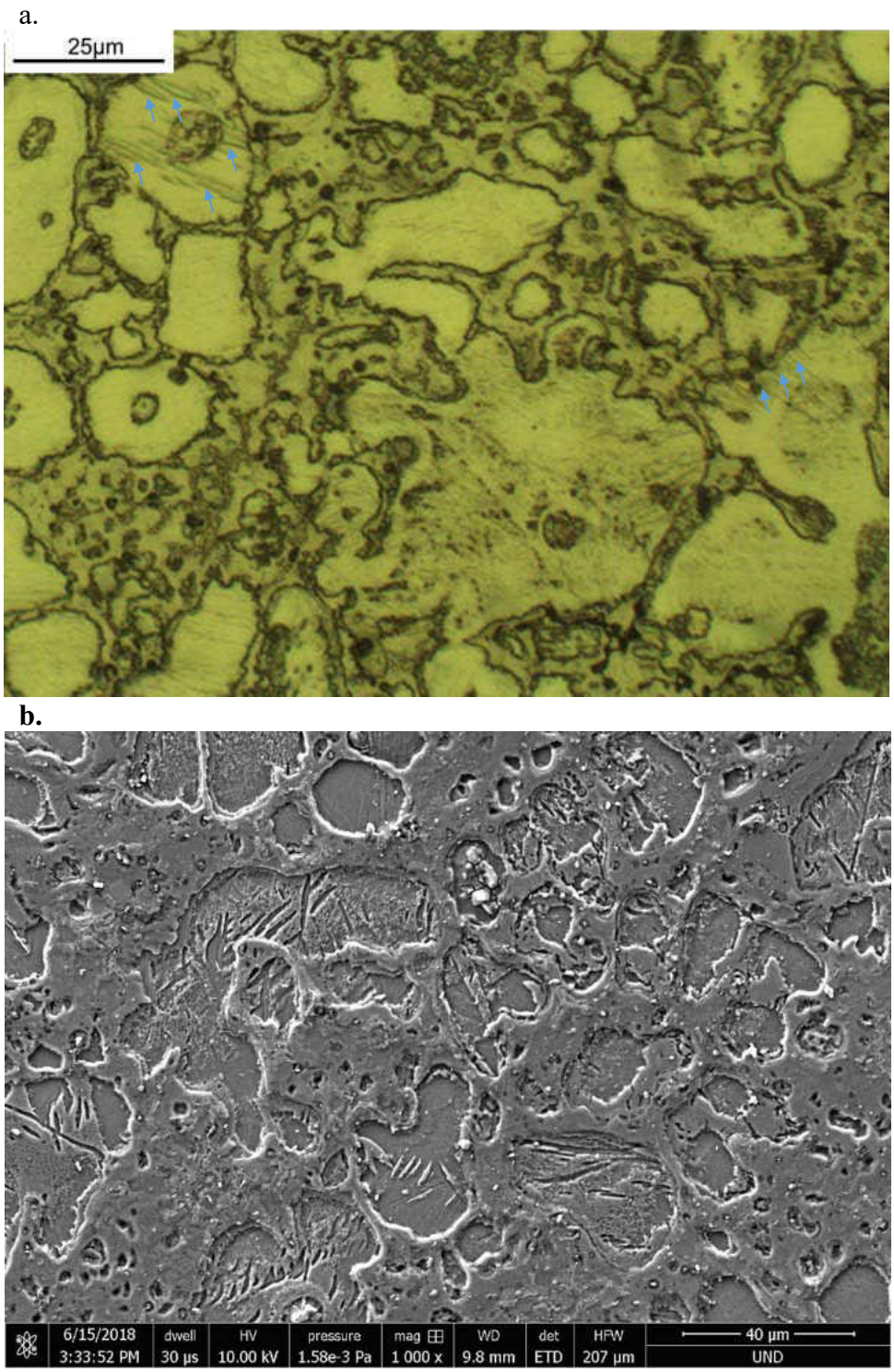

Figure 4-1: The optical micrographs of the microstructure of a) OM image, and b) SEM micrograph. The microstructure is characterized by α-solid solution of aluminum in magnesium (of limited solubility), α+β eutectic (where β is an $Mg_{17}Al_{12}$ intermetallic compound), Al_8Mn_5 intermetallic (dark spots), and twins (shown with arrows in OM image)

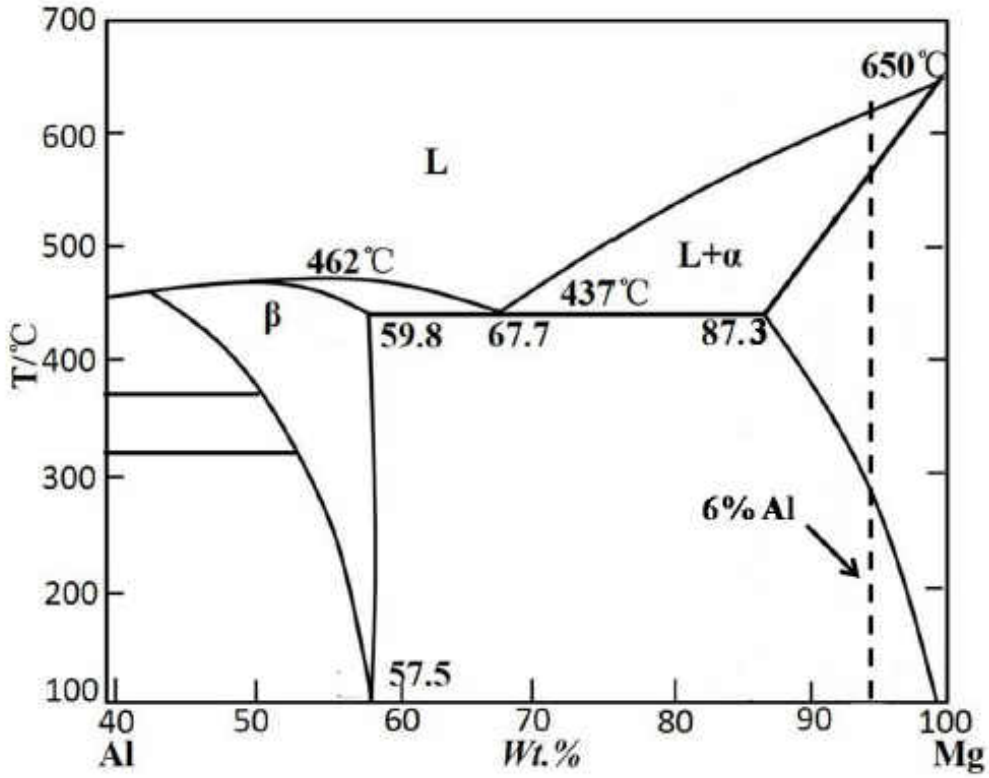

Figure 4-2: Al-Mg binary phase diagram [8]. The dashed line, schematically, shows the position of the AM60 alloy

Upon the FSW operation, the microstructure of the AM60 magnesium alloy changes significantly due to the severe plastic deformation imposed by the rotating tool. In the welded structure, the presence of a clear stirred zone (SZ) with fine equiaxed grains and thermomechanically affected zone (TMAZ) with elongated and tilted grains were found. Figure 4-3 and 4-4 provide the SEM and OM microstructures of the base metal (BM), the TMAZ and the SZ for the purpose of comparison. The SZ experiences intense plastic deformation at fairly high temperature due to the friction between the rotating non-consumable tool and the Mg matrix; this results in dynamic recrystallization and grain refinement in the stir zone (dynamically recrystallized fine grain structure) [32, 104]. Depending on the tool rotational and traverse speeds, the intense plastic strain imposed by the FSW tool occurs in a short period of time which does not provide enough time for

dynamically recrystallized grains, in the SZ, to grow. This leads to significant grain refinement in the SZ.

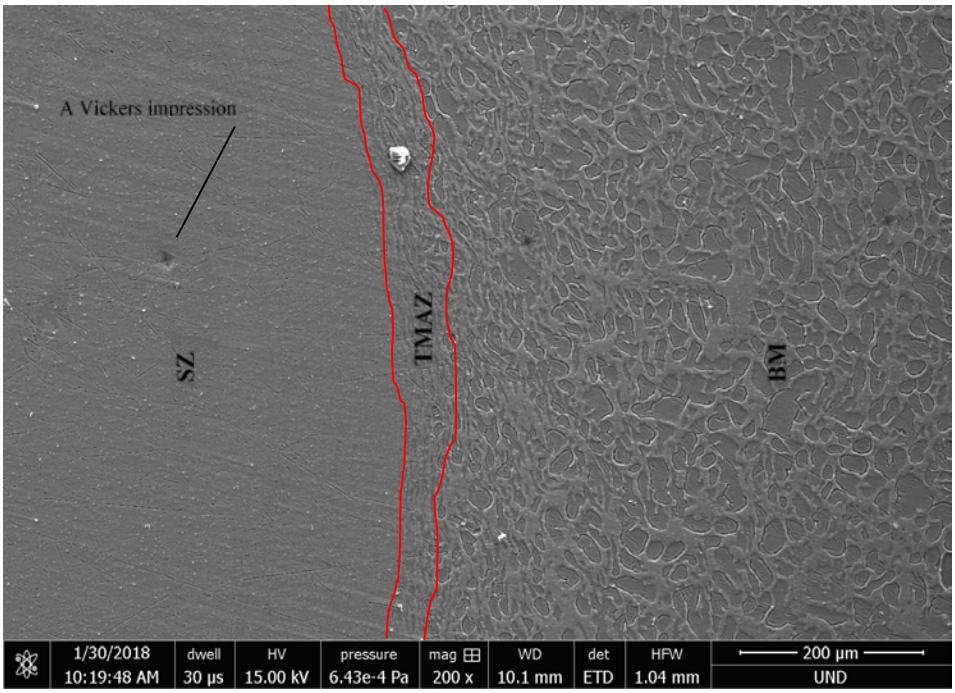

Figure 4-3: SEM micrograph showing of FSW 1200 RPM 420 mm/min stir zone (SZ), thermomechanically affected zone (TMAZ), and base metal (BM).

Continuous dynamic recrystallization (CDRX) and geometric dynamic recrystallization (GDRX) are two controlling mechanisms that drive grain structure evolution in the SZ during the FSW process [105, 106, 107, 108]. According to literature, the CDRX would occur in the SZ if the imposed deformation and strain rate (tool rotational and tool travel speed) remain high [109, 110, 111]. Refined and equiaxed grains along with high fraction of high-angle boundary areas are the main features induced by the CDRX [112, 113]. GDRX is another continuous recrystallization process perceived in microstructure zones with large strains (*i.e.* SZ in the FSW). As a result of the above mechanisms, the gains in the SZ are refine and equiaxed compared with the unprocessed base metal (BM).

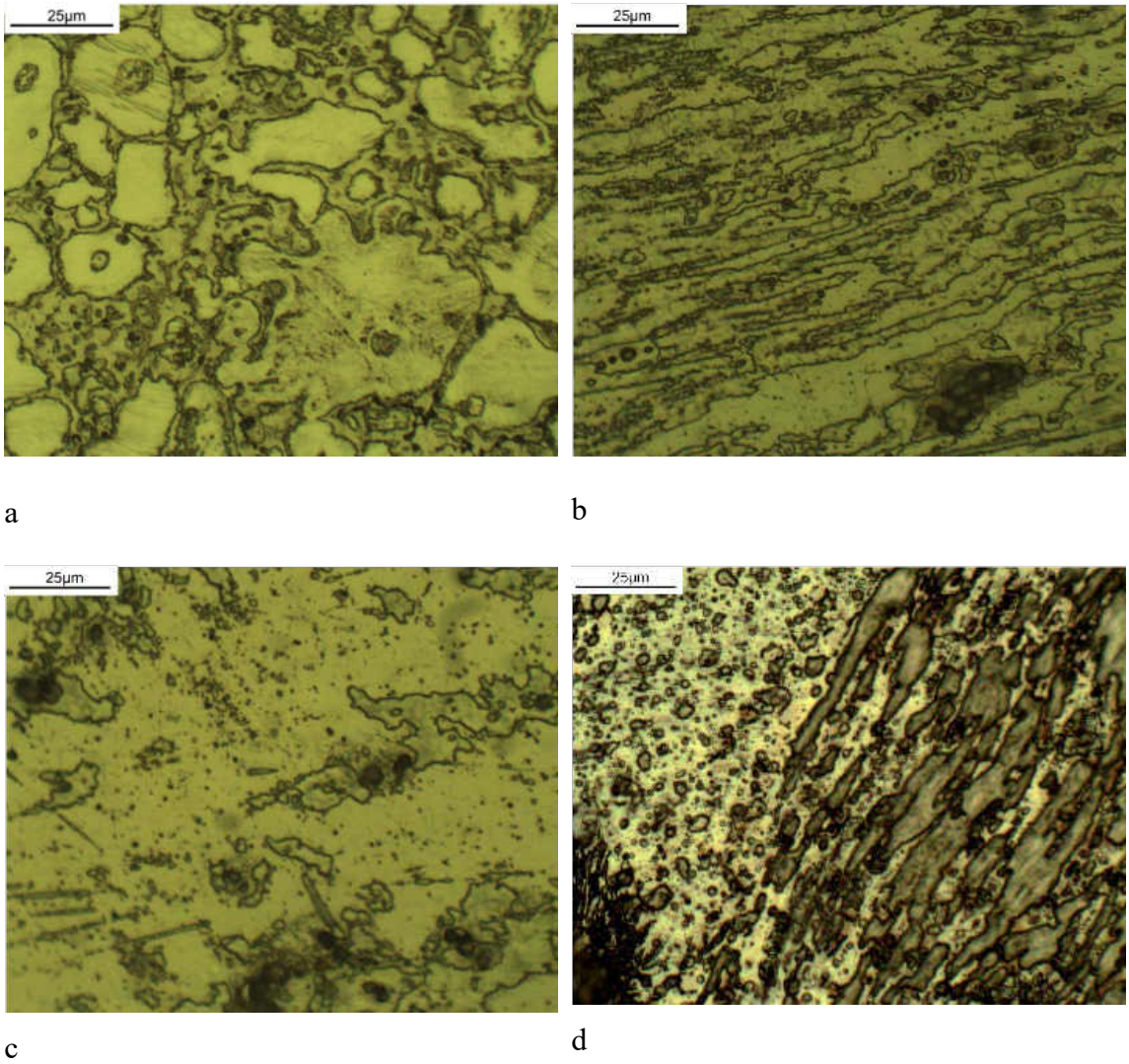

Figure 4-4: The optical micrographs of the microstructure of a) as received AM60 alloy, b) TMAZ (1200 RPM, 220 mm/min), c) SZ (1200 RPM, 220 mm/min), and d) interface between the SZ and the TMAZ showing equiaxed and elongated grains beside each other (635 RPM, 48 mm/min).

The temperature of SZ and the processing parameters (tool traverse and tool rotational speeds) can be correlated with the following relationship [114]:

$$T = T_m K \left(\frac{\omega^2}{\upsilon \times 10^4} \right)^{\alpha} \qquad \text{Eq. 4-1}$$

where T_m is the melting point, ω is tool rotational speed, v is tool travel speed, a and K are constants. By adjusting $\frac{\omega}{\upsilon}$ ratio one can obtain the proper temperature distributions in the SZ for a safe and sound weld (*i.e.* zones I or IV for the FSW of Mg alloys Fig. 4-8).

For Mg alloys, the constants are dependent on the processed materials, constants α and K vary between 0.04-0.06 and 0.65-0.85 respectively, and T_m= 638°C [32]. Through literature review and to the best of the author's knowledge, the constants α and K for AM60 Mg alloy have not been reported. Therefore, in table 4-1 the ration between the SZ and the melting temperatures are reported as a function of the constants α and K based on equation 4-1. It is worth mentioning that recrystallization temperature of the Mg-Al alloys series is ~0.5T_m [115]. Therefore, in almost all combinations of FSW parameters in the present study, dynamic recrystallization does happen. Also, heat input during the FSW process, Q_{FSW}, is directly related to rotational speed (RPM) and inversely related to travel speed (mm/min) [116, 117]:

$$Q_{FSW} \propto \omega \qquad \text{Eq. 4-2}$$

$$Q_{FSW} \propto \frac{1}{v} \qquad \text{Eq. 4-3}$$

According to Eqs. 4-2 & 4-3, increasing the $\frac{\omega}{\upsilon}$ ratio leads to an increase in the SZ temperature.

Unlike the as-cast microstructure, the grains in the SZ, due to the intense plastic deformation induced by the FSW rotating tool, are much refined (Figs. 4-5b and 4-5e). It is worth mentioning that one of the main applications of friction stir welding and processing is to locally modify the brittle microstructure, *i.e.* breaking down the dendritic grains, of the cast materials which eventually produces less brittleness in the microstructure

and better isotropy response of the materials. By moving away from the SZ, the TMAZ shows up which is highly susceptible to plastic deformation as well, however, it does not experience the full dynamic recrystallization because of insufficient strain and temperature induced through the rotating tool. This zone is characteristic of elongated (stretched) grains in an upward flowing pattern around the SZ. Further away from TMAZ, the heat affected zone (HAZ) exists which just experiences some thermal cycles but not necessarily any plastic deformation. Therefore, the microstructures of HAZ and the BM remain quite similar (the grain size in the HAZ might be slightly larger than that of the BM, HAZ grain coarsening).

Table 4-1: The FSW parameters, rotational and transverse speeds, and the SZ temperature according to Eq. 4-1

Rotational speed (rpm)	**Traverse speed (mm/min)**	$\frac{T_{SZ}}{T_m}$
635	48	$K(0.84)^{\alpha}$
635	114	$K(0.35)^{\alpha}$
635	220	$K(0.18)^{\alpha}$
1200	48	$K(3.00)^{\alpha}$
1200	114	$K(1.26)^{\alpha}$
1200	220	$K(0.65)^{\alpha}$
1530	48	$K(4.88)^{\alpha}$
1530	114	$K(2.05)^{\alpha}$
1530	220	$K(1.06)^{\alpha}$

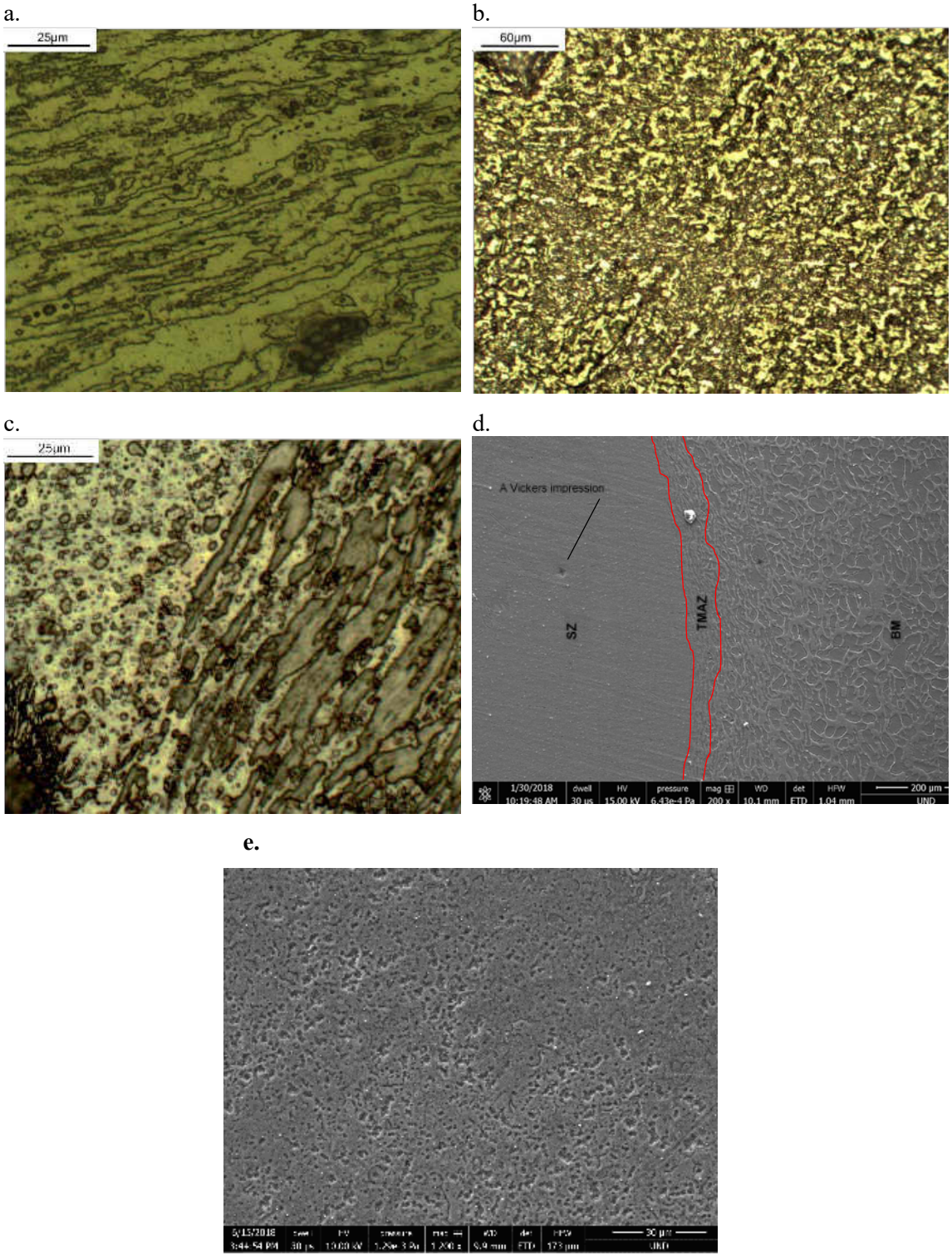

Figure 4-5: a) thermomechanically affected zone (TMAZ), b) stir zone (SZ), c) interface between the SZ and the TMAZ showing equiaxed and elongated grains beside each other, d) SEM micrograph showing the SZ, the TMAZ, and the base metal (BM), and e) higher magnification image of the SZ (1200 RPM, 48 mm/min).

The effects of the travel speed and the rotational speed are shown in figures 4-6 and 4-7. Regardless of the travel speed and the rotational speed the SZ microstructure consists of recrystallized equiaxed grains. It was observed that the grain size decreases as the travel speed increases (Fig 4-6 a → b) and increases as the rotational speed increases (Fig 4-7 a → b). This is as expected because the heat input and peak temperature decrease with increases travel speed or decreased rotational rate [21] and therefore there will be less driving force for grain growth. Also, at lower temperatures less time is available for the grain growth to occur which leads to the finer grain sizes.

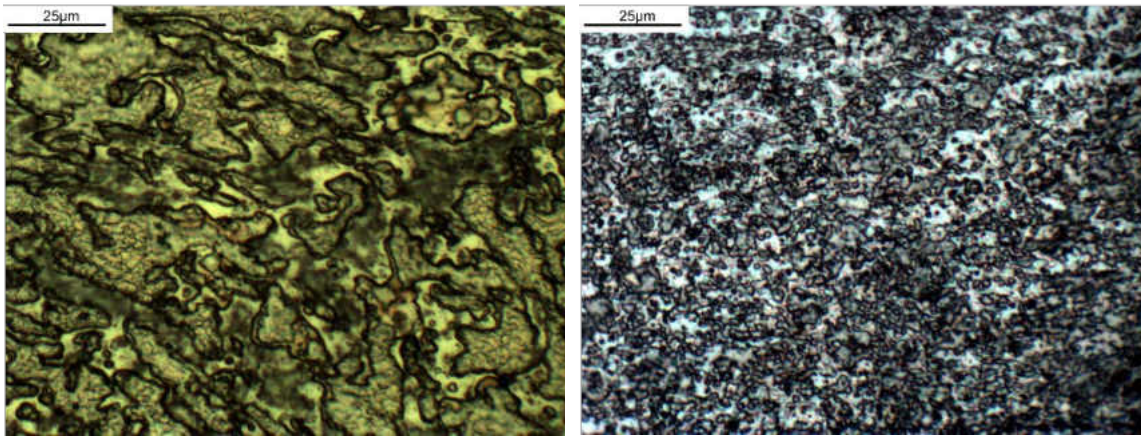

a) b)

Figure 4-6: Grain size of FSW SZ of a) 635 RPM, 48 mm/min and b)1200 RPM, 48 mm/min

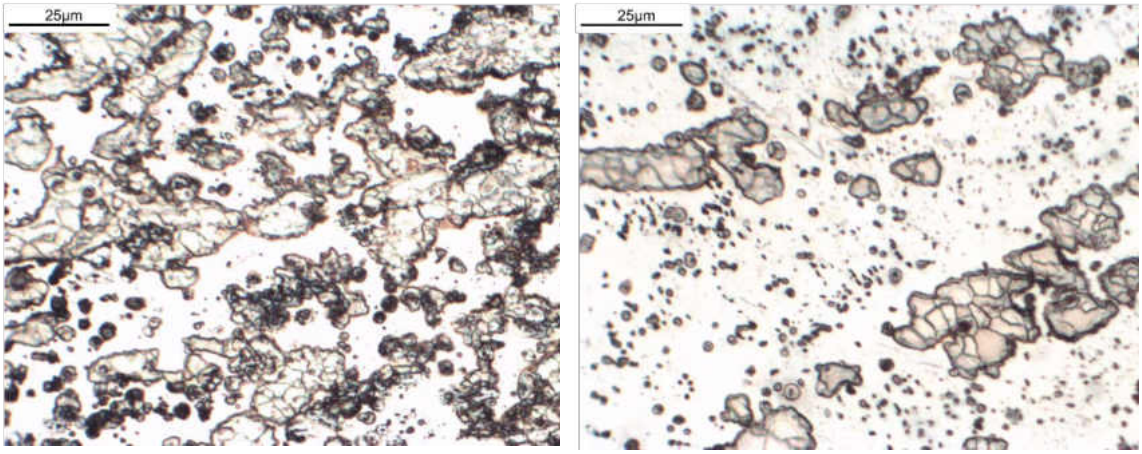

a) b)

Figure 4-7: Grain size of FSW SZ of a) 1200 RPM, 114 mm/min and b) 1200 RPM, 420 mm/min

4.1.2 Hardness Test Results

Hardness measurement is a convenient, and reliable method to assess the variations in mechanical properties, *i.e.* strength, across the weld according to the generated heat induced by the friction during the FSW process. The microhardness is heterogeneously distributed in the FSWed cross section which is due to different phenomena such as grain size, crystallographic texture, dislocation density, and distribution of precipitated within the SZ, TMAZ, HAZ, and the BM.

During the FSW process of cast Mg alloys, *i.e.* HPDC AM60, various defects such as porosity and voids can be possibly generated which can be attributed to improper selection of the tool rotational speed (w) and travel speed (v), and excessive/insufficient flow of material during the processing. In general, more heat is generated at higher tool rotational speed which creates sharper thermal (and therefore stress) gradient during the subsequent cooling process. On the other side, lower rotational speeds result in *colder* weld which causes insufficient material flow and generation of defects in the weld. With regard to traverse speed, mm/min, too high and/or too low speeds directly affect the generated heat input during the welding process and create various defects in the weld region. For instance, slow travel speed produces excessive heat input which may create incipient melting during the process which may not be the case for high travel speed [118, 119, 120]. Having said this, appropriate welding speed and rotational speed must be selected to produce promising joints with an acceptable performance during actual service conditions. Figure 4-8 provide a summary of correlations between tool travel and rotational speeds in the FSW process, this includes various scenarios (I to IV) [121].

- Scenario I provides a defect free weld.
- Scenario II, low travel speed and high rotational speed, observes too much heat input which creates various defects like cracks and voids as well as incipient local melting. Considering Scenario II, a decreasing trend in the strength (microhardness) measurements is expected. Indeed, generation of hotter SZ results in material softening due to the grain growth. Figure 4-9 shows an SEM image of the SZ including some coarse grain and second phase particles.
- Scenario III, high travel speed and low rotational speed, gives rise to insufficient heat input which produces lack of softening and inner voids and cracks.
- Scenario IV, high travel speed and high rotational speed, is associated with stable softening and plastic flow of material causing a defect free weld. When both traverse and rotational speeds are high, considering that $\frac{\omega}{v}$ ratio remains constant, the generated frictional and the adiabatic heat would not have sufficient time to dissipate resulting in confined and localized heating in the weld zone. In this condition the imposed strain and strain rate would be very large; this could in turn ease (promote) the flow of material to fill the produced cavity due to the FSW tool rotation within the material and provide a sound (defect-free) weld. In the present study, best quality welds were those made at the highest speeds (strain rate). It is worth mentioning that the strain rate in the FSW process could be estimated as $\dot{\varepsilon}_{FSW} = \frac{R_m 2\pi r_e}{L_e}$, where Rm is the average material flow rate; this is assumed to be about half of the tool rotational speed; R_m, r_e and L_e describe the effective radius and depth of the dynamic recrystallization (DRX) zone, respectively. The effective

radius of the recrystallized zone(r_e) is about π/4 of the shoulder radius. Similarly, the depth of DRX zone (L_e) is also π/4 of the plunge depth [122].

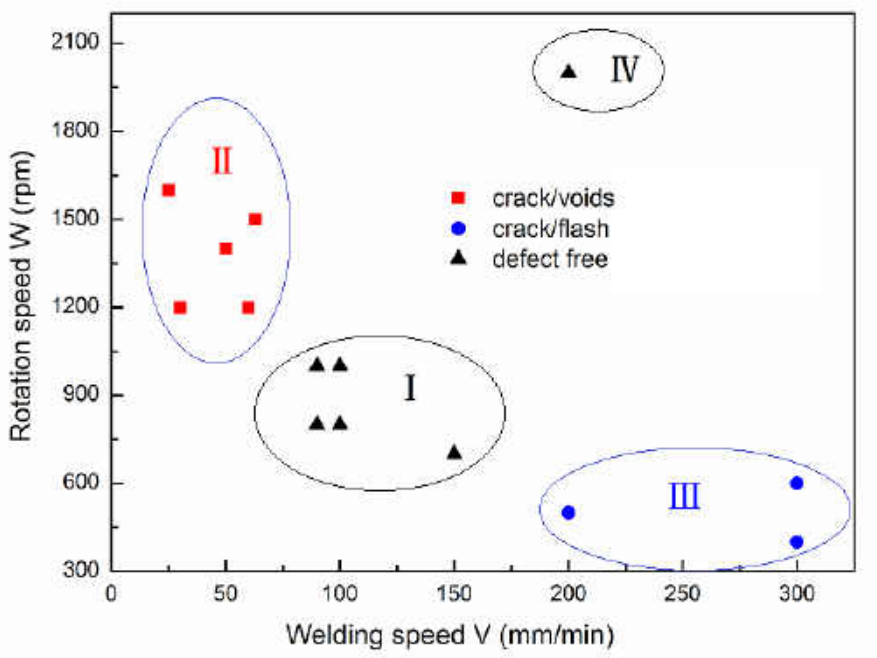

Figure 4-8: Relationship between the macro-defects and the welding parameters [121]

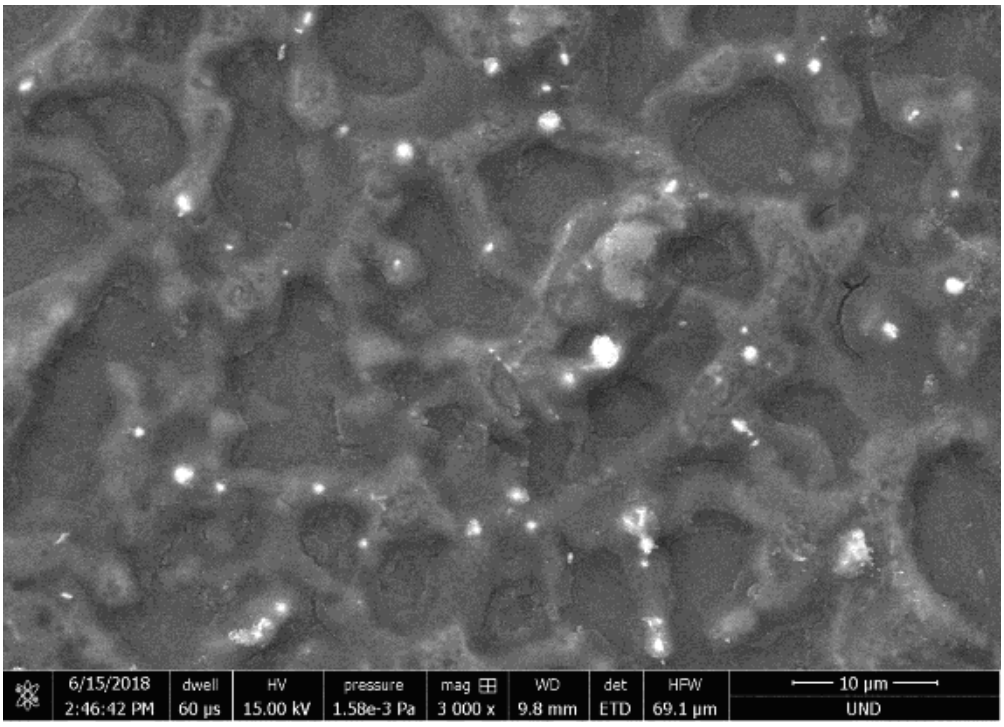

Figure 4-9: microstructure including equiaxed grains and second-phase particles (1530 RPM, 48 mm/min)

Considering the refined and equiaxed (dynamically recrystallized) grains within the SZ, the hardness values are greater than other zones, *i.e.* HAZ, TMAZ, and BM in all combinations of the FSW parameters (Figs. 4-10 through 4-13). Variations in hardness have been identified to follow the Hall-Petch relationship (hardness increase with decreasing grain size) [121]. Figure 4-10, for instance, shows the distribution of hardness across the joint at a constant rotation speed (635 RPM) and different feed rates (for the sake of comparison, different zones have been identified). The peak hardness is observed in the SZ and by moving away from the SZ, hardness decreases, and the least hardness belongs to the BM which is not affected by the mechanical action and/or thermal gradient of the welding operation. The hardness values in the TMAZ are higher than the ones in the HAZ; this is mainly attributed to the imposed plastic deformation in the TMAZ resulting in elongated, stretched and bended grains. There is not that much of difference in the hardness values of the SZ at different travel speeds. According to Eq. 4-1, at a constant rotational speed, with increase in travel speed, *i.e.* from 48 to 422 mm/min, heat input in the SZ becomes less which may slightly improve the hardness recording. It is worth noting that each provided hardness number is an average of three hardness values, however, to make the actual hardness values visible and not to make the hardness graphs busy (and even unreadable) the error bars are not provided. Figure 4-11 shows the hardness measurements at a constant rotational speed of 1200 RPM at different feed rates (48 mm/min to 422 mm/min). It is clear from the hardness values that the highest hardness values, in the stir zone, belong to the one with slowest travel speed. At a constant rotational speed, with decreasing the travel speed, the volume of material being processed per each tool revolution decreases and there will be more time available for the generated heat in a

smaller volume of material to dissipate. This, in turn, leads to decreasing the instantaneous temperature and increasing the work hardening (strength) of processed material. In other words, an increase in the travel speed (from 48 mm/min to 422 mm/min in this study), increases the friction and therefore produced temperature. This can indeed result in dynamic recovery (dislocation rearrangement and annihilation) and grain growth, and therefore decrease in the strength (hardness).

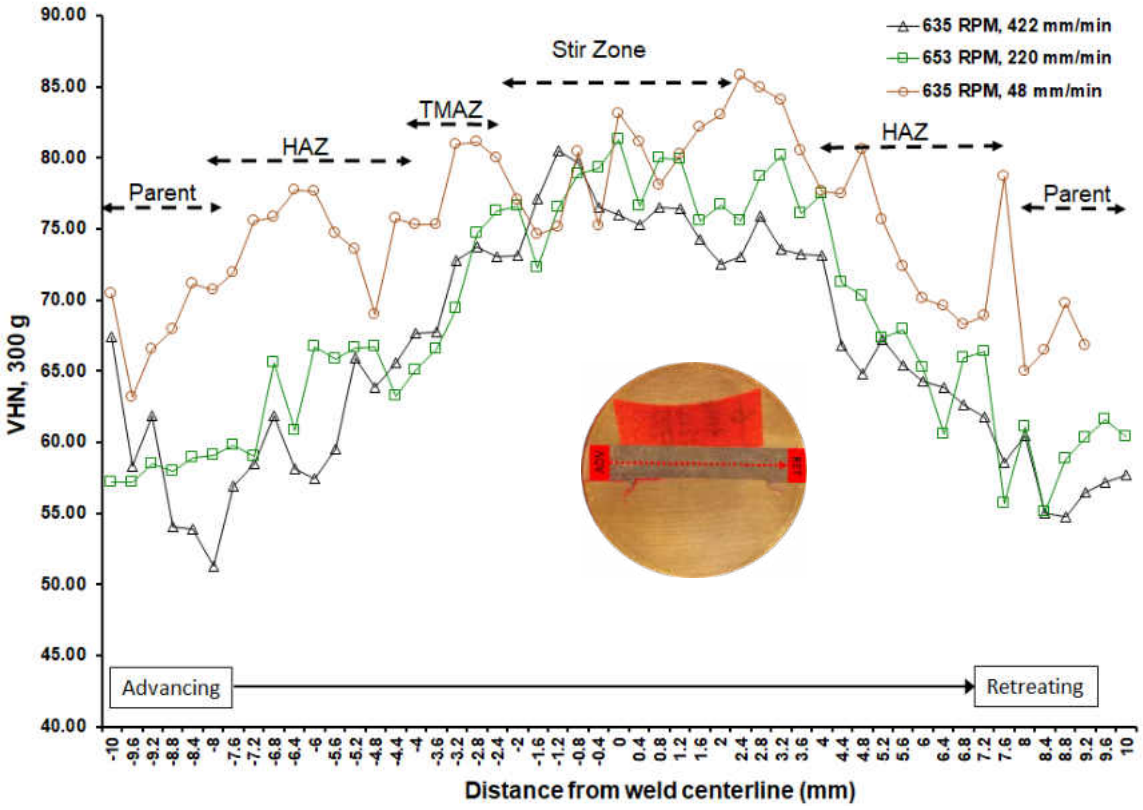

Figure 4-10: Hardness distribution across the weld at a constant rotation speed of 635 RPM and different travel speeds. Various zones have been identified in the image.

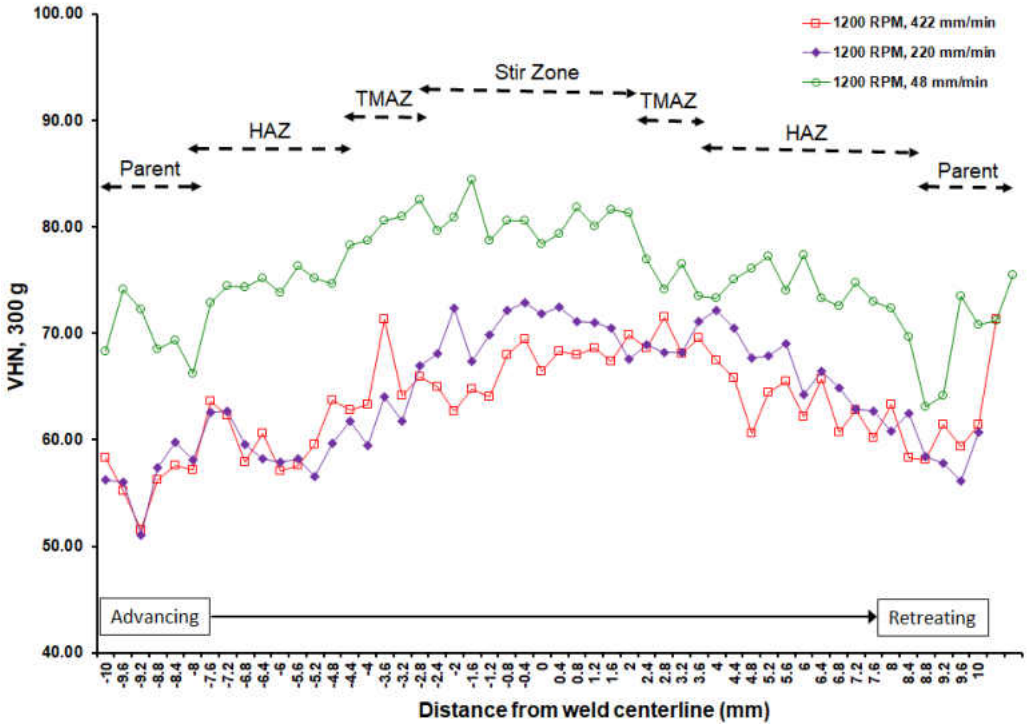

Figure 4-11: Hardness distribution across the weld at a constant rotation speed of 1200 RPM and different travel speeds. Various zones have been identified in the image.

Figure 4-12 shows the hardness variations at a constant travel speed of 48 mm/min and different tool rotational speeds of 635, 1200, and 1530 rpm. As observed, with increase in the RPM, the hardness level decrease in all regions of the weld. According to Eqs. 4-1 and 4-3, higher RPM creates a hotter SZ; this can directly result in (*i*) grain growth, (*ii*) dissolution of α-$Mg_{17}Al_{12}$ phases, precipitates, and (*iii*) dissolution of AlMnSi intermetallic compounds within the matrix. These phenomena contribute to the decreased strength (*i.e.* hardness) in the welded zone. The same trend is observed in Fig. 4-13 where travel speed is fixed at 220 mm/min and rotational speeds are varied. The lower the RPM, the higher the hardness numbers are and vice versa.

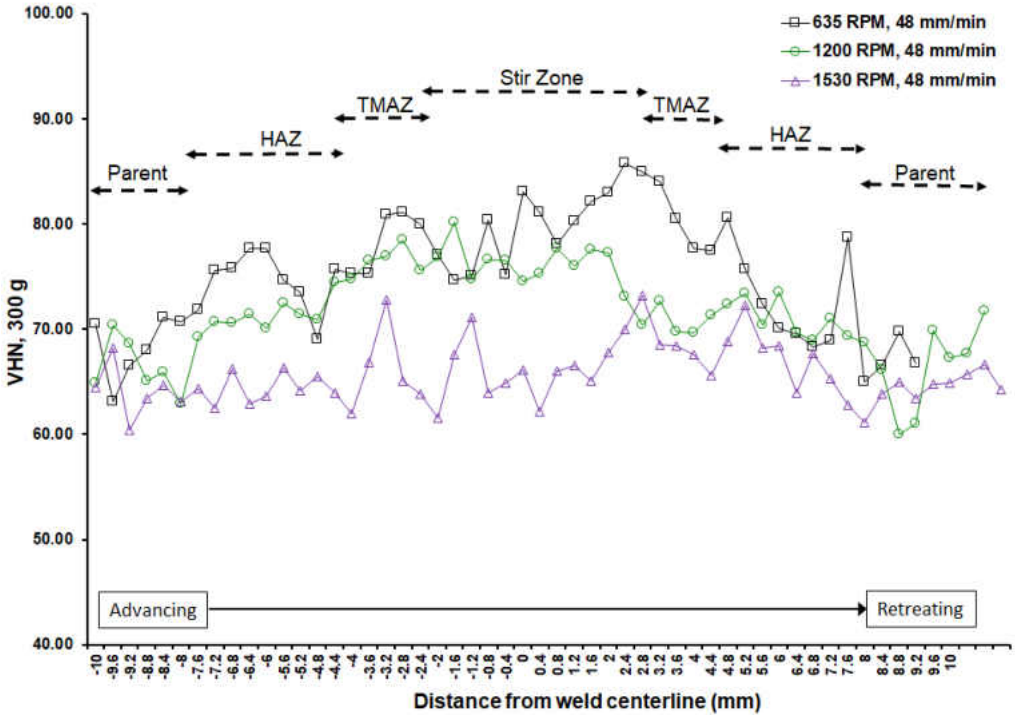

Figure 4-12: Hardness distribution across the weld at a constant rotation speed of travel speed of 48 mm/min and different travel speeds. Various zones have been identified in the image.

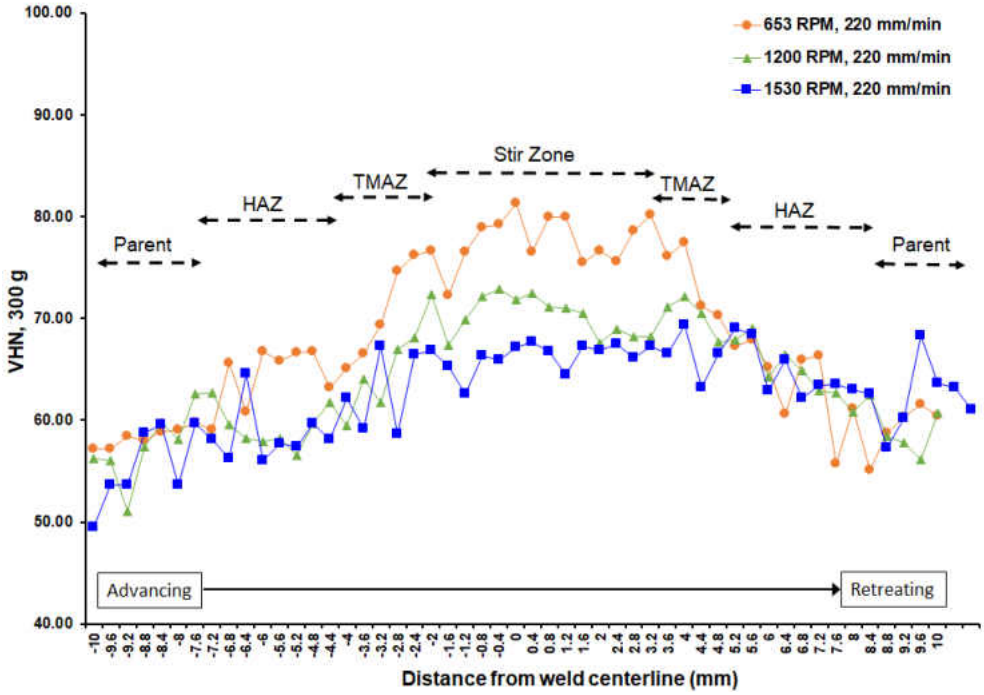

Figure 4-13: Hardness distribution across the weld at a constant rotation speed of travel speed of 220 mm/min and different travel speeds. Various zones have been identified in the image.

4.1.2.1 Design of experiment (DOE) study on hardness variations.

In this study a DOE approach was employed to assess the effect of two important FSW parameters, ω and *V*, on the local hardness measurements of the FSWed die-cast AM60 Mg alloy in the SZ. In the parametric design of the experiments the factorial method is used to study the effect of tool rotational and travel speeds on the strength (hardness) of the joint. To analyze the effect of the two parameters, a 32 factorial design was chosen. A 32 factorial design has three levels of each of the two factors. The study used fixed factors, three tool rotational speeds (635, 1200, and 1530 RPM) and three transverse speeds (48, 220, and 422 mm/min), resulting in nine experimental units. Each of the nine experimental units containing five replicates (five hardness values were taken from the SZ of each sample). With three levels of each factor, the data points in the middle allow for a curved fit response function. The design used is shown below in Table 4-2 and Figure 4-14. This design allowed for an economical investigation into the cause and effect relationships of the significance of the two variables at hand.

Table 4-2: The 32 Factorial arrangement; 0, 1, and 2 stand for low, medium and high quantities, respectfully.

Factor A	Factor B
0	0
1	0
2	0
0	1
1	1
2	1
0	2
1	2
2	2

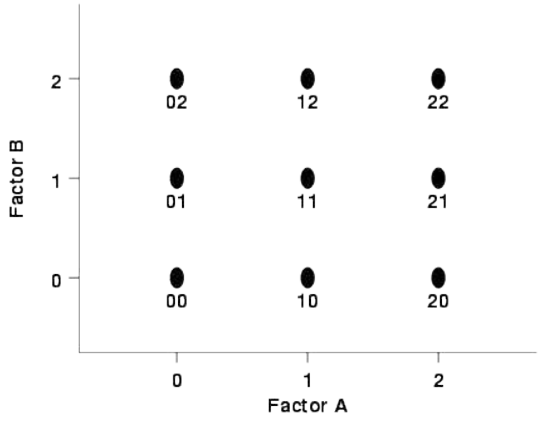

Figure 4-14: A 32 design scheme (0, 1, and 2 stand for low, medium, and high quantities, respectively).

Table 4-3 shows sum and mean of the collected hardness data at different tool rotational and tool travel speed. The main effects (αi and βj) are calculated by equations 4-4 and 4-5:

$$\alpha_i = \bar{\mu}_{i.} - \mu \qquad \text{Eq. 4-4}$$

$$\beta_i = \bar{\mu}_{.j} - \mu \qquad \text{Eq. 4-5}$$

Table 4-3: Sum and mean of collected data

Rotational Speed RPM	Travel Speed (mm/min)						Row Total	Row Means
	48		220		422			
635	87.20	87.40	80.20	79.80	84.00	82.70	1242.10	**82.81**
	87.90	87.90	83.90	80.00	76.40	80.80		
	85.30	**435.70**	76.80	**400.70**	81.80	**405.70**		
1200	85.30	86.50	71.20	72.00	66.10	70.80	1130.80	**75.39**
	85.60	85.60	71.80	71.10	69.90	68.00		
	87.80	**430.80**	72.70	**358.80**	66.40	**341.20**		
1530	69.80	68.20	79.00	79.70	65.50	68.10	1075.70	**71.71**
	67.60	69.40	78.10	80.60	68.20	64.50		
	69.80	**344.80**	78.50	**395.90**	68.70	**335.00**		
Column Total	1211.30		1155.40		1081.90		3448.60	
Column Means	**80.75**		**77.03**		**72.13**			**76.64**

The main effects are calculated in Table 4-4 and displayed graphically from the Minitab output in Fig. 4-15

Table 4-4: Main Effects

Main Effect				
Rotational Speed (RPM)	Travel Speed (mm/min)			Rotational Speed main effects
	48	220	422	
635	87.14	80.14	81.14	**6.17**
1200	86.16	71.76	68.24	**-1.25**
1530	68.96	79.18	67	**-4.92**
Travel Speed Main Effects	**4.12**	**0.39**	**-4.51**	

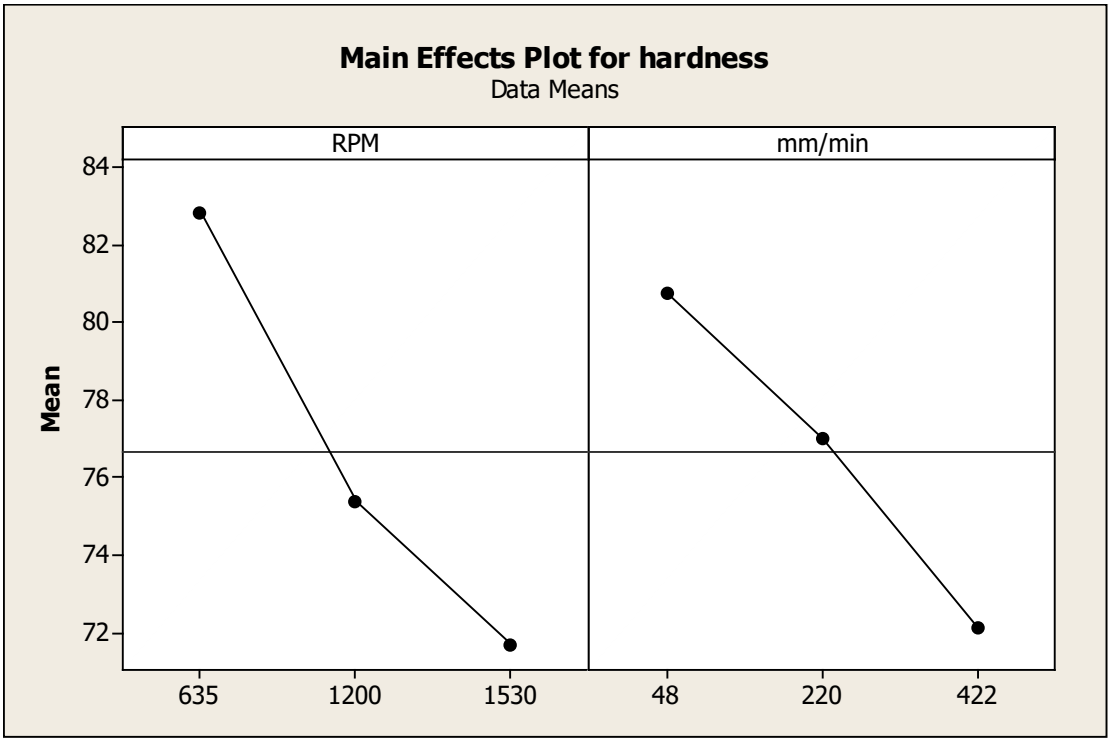

Figure 4-15: Minitab output showing the main effects plot for the hardness values.

The interaction effects are calculated using equation 4-6.

$$y = \mu_{ij} - \bar{\mu}_{i.} - \bar{\mu}_{.j} + \mu \qquad \text{Eq. 4-6}$$

The interaction effects are calculated in Table 4-5 and displayed graphically from the Minitab output in Fig. 4-16.

Table 4-5: Interaction effects between parameters

Interaction Effects			
Rotational Speed (RPM)	Travel Speed (mm/min)		
	48	220	422
635	**0.215556**	**-3.05778**	**2.842222**
1200	**6.655556**	**-4.01778**	**-2.63778**
1530	**-6.87111**	**7.075556**	**-0.20444**

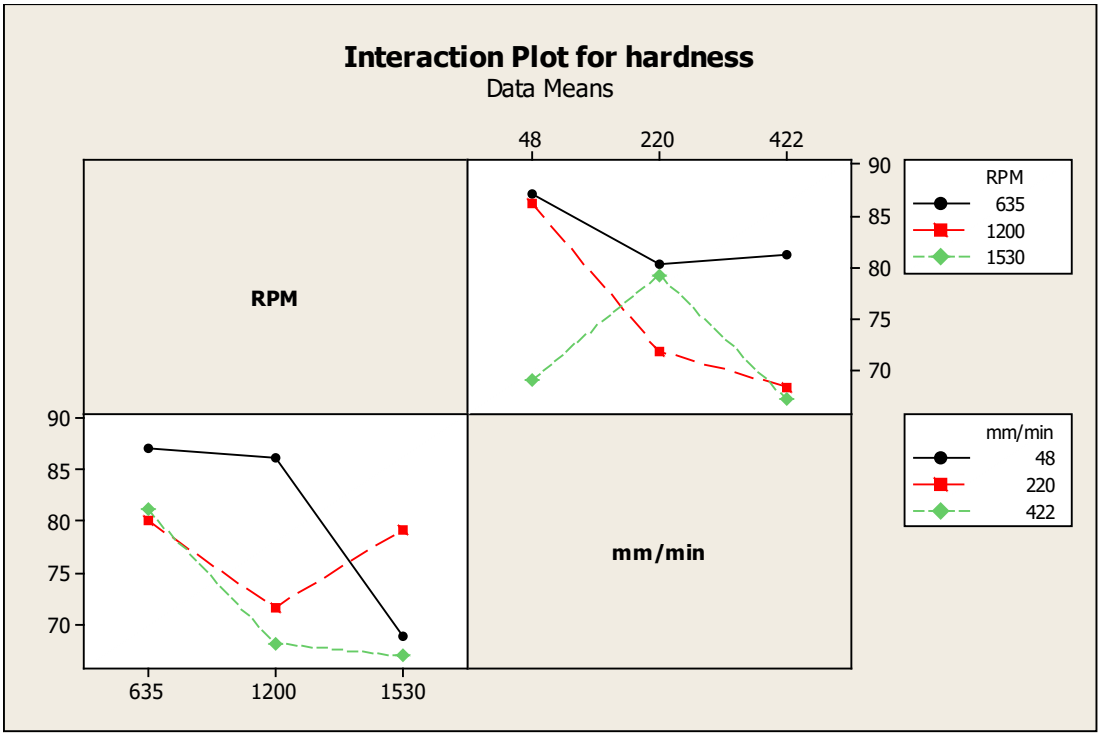

Figure 4-16:Minitab output showing the interaction effects plots for the hardness values

Analysis of variance (ANOVA) [123, 124, 125], a collection of statistical models and their associated procedures (such as "variation" among and between groups) used to analyze the differences among group means, were done by using equations 4 through 20 in Appendix A, considering *n* (number of replicates) = 5, a (number of levels tool rotational speed) = 3, and b (number of levels of the transverse speed) = 3. ANOVA calculations were also made in Minitab. The results from the output calculations are displayed in Table 4-6 and the output from Minitab is displayed in Appendix B.

Table 4-6: ANOVA statistical estimates

ANOVA

Source of Variation	*SS*	*df*	*MS*	*F*	*P-value*	*F crit*
Rotational Speed	958.0591	2	479.0296	158.3685	1.44E-18	3.259446
Travel Speed	561.5871	2	280.7936	92.83114	6.18E-15	3.259446
Interaction	910.9449	4	227.7362	75.29023	5.56E-17	2.633532
Within	108.892	36	3.024778			
Total	2539.483	44				

Upon calculating the results, the model adequacy needed to be verified. Figure 4-17 exhibits four different plots used to verify the adequacy of the model. These plots include the normality assumption, residuals, histogram, and the residuals versus observation order, that verify the adequacy of the model. None of these plots exhibit anything out of the ordinary. The normality plot shows no severe indication of non-normality, nor evidence of any possible outliers. The residuals plot reveals nothing abnormal or of unusual interest. Histogram plots show the central tendency, spread, and variability. This histogram also shows nothing from the ordinary as with the residuals versus observation order.

The purpose of this study was to determine if changing the tool rotational speed and the transverse speed influenced the hardness of the friction stir welded joints. Looking at the ANOVA results (Table 4-6) the $F_{rotational}$ speed = 158.37 and $F_{transverse}$ speed = 92.83, for both $F_{critical}$ = 3.26 with a P value of almost 0. Therefore, the main effect of both the tool rotational speed and the transverse speed are significantly different and do influence the hardness. Also, looking at the interactions $F_{interactions}$ = 75.29 with the $F_{critical}$ = 2.63 and again a P value of almost 0, it can be concluded that there is a significant interaction between the tool rotational speed and the transverse speed. From the main effects plots (Figure 4-15), it is shown that the lower tool rotational speed and transverse speed yield

higher hardness value. Looking at the interaction plots (Fig. 4-16), it is visually shown there are significant interactions between the tool rotational and transverse speeds by the lack of parallelism of the lines.

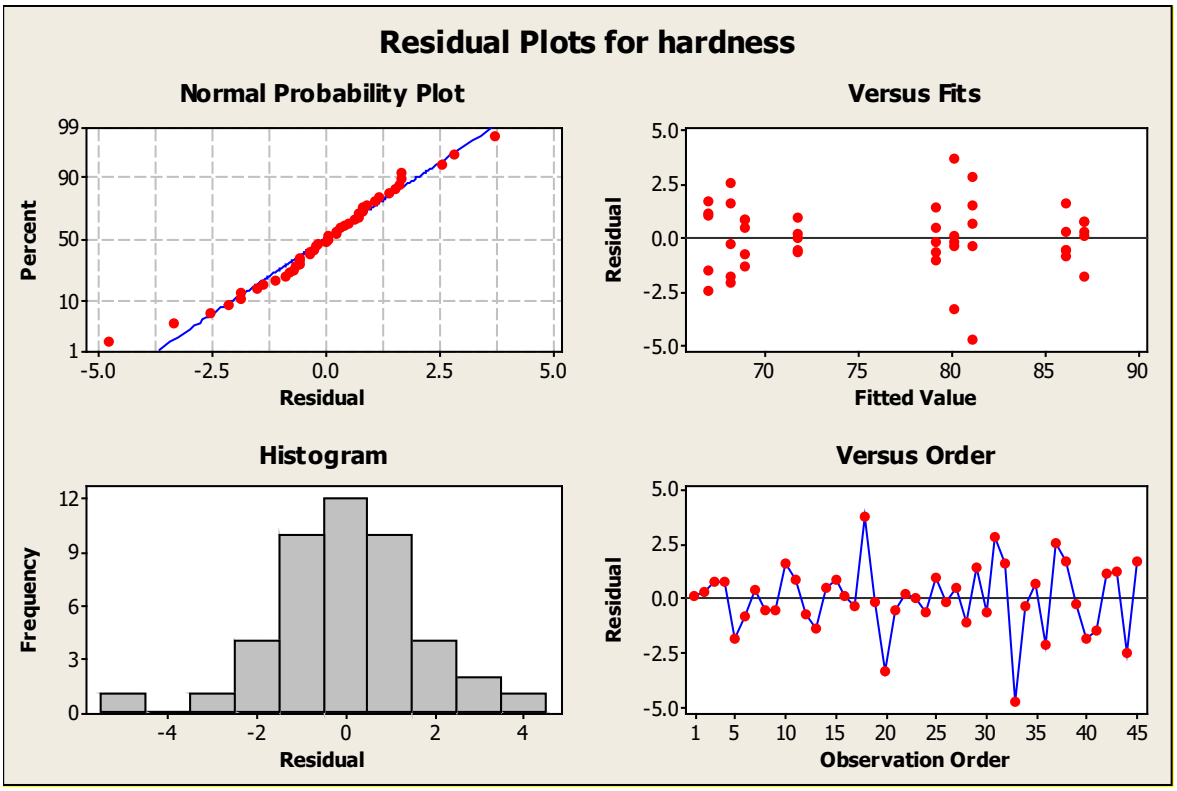

Figure 4-17: Plots of model adequacy checking

4.1.3 Fatigue Response

In vast Mg alloys, current knowledge and predictions lead to a working hypothesis: the structures are not stable over time or under dynamic loading. Strength and fatigue resistance decrease as casting pores and grains continue to grow. The evolution of fatigue damage appears brittle, cracks initiating at intersections between pore surfaces and grain boundaries and growing by linking up with nano-voids nucleating on the boundaries ahead of them. This is enhanced by a combination of grain boundary migration and reductions in the density of diffusion paths. Considering existing potentials on dynamic application of the AM60 Mg alloy, research on fatigue characteristics of FSWed AM60 can provide

significant information on solid-state weldability of cast Mg alloys as a challenging material for fusion welding operation. Besides, fatigue property/ microstructural feature correlations provide a distinct path for optimizing component design and multi-scale modeling.

In fatigue testing of the cast FSWed specimens, crack initiation points are associated with either surface marks (*i.e.* surface circular arcs due to tool rotation and translation, surface grooves and flashes, surface voids made by oxides trapped during casting, etc.) or with internal defects (*i.e.* casting porosities and micro-cracks, cavity created due to insufficient heat input, etc.) [8, 9]. Figure 4-18, schematically, shows common flaw types which can be generated in friction stir welding process. These internal and external defects make the material more sensitive to crack nucleation and, and crack propagation. In fatigue testing of the AM60 Mg alloy, fatigue crack can either propagate across the α-Mg dendritic cell or can preferentially through $Al_{12}Mg_{17}$ phase on the α-Mg grain boundaries.

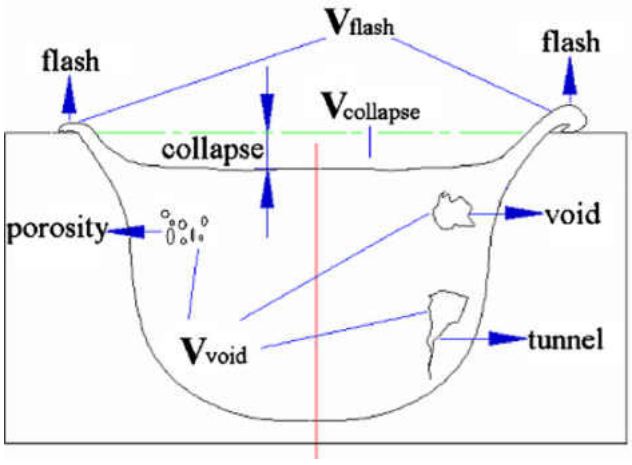

Figure 4-18: Schematic of common flaws generated in the FSW process [126].

For the engineering and structural applications, where fatigue is a potential mechanism of failure, the area of interest is fatigue life beyond 10 million cycles, in particular, for those alloys that do not necessarily show clear endurance limits (*i.e.* aluminum and magnesium).

The available literature on the effect of FSW parameters on fatigue performance (stress/number of cycle (S–N) and fatigue crack propagation behavior) are rather contentious. In several studies [64, 127, 128, 129, 21], it has been reported that fatigue strength of friction stir welds is lower than those of the base metal, however, in some other papers the fatigue limit was reported comparable to (or better than) those of base metal [94, 130, 131]. One main aspect that must be considered when studying fatigue response in the FSW is residual stress created in the weld zone. In the FSW process, rigid clamping is used, to position the plates for the FSW run, which creates large restraint on the welded plates (this is not necessarily the case in conventional fusion-based welding operations). These restraints obstruct the contraction of the SZ and the HAZ during subsequent cooling generating residual stresses. In particular, tensile residual stresses impart adverse effects on fatigue life of the welded parts compared with non-welded parts. The FSW parameters and clamping forces can directly affect the type and magnitude of the residual stresses created in the weld. With increasing tool transverse and tool rotational speeds, strain, strain rate, and tensile residual stresses in the HAZ have been reported to increase (this is explained by higher cooling rate) [132]; this results in a decrease in the fatigue life of the welded parts.

Figure 4-19 shows stress/N_f trends at a constant RPM of 1200 and two different rotational speeds of 48 and 114 mm/min. At a constant rotational speed, with increase in the tool travel speed the peak temperature in the SZ and the heat input decrease (see Table 4-1). Decrease in the heat input results in higher hardness in the SZ and therefore improved fatigue life (the higher the hardness the higher the fatigue life [116]). Figure 4-20 shows the stress/N_f graphs a constant travel speed of 114 mm/min and different RPMs. At a

constant travel speed, with increase in the RPM the SZ becomes hotter (see Table 4-1) and therefore grain growth is promoted. This results in a reduction in the hardness and a lower fatigue life. Considering Figs. 4-19 and 4-20, one can see that the weld heat input possesses a significant influence on fatigue strength of the welded joints although the relationship is non-linear. As mentioned before, fatigue failure in the FSWed samples was either caused by internal voids in the weld nugget or by the FSW fingerprints (*i.e.* surface marks that act as crack initiation sites). According to the hardness profiles of the FSWed samples, fatigue cracks must initiate in the HAZ and TMAZ due to the low hardness values of these regions. This is in agreement with results reported by Montgomery *et al* [28], Rajakumar *et al* [133] and Mohamed and Manurung [134]. Figure 4-21 shows the correlations between N_f and the SZ hardness values at different travel speeds. With increase in the travel speed, the hardness increases which results in a better fatigue life (a better weld quality is achieved here with less density of internal and surface defects).

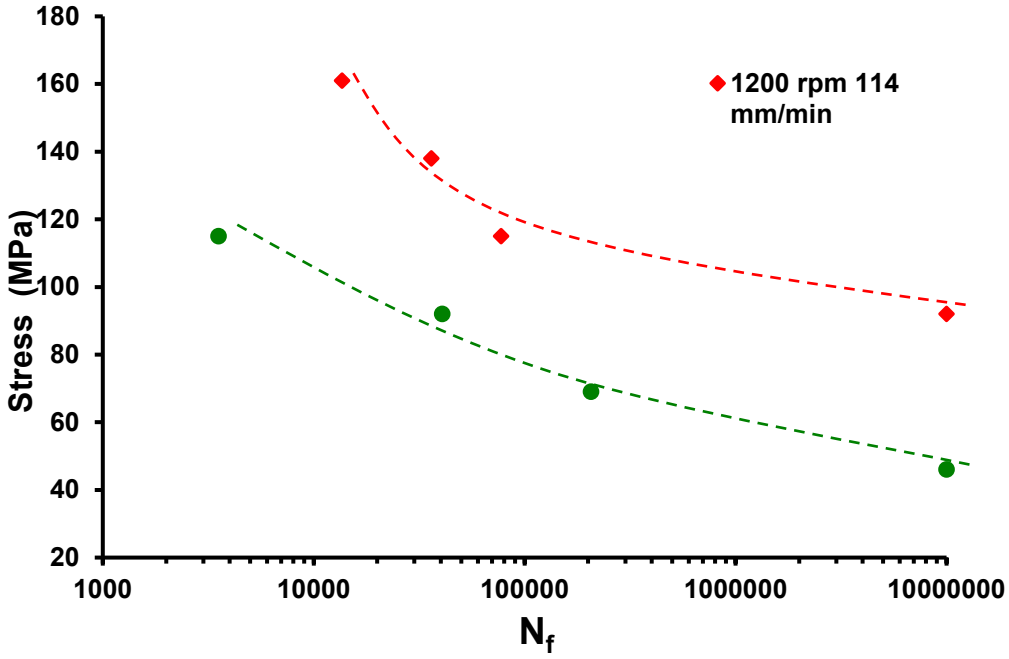

Figure 4-19: Stress versus fatigue cycles at a constant RPM and two different travel speeds.

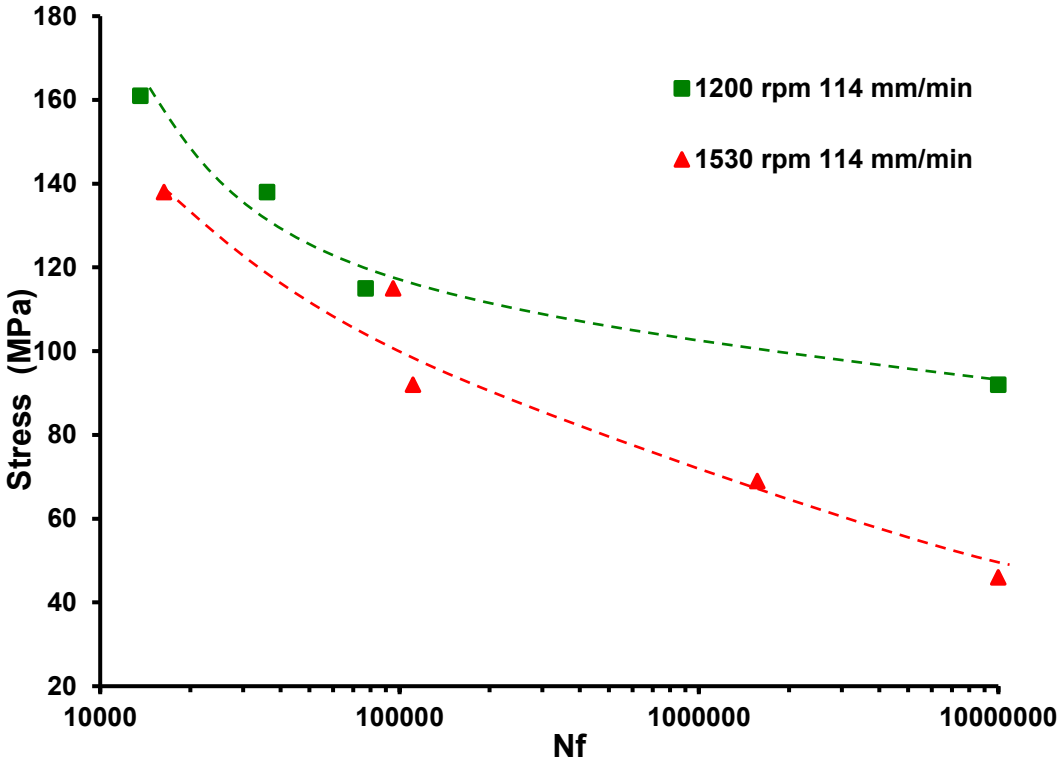

Figure 4-20: Stress versus fatigue cycles at a constant travel speed and two different rotational speeds

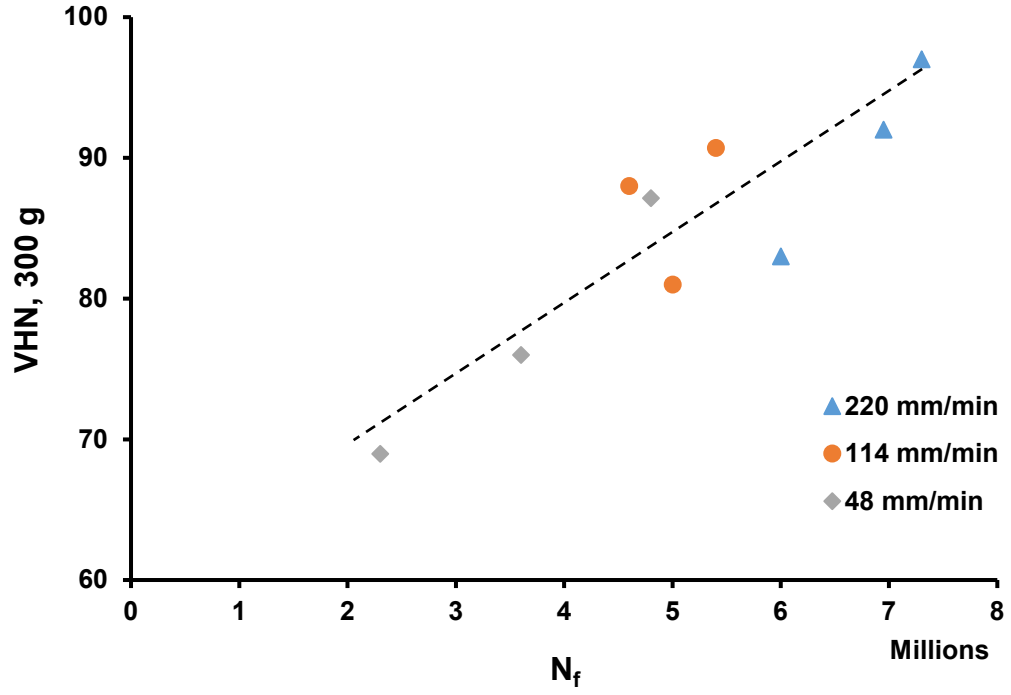

Figure 4-21: Correlations between Nf and the SZ hardness values at different travel speeds. For each traverse speed, there is a 635, 1200, and 1530 rotational speed; the hardness values were an average of 5 indents from the SZ.

Figure 4-22 shows the difference between fatigue response of the thinner and the thicker sheets for a representative FSW test at 1500 rpm and 220 mm/min. Two main reasons for better fatigue life of thinner sheets versus thicker sheets are (*i*) a larger volume of material is stressed which means more imperfections and initial defects (*i.e.* micro-cracks, porosities, lack of fusion, etc.) are involved; (*ii*) the residual stress in a thicker joint is higher than thinner one, which influences the fatigue life of welded structures.

Having said this, the corresponding thickness corrections for fatigue life can be written as [135]:

$$N = N_B \left(\frac{t_B}{t} \right)^{0.75} \qquad \text{Eq. 4-7}$$

where N_B refers to fatigue life for a reference plate thickness t_B.

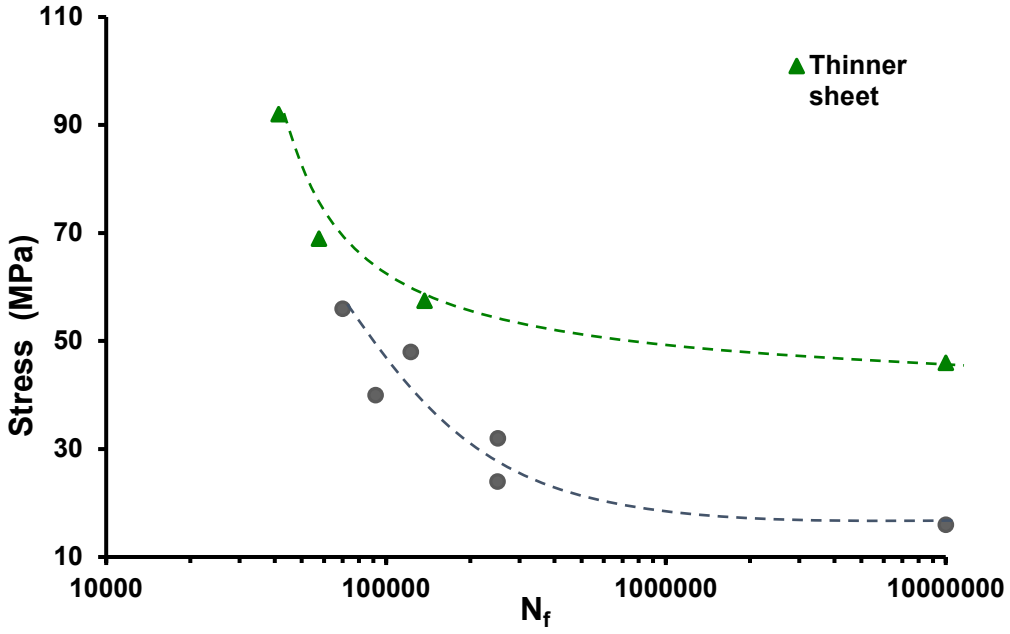

Figure 4-22: The effect of sheet thickness on the fatigue response of FSWed AM60 (1500 rpm and 220 mm/min).

4.1.4 SEM Fracture Surface Analysis

The fracture surfaces were analyzed by the SEM to reveal the mechanisms and the type of fracture of the samples that undergo fatigue testing. During fatigue testing, cracks initiate from the imperfections (either surface or internal) then grow continuously until the point where the remaining material is overstressed. The next step is unstable crack growth and final fracture (failure). Figure 4-23 shows a crack initiation point for the FSWed samples employing 1530 rpm rotational and 48 mm/min travel speed.

The dominant feature on the fracture surface is the extensive presence of ductile dimple markings (Fig. 4-24) which are indicatives of void initiation, growth, and coalescence (possibly from $Al_{12}Mg_{17}$ phase particles). Some porosities are observed on the fracture surface which act as pre-existing voids of significant size and facilitate the coalescence of other growing damages. In this case, voids, generated by the FSW process, and casting porosities both contribute to the final fracture. Having said this, the material exhibits a ductile behavior. The stirring action of the FSW tool produces fine grains in the SZ leading to ductile fracture compared with brittle fracture of the non-processed (as-cast) materials where casting voids can directly contribute to the brittle behavior of the material. As depicted with arrows on the fracture surfaces, isolated small zones of striation-like features (Fig. 4-25) and the presence of local ductility in the zones surrounding the small voids were observed. In the *hcp* materials, like AM60 Mg alloy, the formation of fatigue striations has been linked to the twinning and de-twinning during loading and unloading [136]. The striations are unique features to fatigue testing which are microscopic in nature and only visible under high magnification. There are regions of brittle fracture (Fig. 4-26) that

transitioned to ductile regions interspersed with dimples and localized area of plastic deformation of the fracture surface.

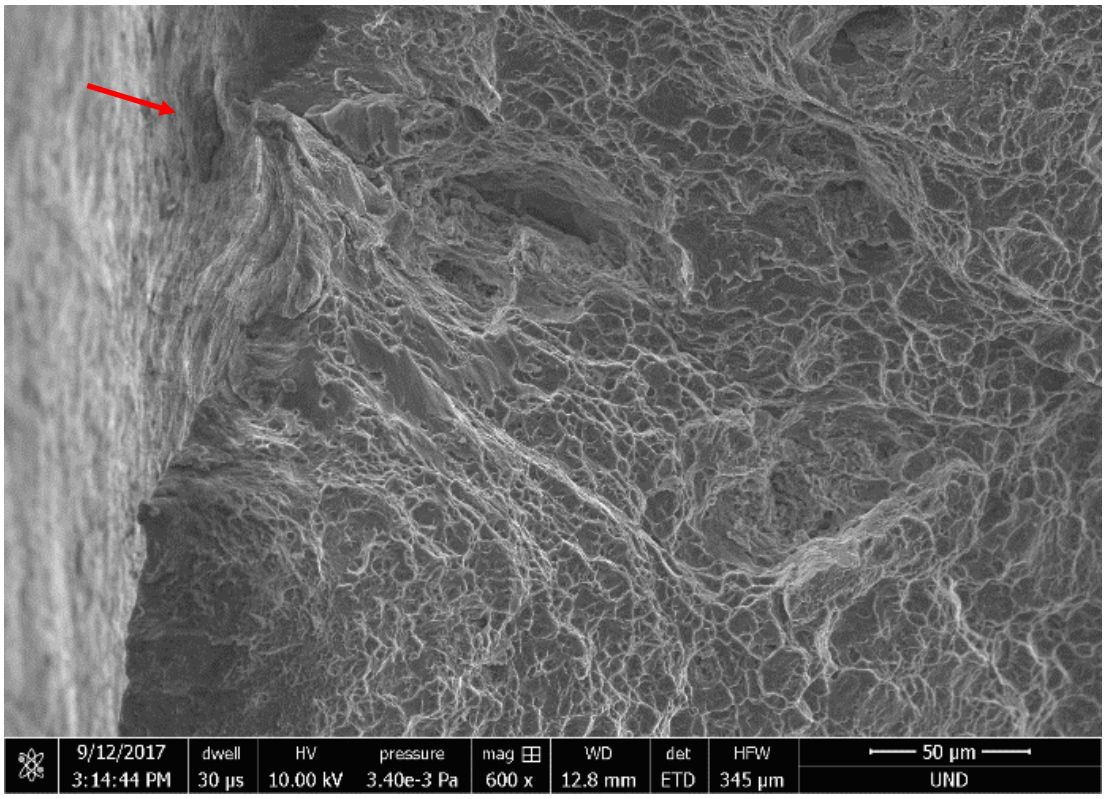

Figure 4-23: Red arrow shows a fatigue crack initiation point (1530 rpm rotational and 48 mm/min travel speed).

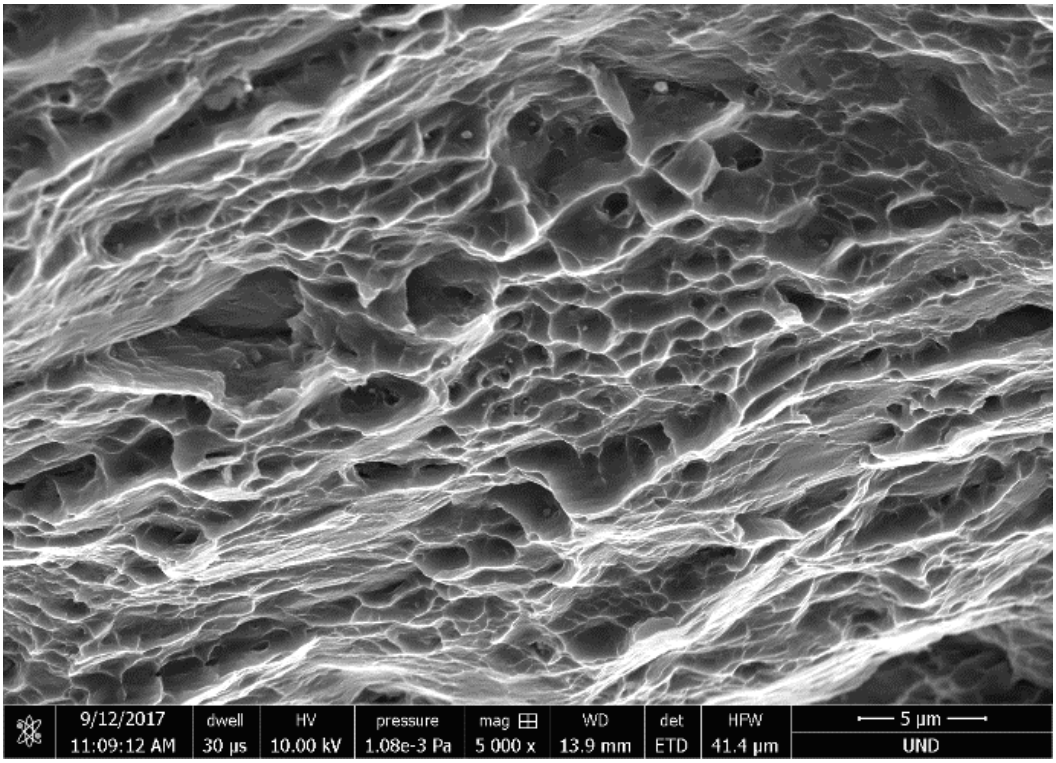

Figure 4-24: SEM fractograph showing considerable ductile-dimple structure in the eutectic in the fracture surface (1530 RPM, and 220 mm/min).

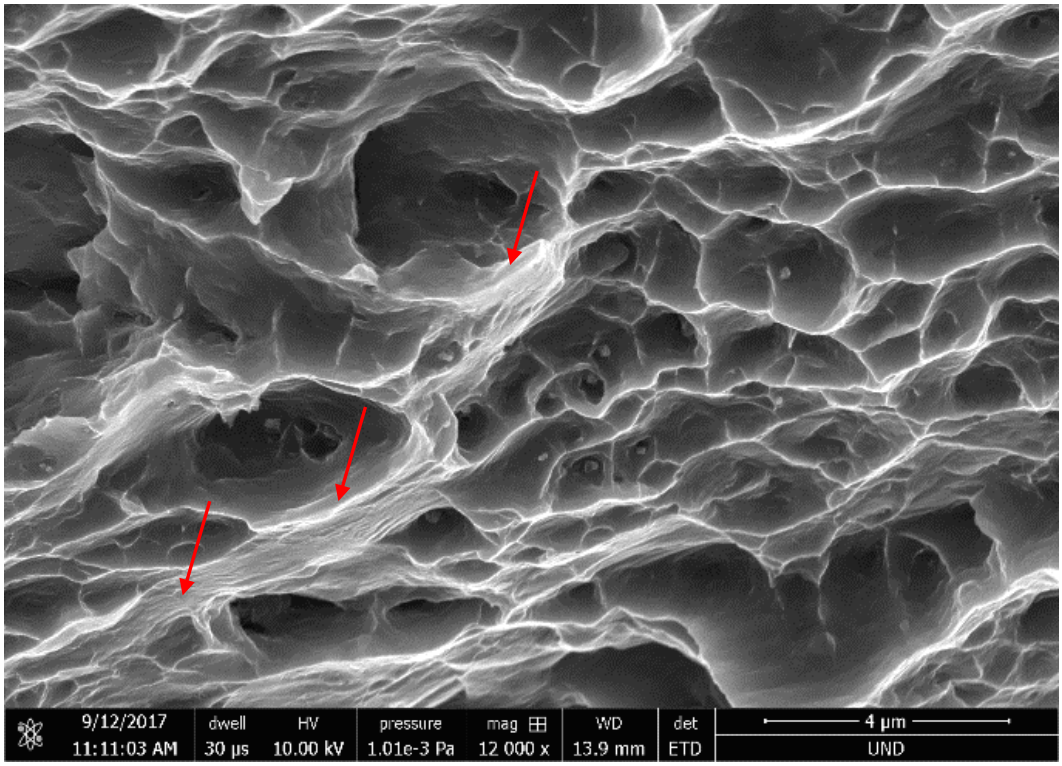

Figure 4-25: Striation-like features on the fracture surface (1530 RPM, and 220 mm/min).

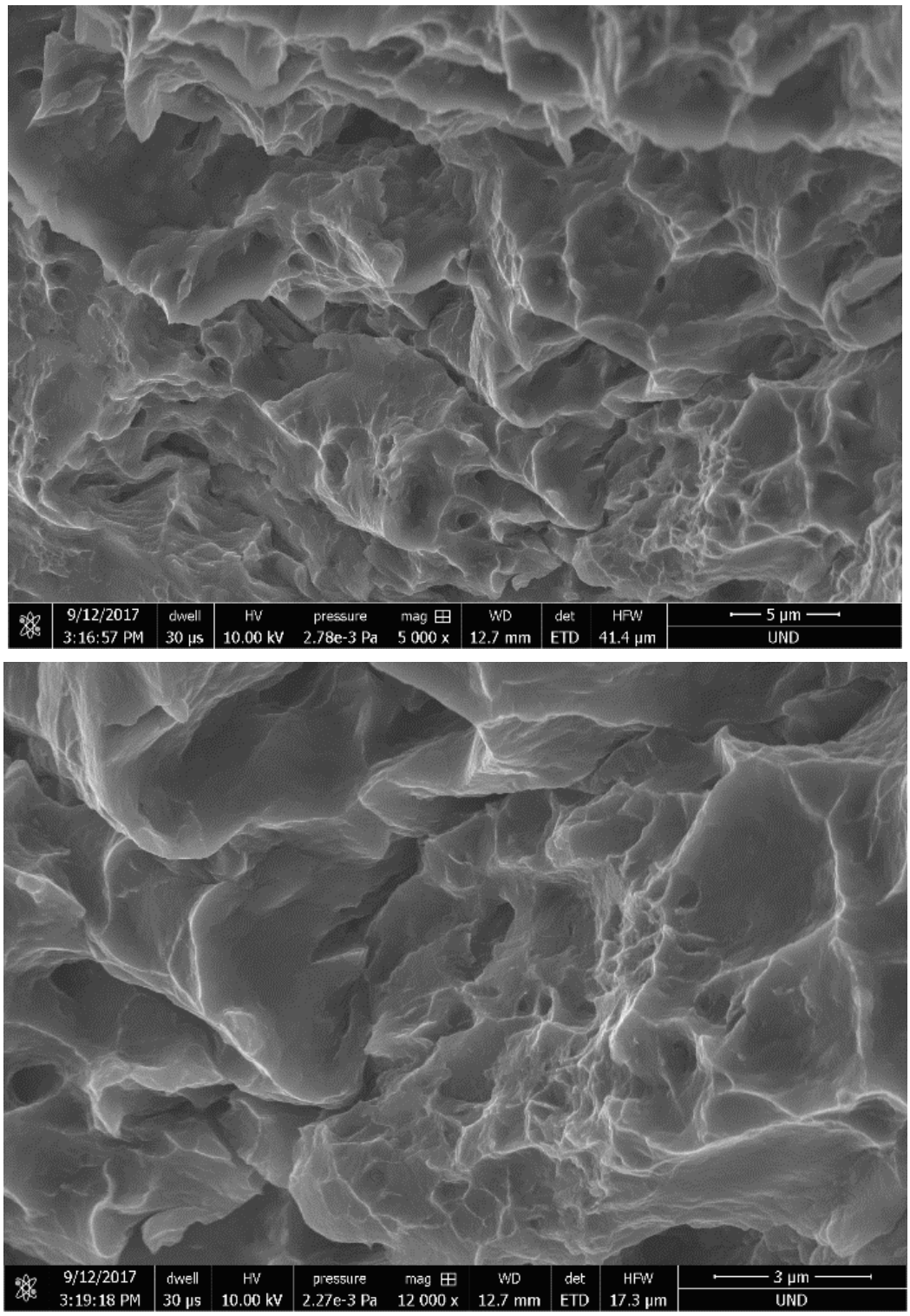

Figure 4-26: Features on the fracture surface confirming a mixture of brittle/ductile fracture (1530 RPM, and 48 mm/min).

4.2 Al-10%Si Al Alloy

4.2.1 Microstructure Analysis

In this section the microstructure of the of the non-processed base aluminum Al-10%Si cast alloy is compared against the processed microstructure to assess the microstructural evolutions. Figure 4-27 shows the SEM micrograph of the as-received die cast Al-10% Si microstructure used in this study. The Al-10%Si alloy is a hypoeutectic mixture which possesses a homogeneous microstructure that includes a primary dendrite phase, eutectic mixture along with some porosity. The microstructure consists of α-Al dendrites and coarse Si particles concentrated in Al-Si eutectic regions. This type of Si particle segregation in the inter-dendritic regions is the effect of the natural solidification sequence of this alloy, the sizes and morphologies vary depending on melt chemistry and cooling rate. This is the expected microstructure for the alloy at ambient temperature based on the Al-Si binary phase diagram provided in figure 4-28.

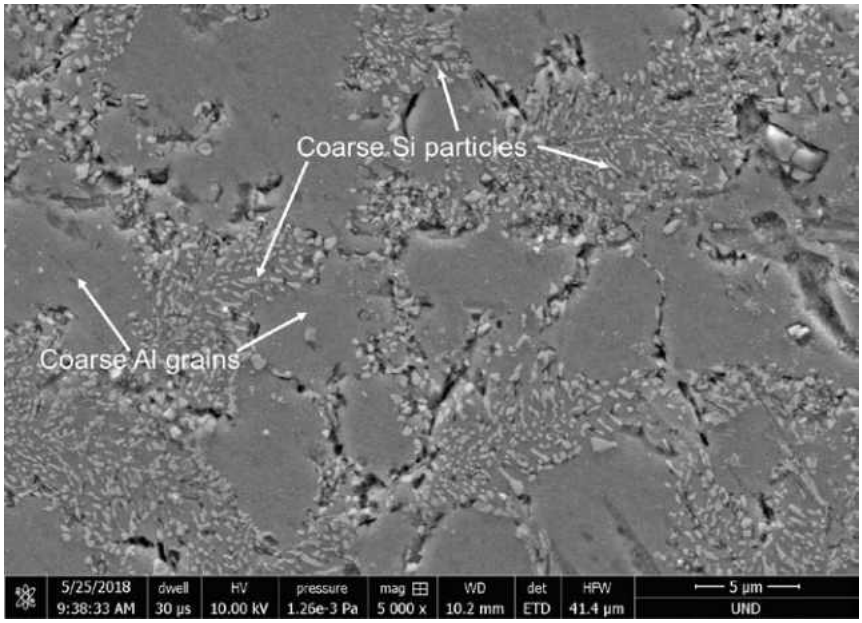

Figure 4-27: SEM of the microstructure of the as received Al-10%Si alloy (1200 RPM, 114 mm/min)

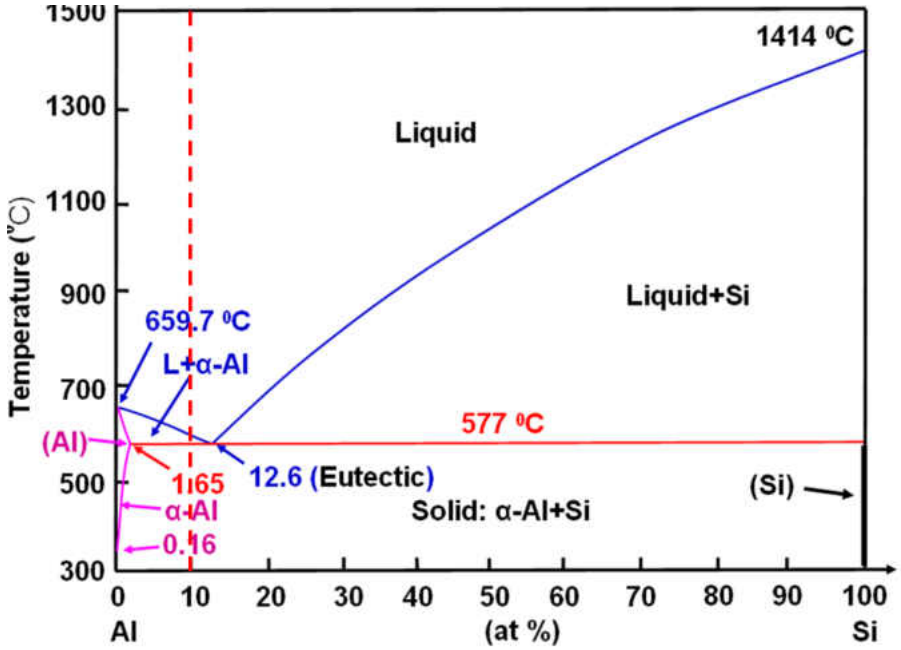

Figure 4-28: Aluminum-silicon phase diagram [54]. The dashed line, schematically, shows the position of the Al-10%Si alloy

Upon running the FSW process, the microstructure of the Al-Si alloy changes drastically due to the severe plastic deformation caused by the rotating tool. The welded structure of the Al-Si alloy is like that of the AM60 alloy with the presence of a clear stirred zone (SZ) with fine equiaxial grains and thermomechanically affected zone (TMAZ) with elongated and tilted grains were found. Figure 4-29 provides the microstructures of the base metal (BM), the TMAZ and the SZ for the purpose of comparison. Under an optical microscope, the lighter areas are the α-Al while Si particles are dark. The BM is composed of course Si particles which are non-uniformly distributed in the eutectic matrix. As expected the SZ of the FSW joints consistently showed a fine recrystallized, equiaxed grain structure, with β-Mg_2Si precipitates which is caused by dynamic recrystallization. It is expected that the size of the α-Al grains in the SZ as compared with the base metal are much finer [21]. As with AM60, the intense plastic deformation imposed by the FSW tool occur in a short period of time that does not allow for the recrystallized grains to grow with in the SZ and this leads

to the significant grain refinement. The temperature of the SZ is dependent on the tool traverse and rotational speeds and can be calculated using equation 4-1.

For Al-10%Si the constants are unknown. Table 4-7 shows the ratio between the SZ and melting temperature as a function of the constants K and α based on Eq. 4-1 (T_m= 660 ºC [52]). The recrystallization temperature of the Al-Si alloys series is ~400 ºC [137]. Therefore, in almost all combinations of FSW parameters in the present study, dynamic recrystallization does happen.

Table 4-7: The FSW parameters, rotational and transverse speeds, and the SZ temperature according to Eq. 4-1

Rotational speed (rpm)	**Traverse speed (mm/min)**	$\frac{T_{SZ}}{T_m}$
635	114	$K(0.35)^{\alpha}$
635	420	$K(0.10)^{\alpha}$
1200	114	$K(1.26)^{\alpha}$
1200	220	$K(0.65)^{\alpha}$
1530	114	$K(2.05)^{\alpha}$
1530	420	$K(0.56)^{\alpha}$

The foremost factor in determining the recrystallized grain size is the peak temperature of the FSW cycle. This means that the recrystallized grain size in the FSW Al-Si alloy increases with increasing tool rotational rate or the ratio of the tool rotational speed/travel speed. This is expected because the heat input and peak temperature decrease with increase in traverse speed or decrease in rotational rate. At these lower temperatures there is less time for the grain growth to occur which leads to the smaller grain sizes. There is an optimum combination of FSW parameters for generating the finest grain size in the Al-Si alloy.

In the SZ, as observed, Si fibers are broken into smaller pieces within the SZ and uniformly distributed within the α-Al matrix. The SZ forms a rotational shear material (RSM) region [8]. In the RMS region the Si particles are uniformly distributed throughout the α-Al matrix. Figure 4-29c shows these smaller, evenly distributed particles in the SZ. Outside of the RMS region the alloy is still deformed but to a much lower extent causing the concentration of the Si particles in the interdendritic regions to remain, this keeps the microstructure highly segregated. The broken Si particles are found to be nearly spherical in shape which is a result of the intense stirring effect of the rotating tool. Figure 4-30 is the SEM micrograph showing the as-cast Si fibers within the eutectic matrix and Figure 4-31 shows the post-FSW spherical particles. These spherical particles are created through spheroidization (Fig. 2-8). Spheroidization helps to improve the alloy's ductility and fatigue strength [50].

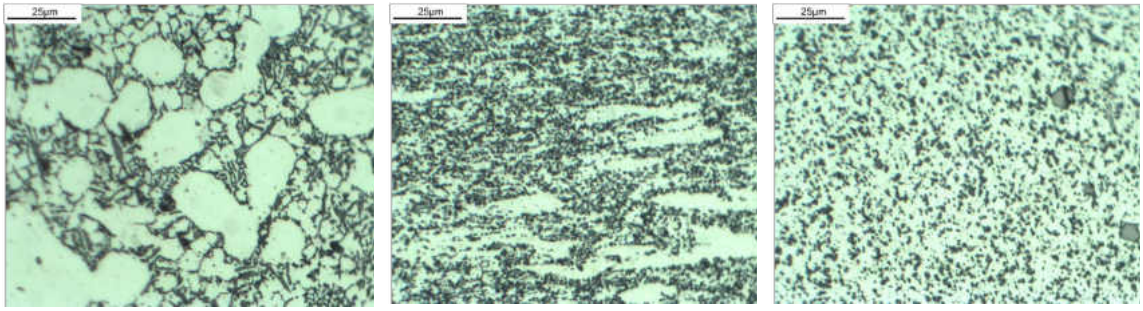

a) b) c)

Figure 4-29: The optical micrographs of the microstructure of as-received a) Al-10%Si alloy, b) TMAZ and c) SZ (1530 RPM, 420 mm/min)

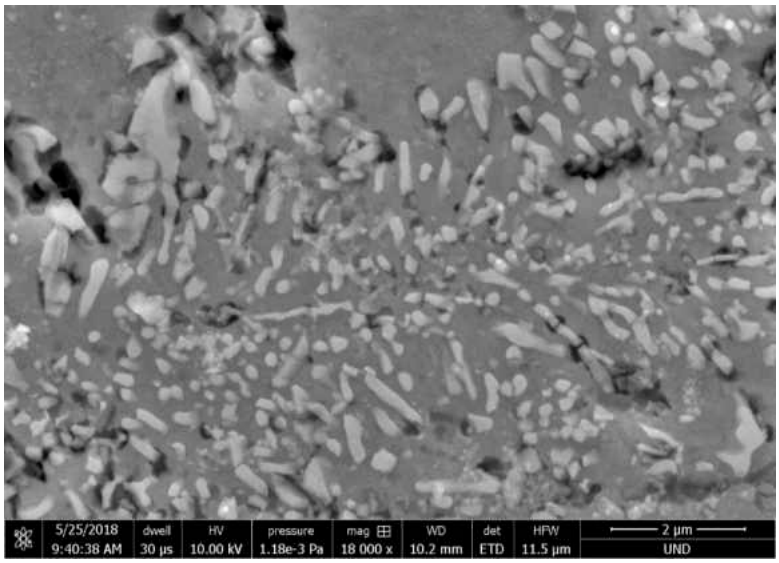

Figure 4-30: SEM of the microstructure of the as-cast Si fibers (1200 RPM, 114 mm/min)

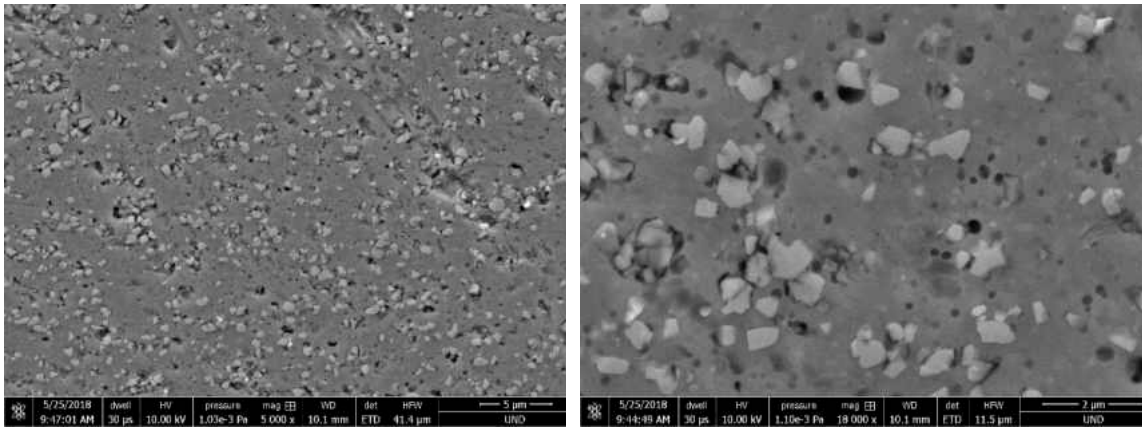

a) b)

Figure 4-31: SEM of the microstructure of FSW SZ spherical particles (1200 RPM, 114 mm/min)

The size and distribution of the Si particles are hardly affected by the welding parameters. This is evident in Figure 4-32 which shows a comparison of the SZ of different parameters. As well, the fine, spherical Si particles are expected to reduce the crack sensitive zone [57]. The size of the α-Al grains in the SZ as compared with the base metal is much finer. As with AM60, the intense plastic deformation imposed by the FSW tool occur in a short period of time that does not allow for the recrystallized grains to grow with in the SZ and this leads to the significant grain refinement.

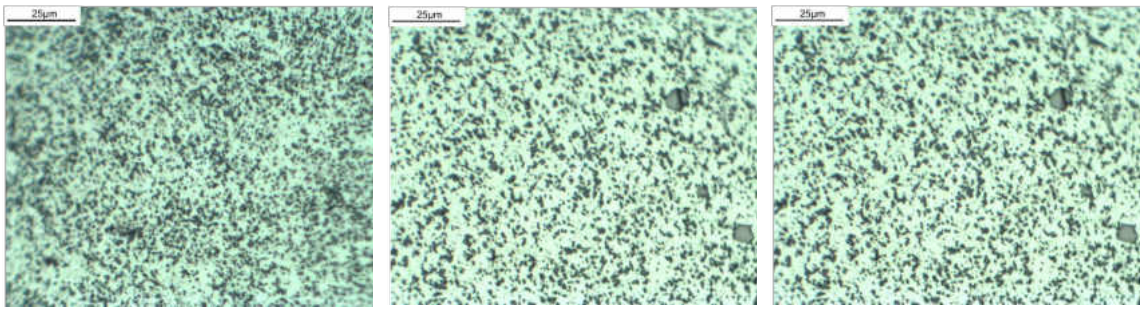

Figure 4-32: The optical micrographs of the SZ of FSW a) 635 RPM, 420 mm/min, b) 1530 RPM, 420 mm/min and c) 1530 RPM, 114 mm/min

The TMAZ (Fig 4-29b) is highly susceptible to plastic deformation but it does not go through dynamic recrystallization because of deficient strain and temperature [21]. The TMAZ is characterized by elongated grains which are stretched around the SZ.

The TMAZ is made up of two sub-regions. These regions are dependent on the location they are formed. One is formed by the FSW tool shoulder on the top layer of the alloy, this is known as the shoulder affected (SE) TMAZ. The other region is along the sides of the SZ, this is the pin-affected (PE) TMAZ (Fig. 4-33) [138]. Since the SE-TMAZ is formed along the shoulder diameter, which is subjected to compressive stress, the microstructure is influenced by the high temperatures generated from the frictional interaction between the alloy and the tool shoulder and not the pin stirring [138] (Fig. 4-34).

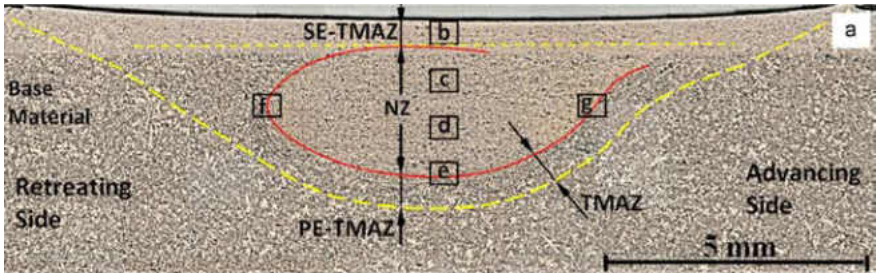

Figure 4-33: Cross-section of FSW sample perpendicular to the advancing direction showing the different TMAZ subsections [138]

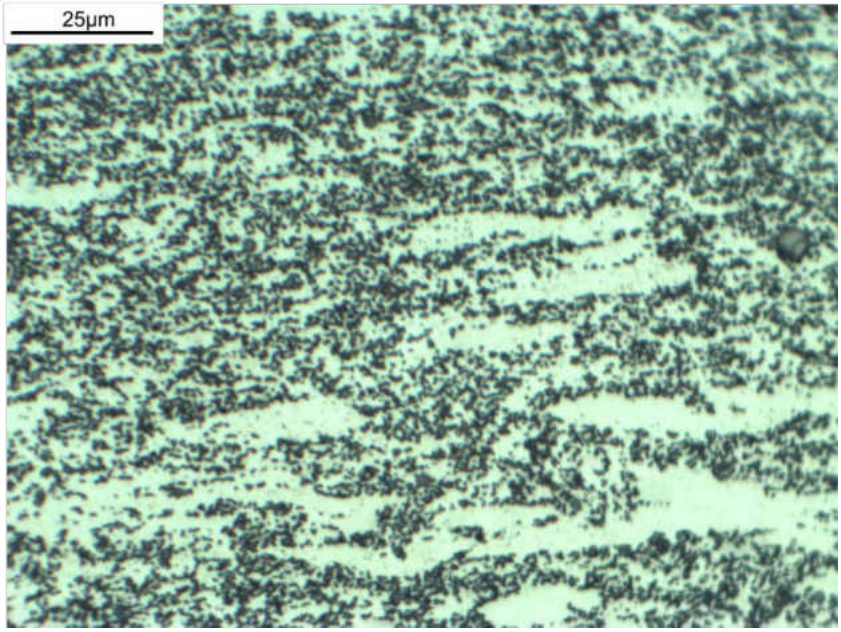

Figure 4-34: SE-TMAZ region (1530 RPM, 420 mm/min)

The PE-TMAZ is much more effected from the stirring on the pin as compared with the SE-TMAZ. There is a distinct transition from the SZ to the PE-TMAZ (fig. 4-35). The eutectic Si particles are aligned in the same direction around the SZ.

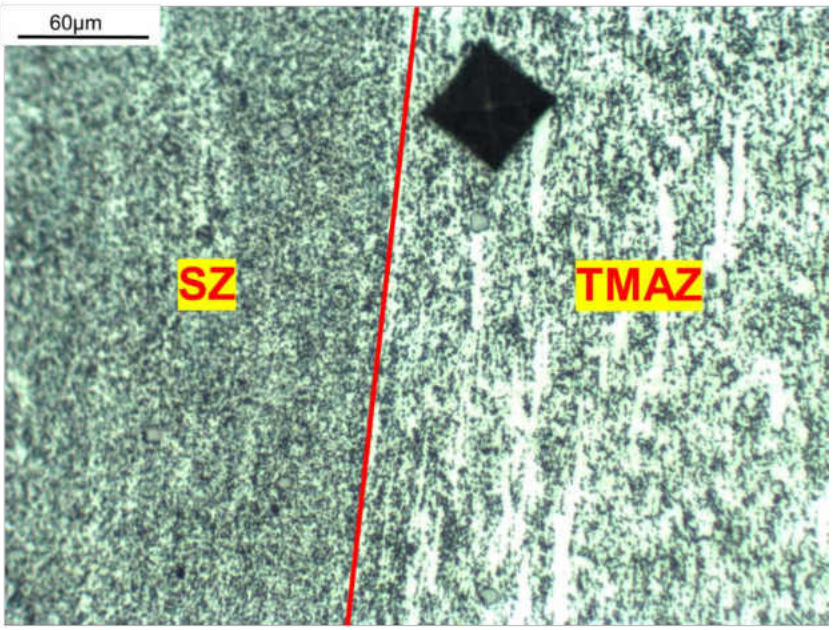

Figure 4-35: Transition region in the PE-TMAZ (635 RPM, 420 mm/min)

4.2.2 Hardness Test Results

It is clear that there is significant softening throughout the weld zone as compared to the base Al-10%Si base metal. It is observed that there is a wide range of hardness in the BM. The BM is made up of a hypoeutectic microstructure of Al-Si (Fig 4-28). The Al solution is softer than the Si fibers and has a larger volume fraction. If the hardness was taken in the primary α-Al phase as compared with the eutectic Al-Si solution it shows a lower hardness [139]. This indicated that the hardness of the Al-Si alloy BM is dependent on where the indenter sits in the alloy. The SZ shows more uniform hardness values because of the dispersed, spherical Si particles.

Aluminum alloys can be classified into heat-treatable (precipitation-hardenable) alloys and those that are non-heat-treatable alloys. Previous studies on precipitation-hardened aluminum alloys show that FSW creates a softened region around the weld center [21]. This softening happens in the thermal cycle of FSW when the strengthening precipitates (Si) are coarsened [21]. The vigorous stirring of the Al-Si alloys during FSW causes the eutectic Si fibers to convert to spherical particles. This is done in a process known as spheroidization. Spheroidization occurs when the temperature of the alloy is held below the eutectic temperature [140] which is provided through frictional heat during the FSW process. The Si content assumes a spheroidal shape and then is dispersed evenly through the alloy by sever plastic deformation during the FSW [141] (Fig 4-31).

Figure 4-36 shows the distribution of hardness across the joint at a constant rotation speed (635 RPM) and different feed rates (for the sake of comparison, different zones have been identified). The weld center (or stirred zone) is showing a softer region where Si spheroidization happens. Spheroidization phenomenon results in the reduced hardness

with-in the SZ because the sharp edges of strengthening Si precipitates are eliminated. This reduction in hardness leads to an increase in the ductility of the Al-Si alloy in the SZ. That is, the spherical Si particles allow the alloy to deform plastically without cracking [142], which in turn increases the machinability [140]. By moving away from the SZ, hardness increases. The peak hardness is seen in the base metal which is not affected by the mechanical action and/or thermal gradient of the welding operation. The hardness values in the TMAZ is lower than the ones in the HAZ; this is mainly attributed to the TMAZ being exposed to more of a thermal cycle then the HAZ and thus more precipitation distribution in the TMAZ is seen than the HAZ [21]. There is not that much of difference in the hardness values of the SZ at different travel speeds when the rotational speed is held constant. It is worth noting that each provided hardness number is an average of three hardness values, however, to make the actual hardness values visible and not to make the hardness graphs busy (and even unreadable) the error bars have not been provided. Figure 4-37 shows the hardness measurements at a constant rotational speed of 1200 RPM and different traverse speeds (114 mm/min and 420 mm/min). It is clear from the hardness values that the highest hardness values in the stirred zone are less than those of the other zones. It can be noted that the softest measurement is not seen in the center of the weld but rather 2.8 mm on either size of the weld center line. In both figure 4-37 and Figure 4-38, we see the lower travel speed contributes to the lowest hardness values which is attributed the higher heat input created in lower travelling speed. At a constant rotational speed, with decreasing the travel speed, the frictional heat is increased. This can account for more of the precipitates to become dissolute which in turn reduces the hardness of the metal.

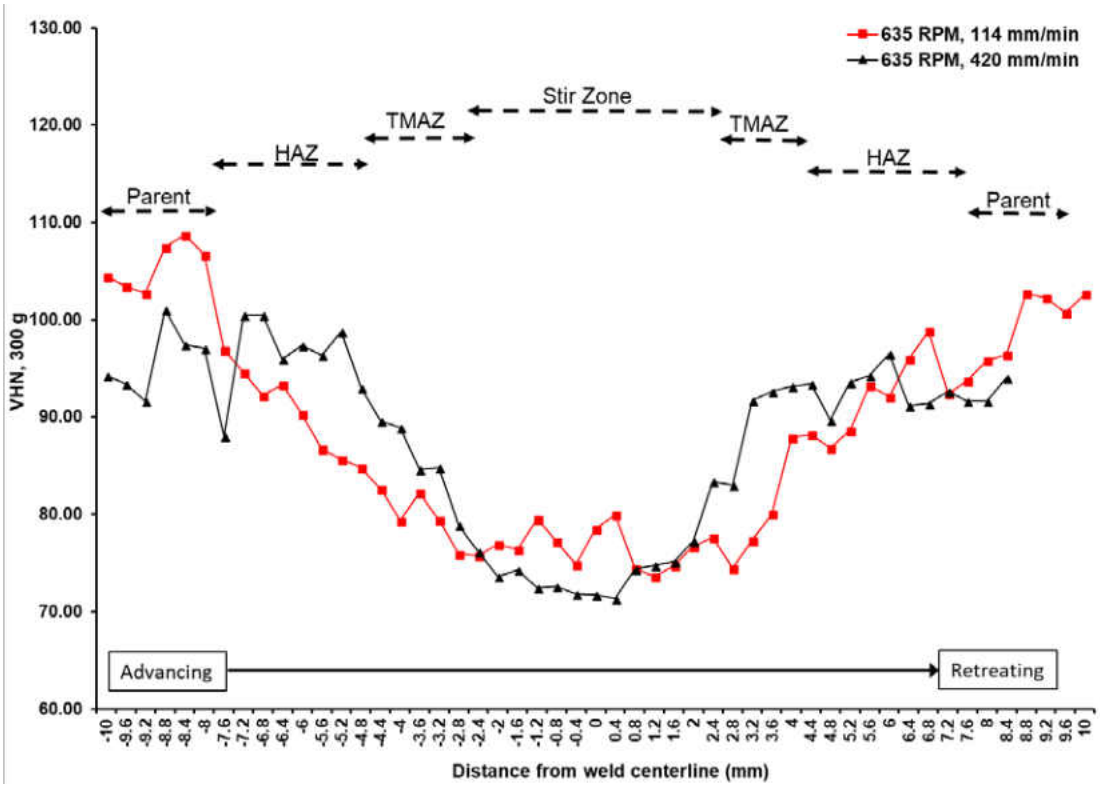

Figure 4-36: Hardness distribution across the weld at a constant rotation speed of 635 RPM and different travel speeds. Various zones have been identified in the image

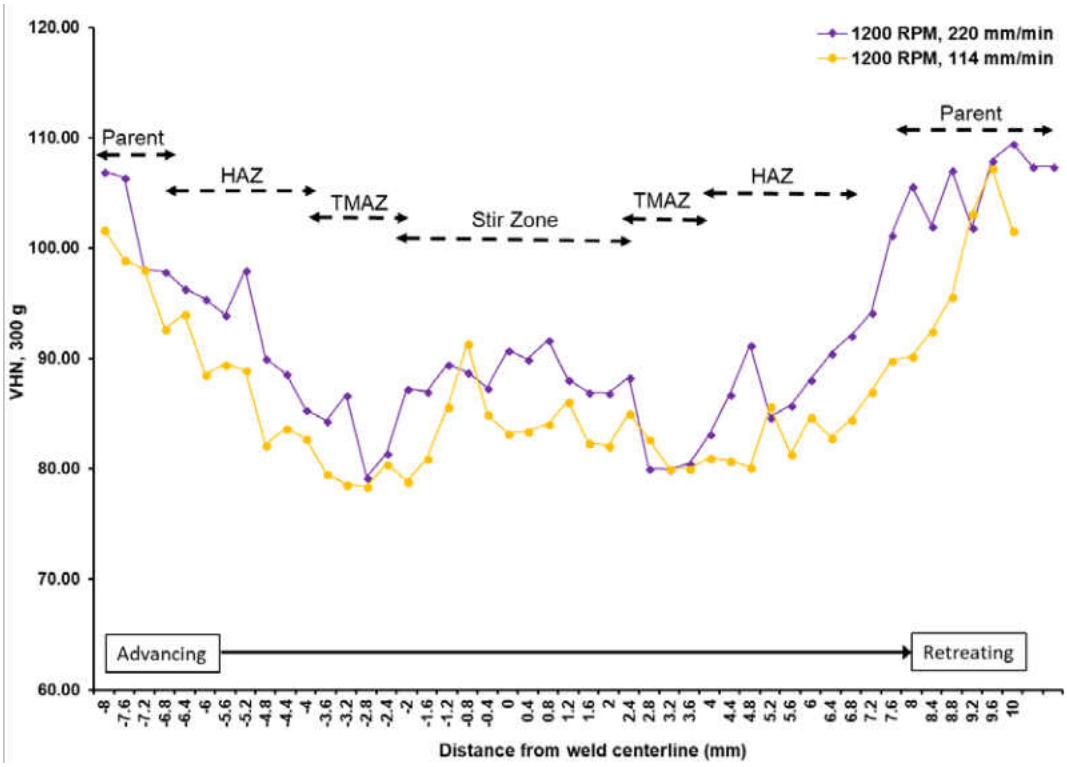

Figure 4-37: Hardness distribution across the weld at a constant rotation speed of 1200 RPM and different travel speeds. Various zones have been identified in the image

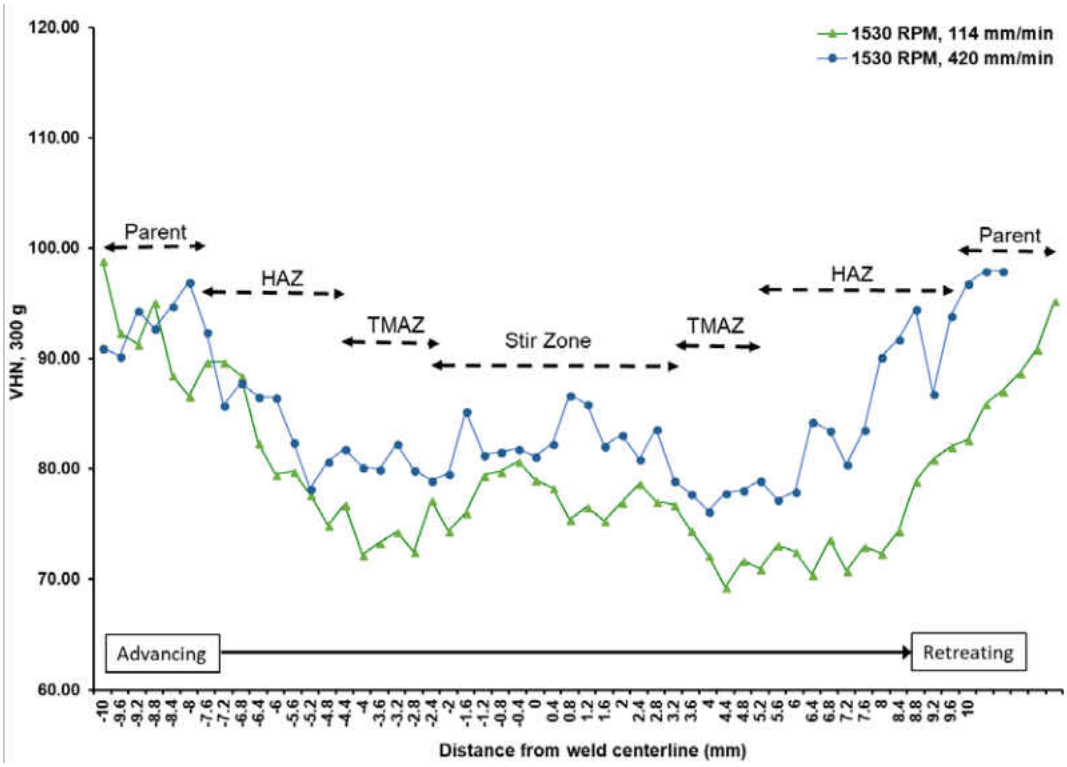

Figure 4-38: Hardness distribution across the weld at a constant rotation speed of 1530 RPM and different travel speeds. Various zones have been identified in the image

Figures 4-39 and 4-40 show the hardness variations at a constant traverse speed and different tool rotational speeds of 635 and 1530 rpm. Here we see the same results as when the rotational speeds were held constant. The softer material is seen in the center of the weld, caused by the Si particle spheroidization. At the lower travel speed (114 mm/min) both 635 and 1530 RPM show similar hardness. At a higher travel speed of 420 mm/min, 635 RPM has a softer hardness with in the weld zone.

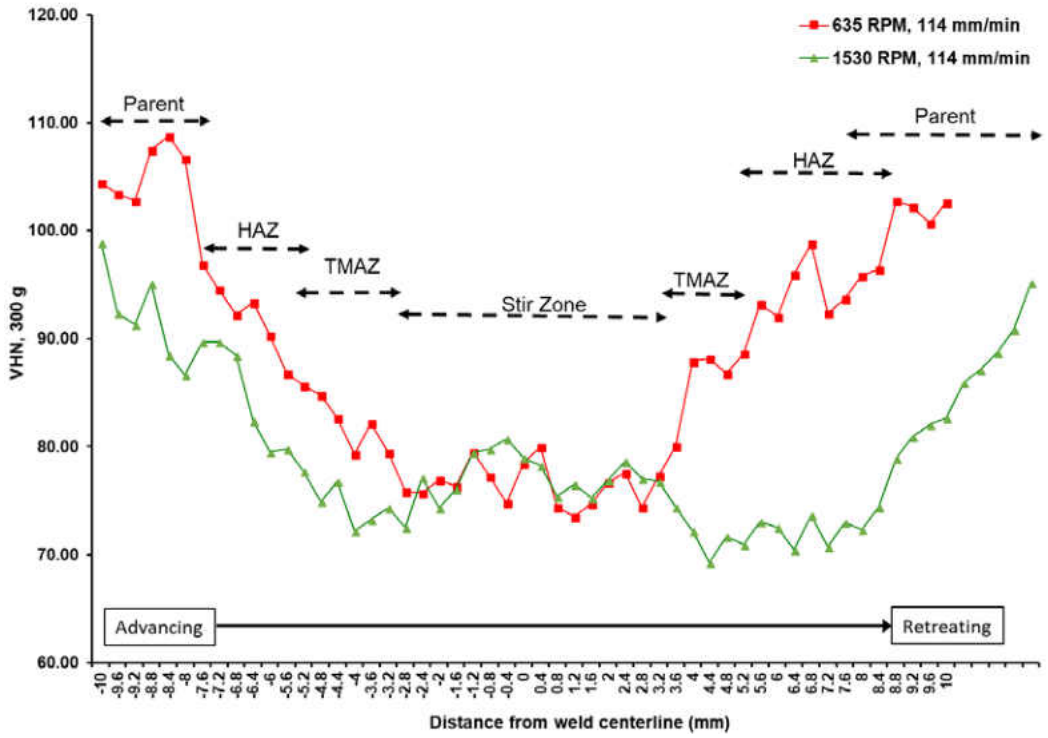

Figure 4-39: Hardness distribution across the weld at a constant travel speed of 114 mm/min and different rotational speeds. Various zones have been identified in the image

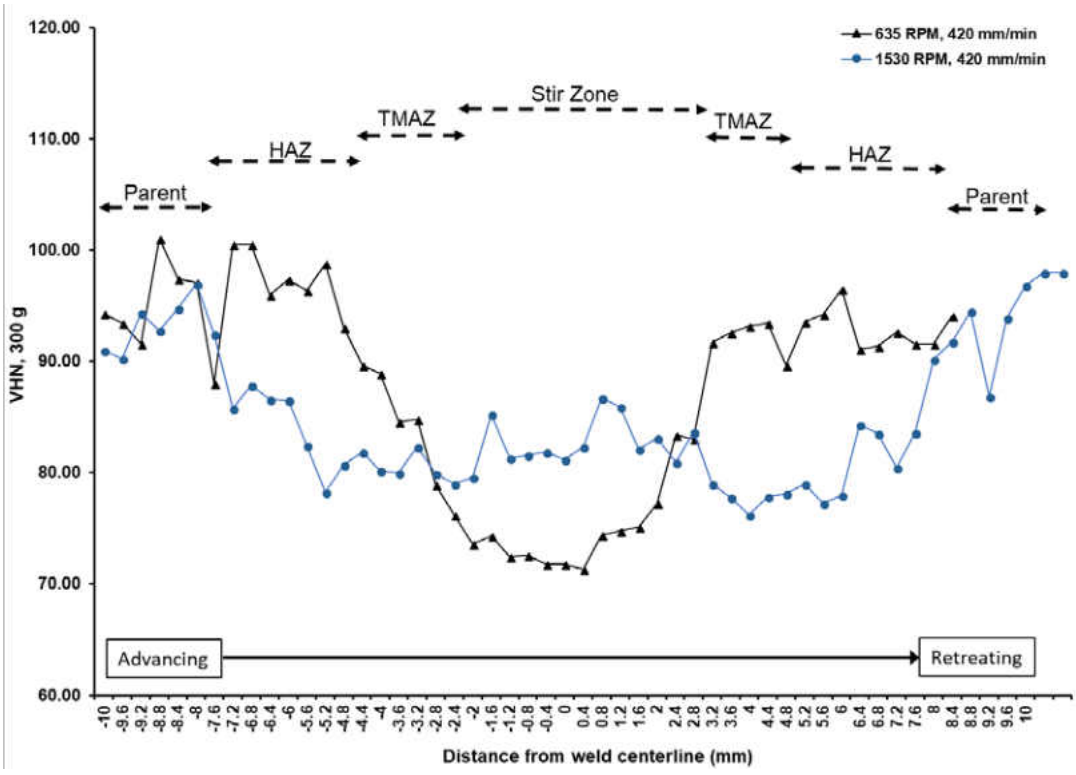

Figure 4-40: Hardness distribution across the weld at a constant rotation speed of travel speed of 420 mm/min and different travel speeds. Various zones have been identified in the image

4.2.3 Fatigue Response

Figure 4-41 through 4-43 shows the maximum stress plotted against the number of cycles to failure for constant RPMs of 635, 1200, and 1530, respectively and two different rotational speeds of 114 and 420 mm/min or 114 and 220 mm/min. When the rotational speed is held constant, the slower traverse speed (114 mm/min) has a better fatigue response that that of the faster travel speeds (220 mm/min or 420 mm/min). By lowering the travers speed to 114 mm/min the fatigue life was improved between 2 and 2.5 times. At 635 RPM and 420 mm/min there was no failure until 10^7 cycles when tested at 46 MPa, whereas at the same rotational speed and 114 mm/min this was improved to 115 MPa (Fig. 4-41). At 1200 RPM and 220 mm/min there was no failure until 10^7 cycles when tested at 23 MPa, whereas at the same rotational speed and 114 mm/min this was improved to 46 MPa (Fig. 4-42). At 1530 RPM and 420 mm/min there was no failure until 10^7 cycles when tested at 46 MPa, whereas at the same rotational speed and 114 mm/min travelling speed this was improved to 92 MPa (Fig. 4-43). At a constant rotational speed, with increase in the tool travel speed the peak temperature in the SZ and the heat input decrease (see Table 4-7). We saw from the hardness tests that the hardness with in the SZ was decreased caused by the spheroidization of the Si particles. The Al-10Si alloy becomes less brittle with enhanced fatigue life.

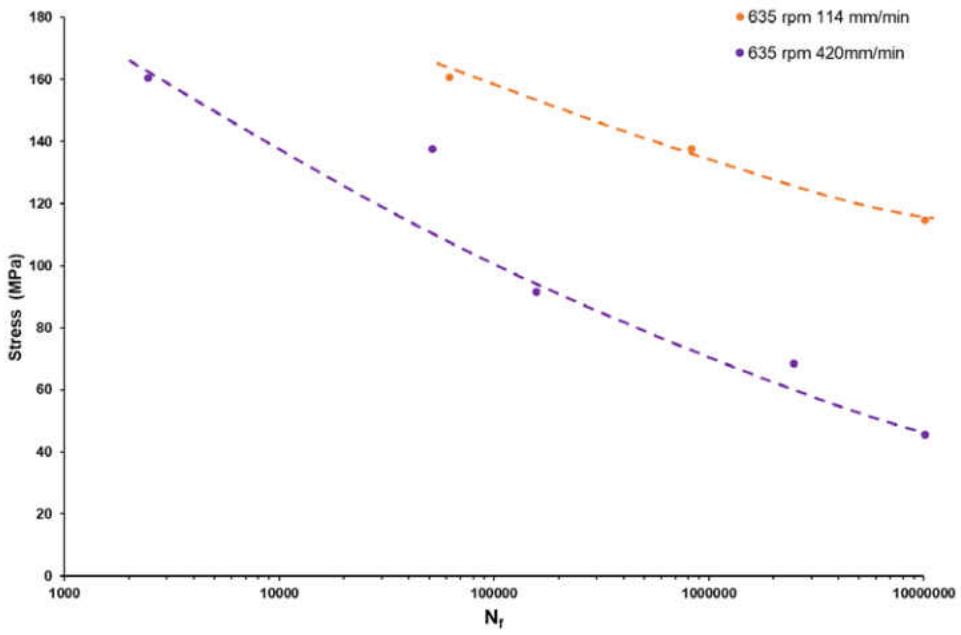

Figure 4-41: Stress versus fatigue cycles at a constant 635 RPM and two different travel speeds

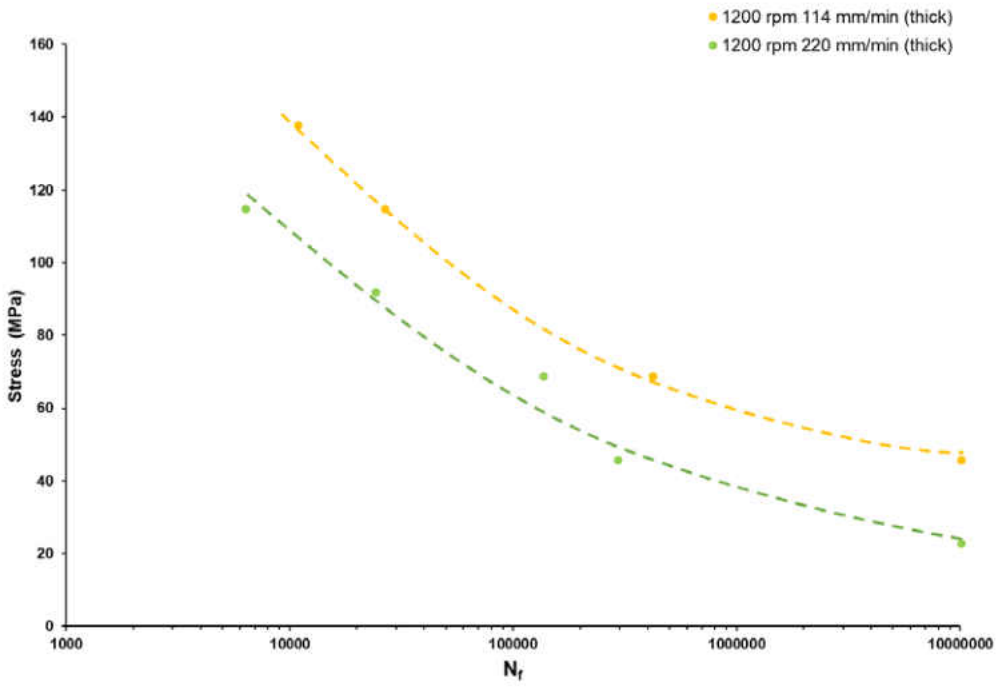

Figure 4-42: Stress versus fatigue cycles at a constant 1200 RPM and two different travel speeds.

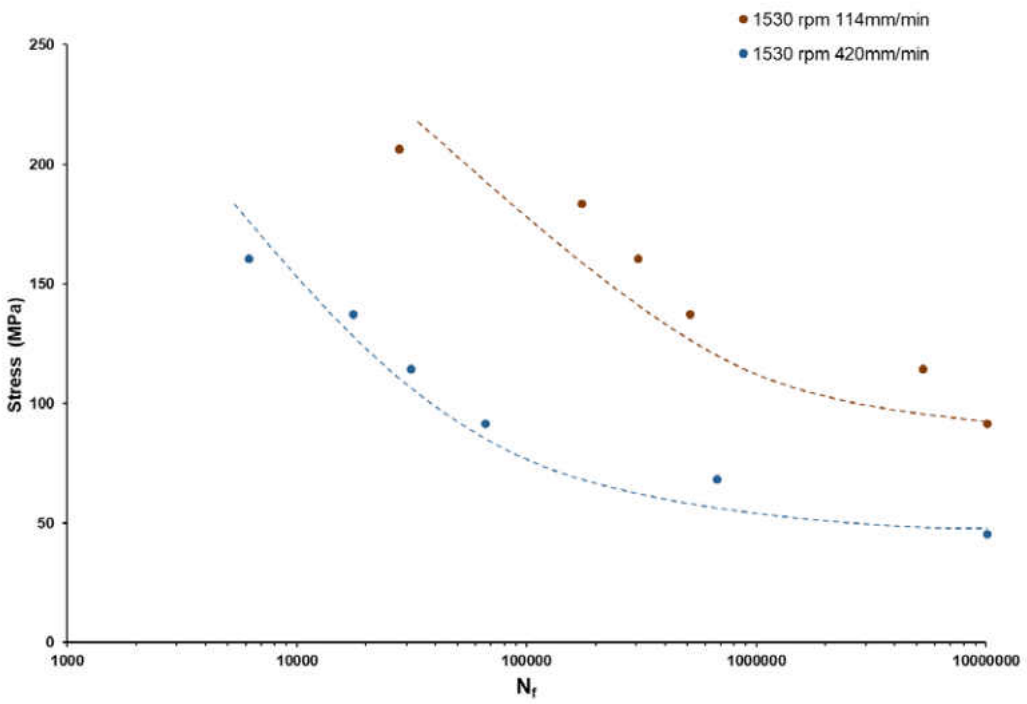

Figure 4-43: Stress versus fatigue cycles at a constant 1200 RPM and two different travel speeds

Figure 4-44 is a plot of the stress amplitude (σ_a), as a function of the number of load reversals or N_f on a log-log scale for the parameters shown in figure 4-41 through 4-43. A linear relationship between the stress amplitude and number of load reversals follows the Basquin relationship (Eq 4-8) where σ_f represents the fatigue strength coefficient and b represents the Basquin exponent [94, 143]. The data from the different parameters is clearly separated on the Basquin plot with 635 RPM and 114 mm/min having the highest response with 1200 rpm and 220 mm/min showing the poorest response. It is evident from this plot that the lower travel speed of 114 mm/min possesses a better fatigue life than that of the higher traverse speed of 420 mm/min where changing the RPM has no effect on the fatigue life. The Basquin exponent values are outlined in table 4-8.

$\sigma_a = \sigma_f (N_f)^b$ [94, 143]. Eq. 4-8

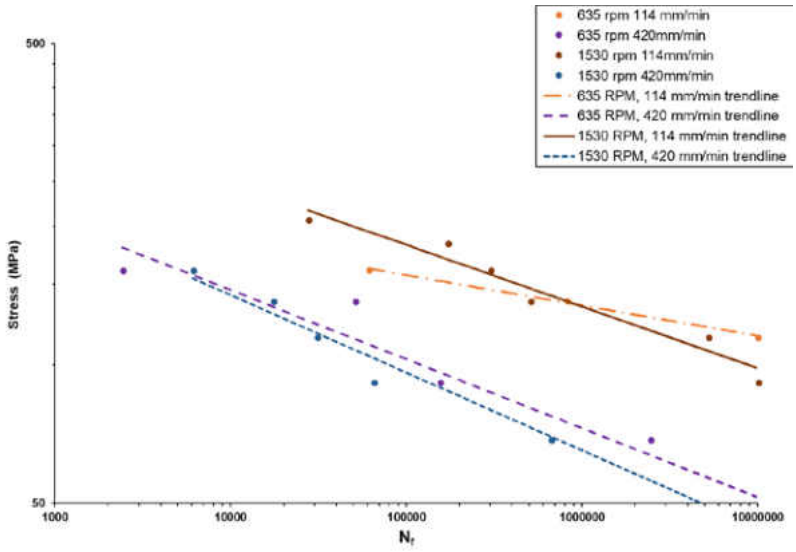

Figure 4-44: Stress amplitude vs number of cycles

Figure 4-45 and 4-48 shows the stress/N_f graphs a constant travel speed of 114 mm/min and 420 mm/min respectively and different RPMs of 635 and 1530 rpm. These results show no difference between the change in the rotational speed on the fatigue life of the Al-10%Si alloy. Considering Figs. 4-41 through 4-43, 4-45 and 4-46, one can see that the traverse speed significantly influences the fatigue strength of the welded joints; although the relationship is non-linear, the rotational speed has no influence on the fatigue strength. As mentioned before, fatigue failure in the FSWed samples was either caused by internal voids in the weld nugget or by the FSW fingerprints (*i.e.* surface marks that act as crack initiation sites). According to the hardness profiles of the FSWed samples, fatigue cracks must initiate in the SZ or TMAZ due to the low hardness values of these regions.

Table 4-8: Basquin exponent values

Parameters	Basquin Exponent	Fatigue Strength Coefficient (MPa)
635 RPM, 114 mm/min	-0.066	335
635 RPM, 420 mm/min	-0.150	580
1530 RPM, 114 mm/min	-0.134	856
1530 RPM, 420 mm/min	-0.165	672

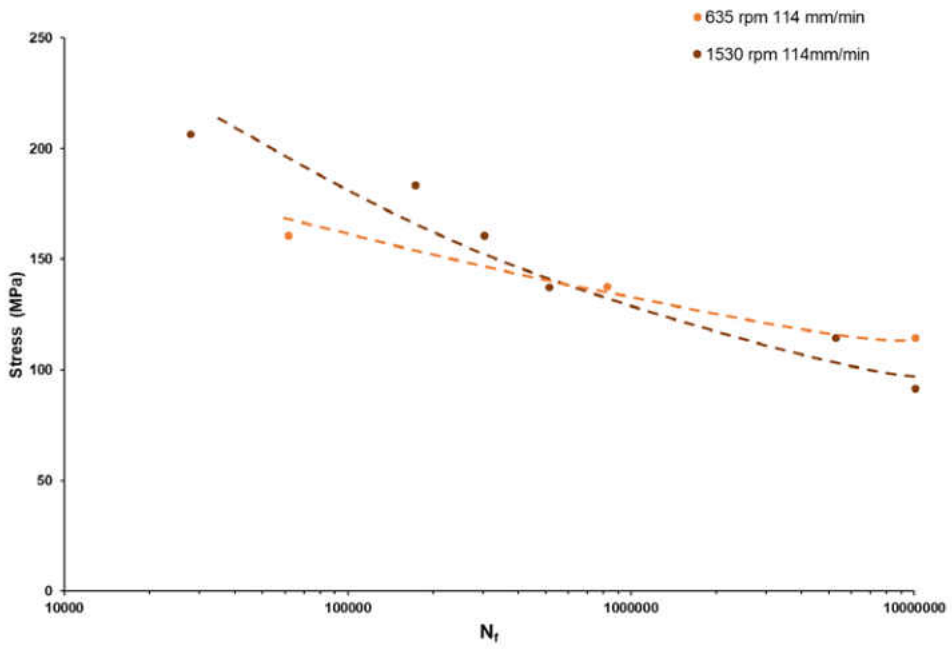

Figure 4-45: Stress versus fatigue cycles at a constant travel speed 114 mm/min and different rotational speeds

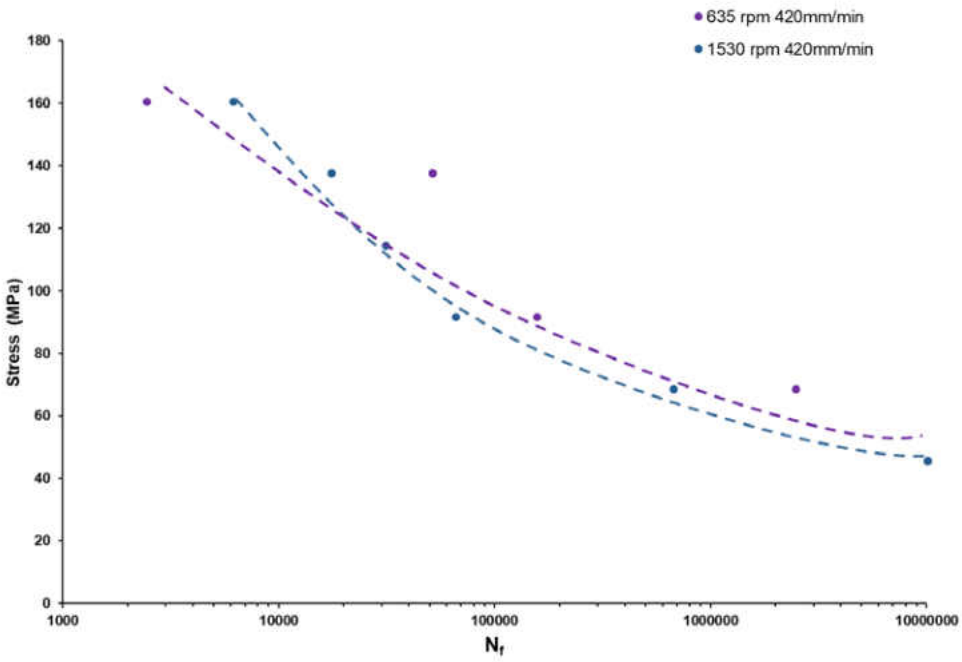

Figure 4-46: Stress versus fatigue cycles at a constant travel speed 420 mm/min and two different rotational speeds

Figure 4-47 shows the difference between fatigue response of the thinner and the thicker sheets for a representative FSW test at 1500 rpm and 220 mm/min. In the Al-10%Si alloy, very subtle difference is seen between the two thicknesses of material (the thinner sheet shows a bit better life).

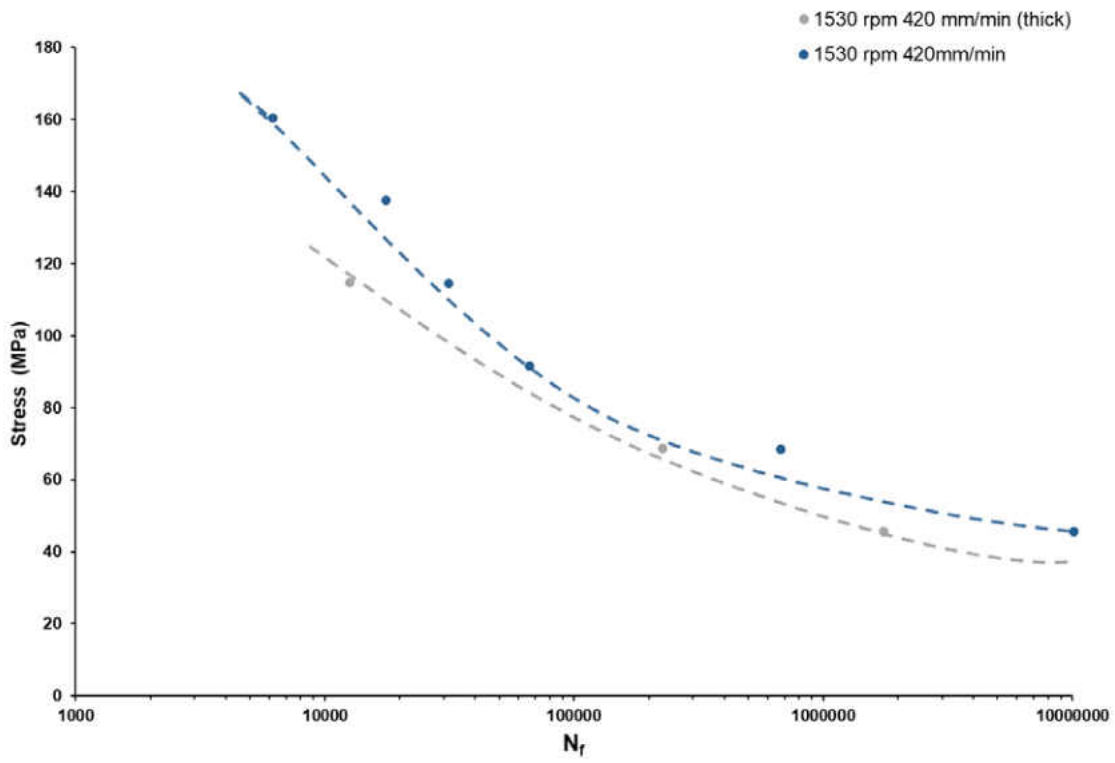

Figure 4-47: The effect of sheet thickness on the fatigue response of FSWed AM60 (1500 rpm and 420 mm/min)

4.2.4 SEM Fracture Surface Analysis

The fracture surfaces were analyzed by the SEM to reveal the mechanisms and the type of fracture of the samples that undergo fatigue testing. During fatigue testing, cracks initiate from the imperfections (either surface or internal) then grow continuously until the point where the remaining material is overstressed. The next step is unstable crack growth and final fracture (failure). Figure 4-48 shows a crack initiation point for the FSWed sample

employing 1530 RPM rotational and 114 mm/min traverse speed (serrations are clearly observed).

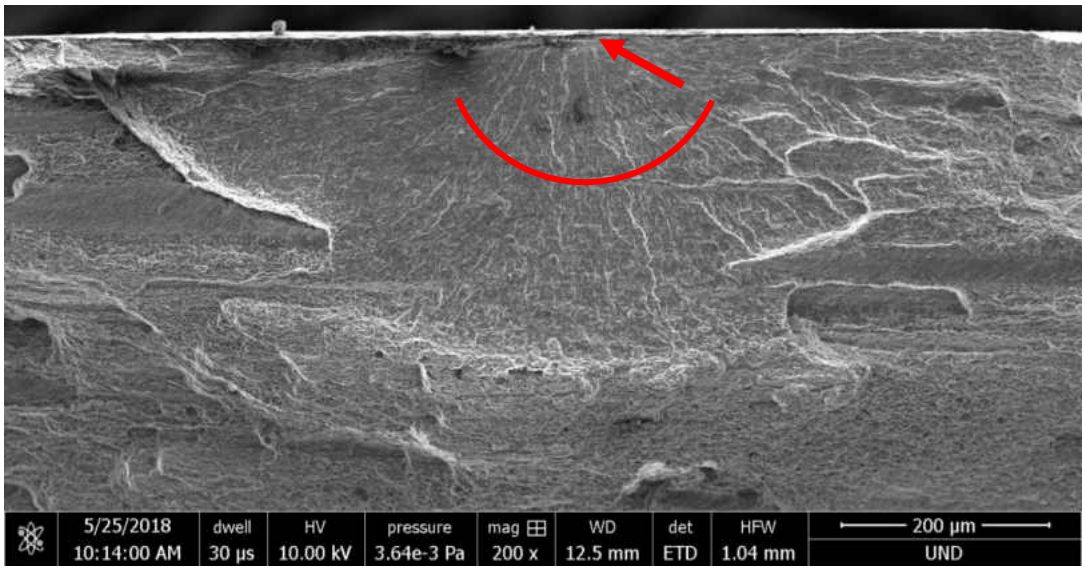

Figure 4-48: The red arc shows the beach marks which direct to the fatigue crack initiation point at the red arrow. (1530 RPM, 114 mm/min)

The dominant feature on the fracture surface is the extensive presence of dimple markings (Fig. 4-49 through 4-51). These dimples are an indication that it is a ductile type of fracture [144]. As mentioned previously the stirring action of the FSW tool refines and uniformly distributes the Si particles throughout the SZ, breaking the network of brittle blades/fibers and converting them to broken/spheroidized particles. This improves the ductility in the SZ as compared to the brittle fracture of the non-processed (as-cast) materials [57] where casting voids and Si fibers directly contribute to the brittle behavior of the material. This is because of the elimination of sharp tips and corners of the large brittle Si fibers and conversion of them to small broken particles that are evenly distributed in the matrix because of the stirring action of the rotating tool. This agrees with the findings from the microstructure, hardness, and fatigue results. Literature review on tensile strength of the FSWed Al-Si alloys also show a significant increase in the uniform elongation and

toughness in the SZ as compared to the as-cast Al-Si alloy (figure 4-52) [144, 141, 145, 57, 146].

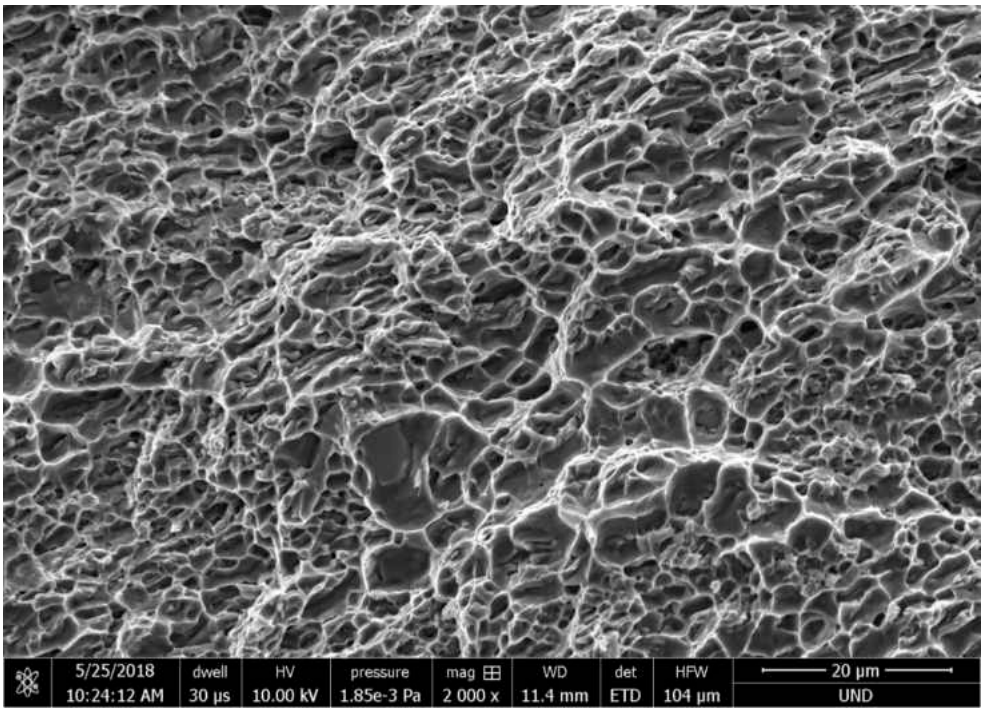

Figure 4-49: SEM fractograph showing considerable ductile-dimple structure in the fracture surface (1530 RPM, and 114 mm/min)

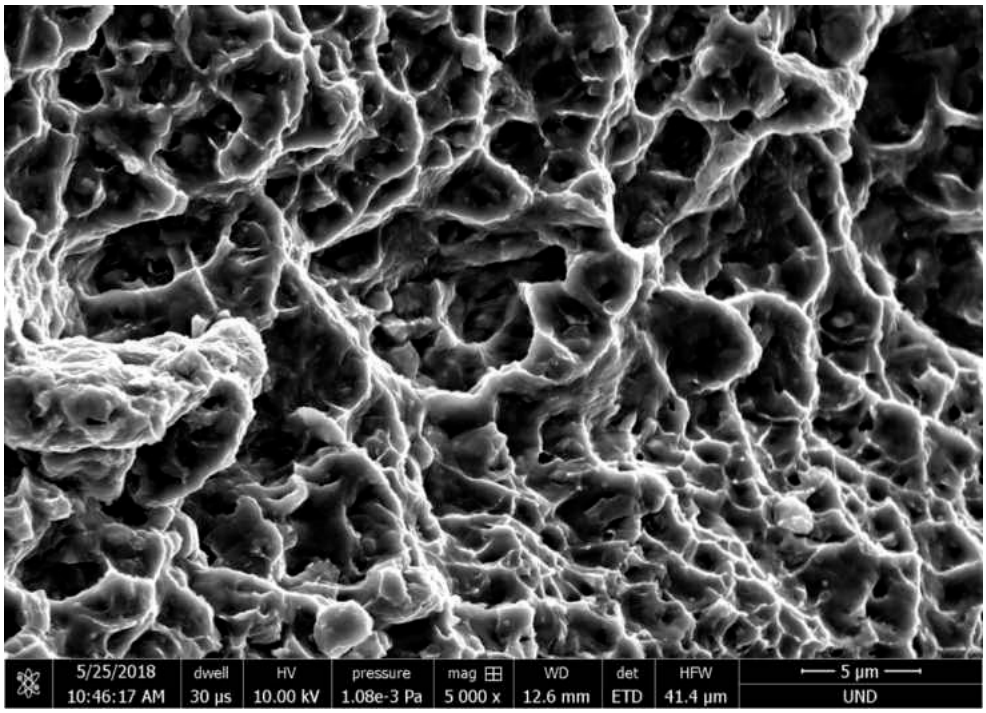

Figure 4-50: SEM fractograph showing considerable ductile-dimple structure in the fracture surface (1200 RPM, and 114 mm/min)

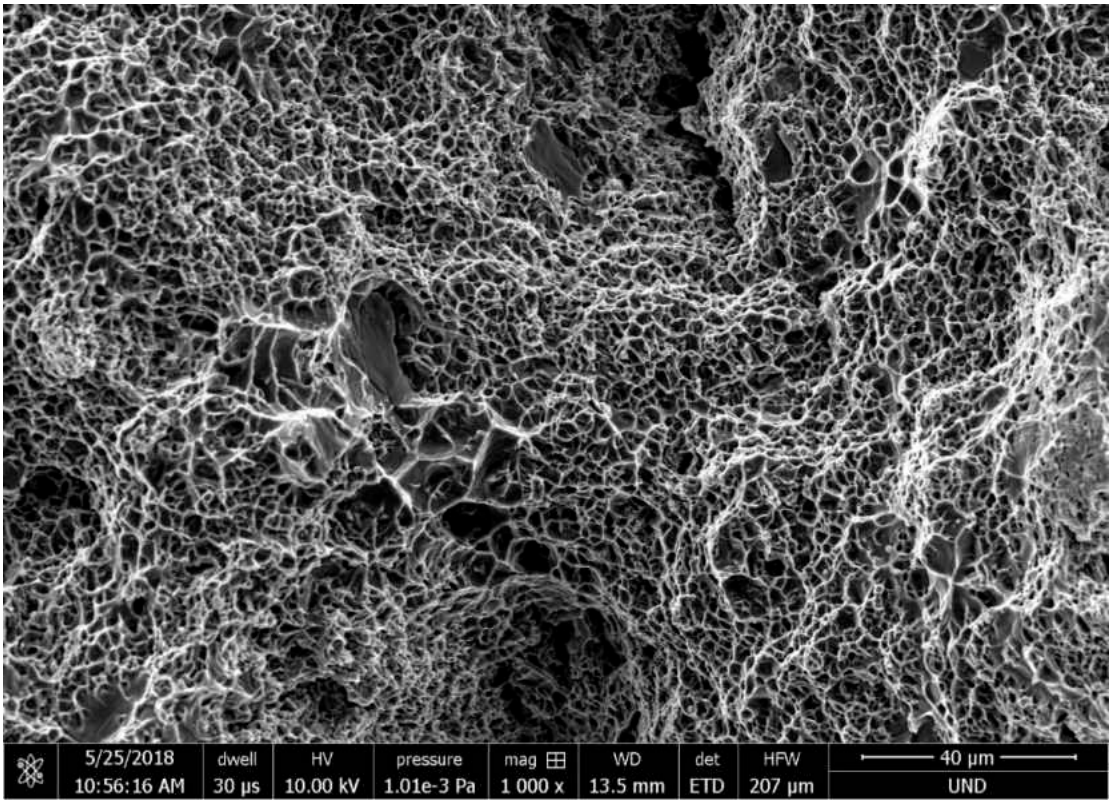

Figure 4-51: Ductile failure and the crack in this weld. (1530 RPM, and 420 mm/min)

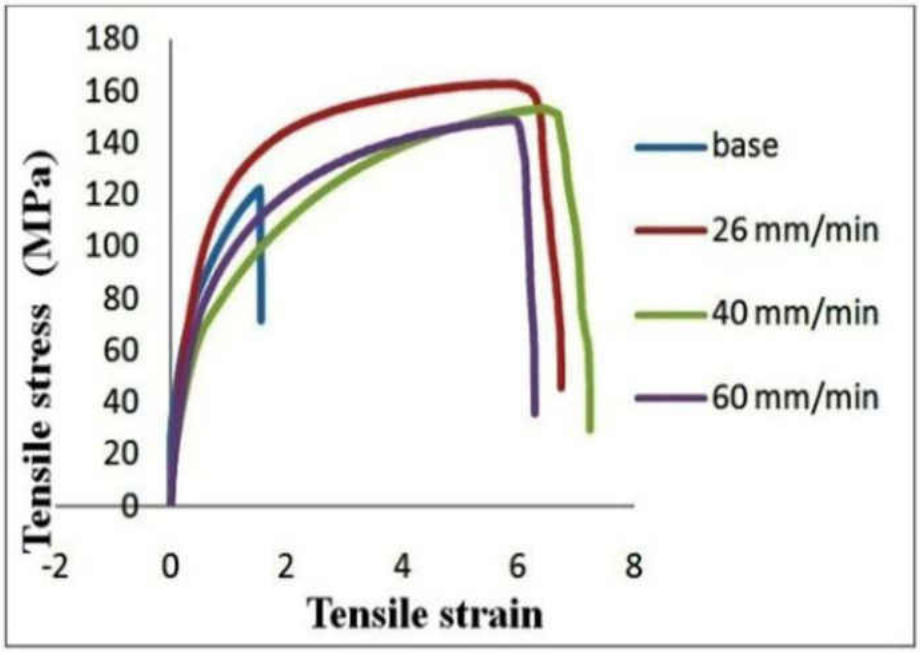

Figure 4-52: [57] Stress verses strain in base and FSPed samples at various process parameters

4.3 Comparison between AM60 Mg alloy and Al-10Si Aluminum alloy

Though the microstructural changes, induced by the FSW tool, of the AM60 Mg alloy and the Al-10%Si alloy are quite similar, a couple of distinct differences are observed. The base metal of the AM60 alloy consists of α-Mg grains and eutectic β-$Mg_{17}Al_{12}$ phase and eutectic α which is distributed along the grain boundaries (Fig 4-53a). While the BM Al-10%Si consists of an α-Mg phase and an Al-Si eutectic region which possesses course Si-particles in the shape of needle like plates (Fig 4-53b) distributed on α-Al grain boundaries. During the FSW process, both alloys undergo severe plastic deformation which results in dynamic recrystallization of the grains within the SZ caused by the rotating tool and frictional heat. The AM60 alloy is indicative of recrystallized equiaxed, fine grains which are evident in the SEM image shown in Figure 4-54a. The Al-10%Si alloy undergoes grain refinement, but the Si fibers go through spheroidization creating sphere shaped Si particles evenly distributed throughout the stirred zone (Fig. 4-54b).

a. b.

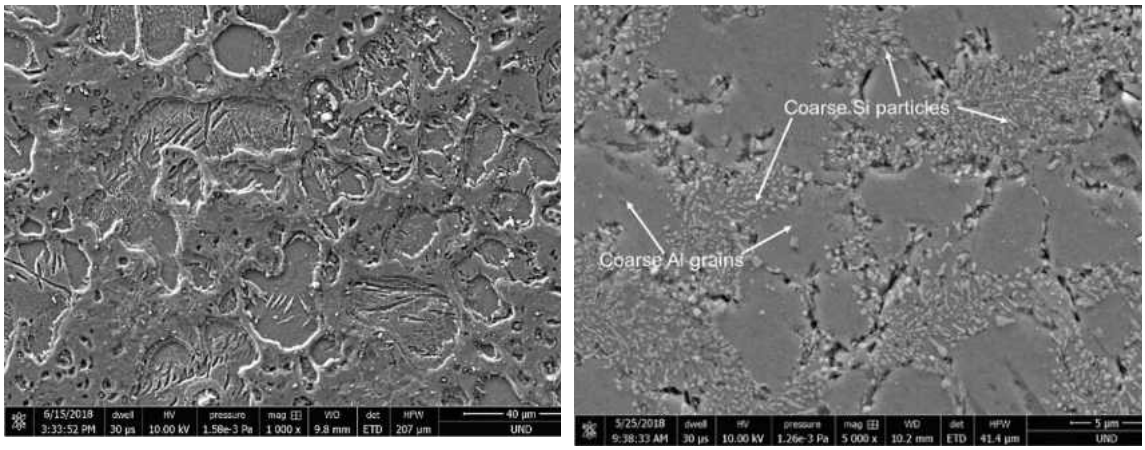

Figure 4-53: SEM micrograph of a) AM60 alloy b) Al-10%Si alloy

a. b.

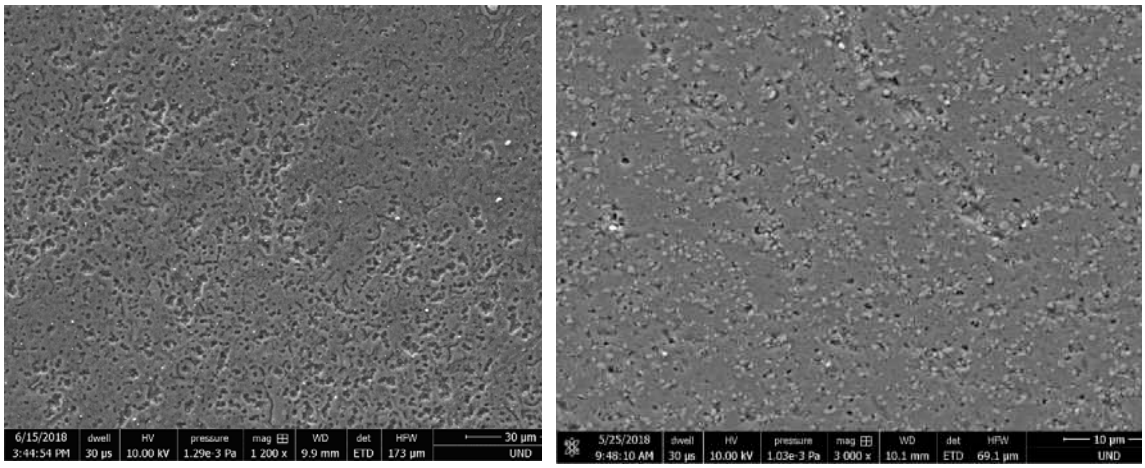

Figure 4-54: SEM micrograph showing a) the recrystallized grains of the SZ for AM60 and b) the sphere-shaped particles which are evenly distributed in the SZ of the Al-10%Si alloy

Upon the FSW process, the SZ of the AM60 Mg alloy becomes harder than the BM whereas for the Al-10%Si Al alloy it becomes softer. Figure 4-55 is a comparison of the hardness of the AM60 and the Al-10%Si at 635 RPM and 114 mm/min. The hardness of the Mg alloys has been shown to be affects by refined grains created by sever plastic deformation as compared to the SZ hardness for the Al –Si alloy which is mainly controlled by the distribution of the Si fibers, which as they undergo plastic deformation are broken and spheroidized into smaller sphere-shaped particles in-turn reducing the hardness of the metal. It is worth mentioning that both grain refinement and Si spheroidization would

happen in the SZ of the Al-Si10 alloy. However, according to the hardness measurements, it seems that Si spheroidization (conversion of long brittle eutectic Si blades to broken spheroidized particles) is the dominant controlling mechanism in defining the SZ microstructure in the Al-Si10 alloy.

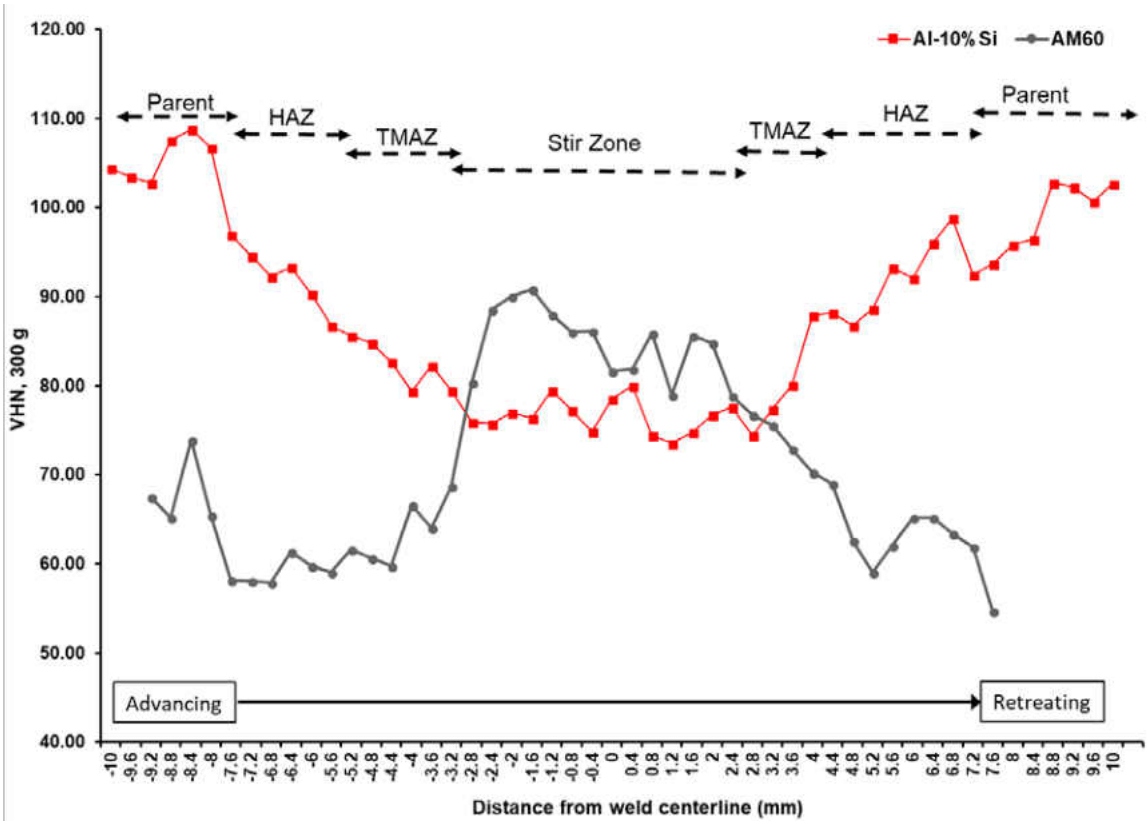

Figure 4-55: Hardness for AM60 and Al-10%Si at 635 RPM and 114 mm/min

The fracture surface of the AM60 shows a brittle/ductile combination nature. The dominant feature on the fracture surface was ductile dimple markings (Fig 4-56), that being said, there are isolated zones on the fracture surface that show a brittle fracture (Fig 4-57) of striation-like features present. This is an indicative of a ductile fracture but the striation like features on the fracture surface specify a brittle nature (Fig. 4-56a). Al-10%Si shows dimple markings as the dominant feature which indicates a ductile type of fracture (Fig. 4-56). This agrees with the dominant phenomena controlling the microstructure of the Al-

Si10 alloy in the SZ. As mentioned before, rotating FSW tool results in (*i*) spheroidization of the Si particles and (*ii*) even distribution of the broken Si particles in the SZ matrix. Because of the directional anisotropy as well as sharp tips/terminal of the Si blades are excluded, the hardness in softened. Besides, Si particles would be distributed uniformly/evenly in the matrix as compared with the non-processed microstructure where eutectic Si colony is precipitated on the α-Mg grain boundaries (See Fig. 4-58).

a. **b.**

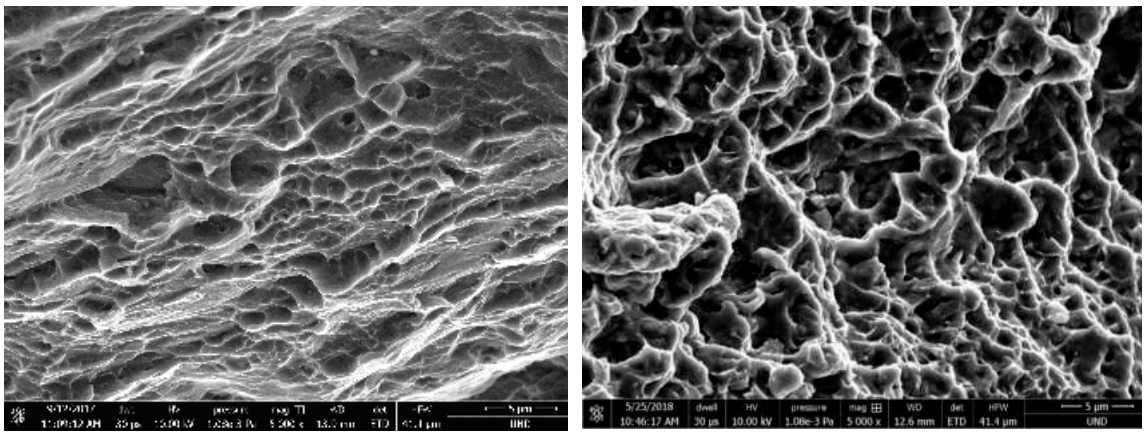

Figure 4-56: SEM fractograph of a) AM60 at 1530 RPM and 220 mm/min and b) Al-10%Si at 1200 RPM and 114 mm/min

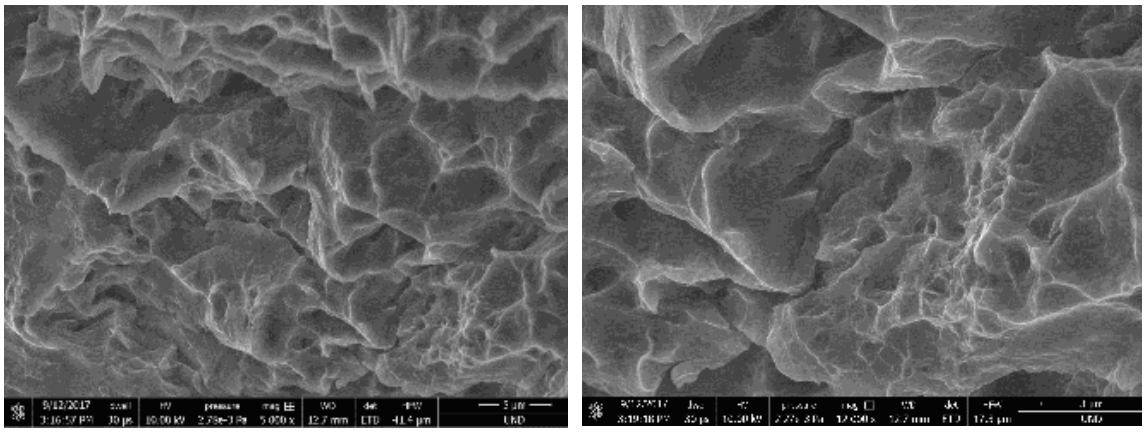

Figure 4-57: Features on the fracture surface confirming a mixture of brittle/ductile fracture (1530 RPM, and 48 mm/min).

a. b.

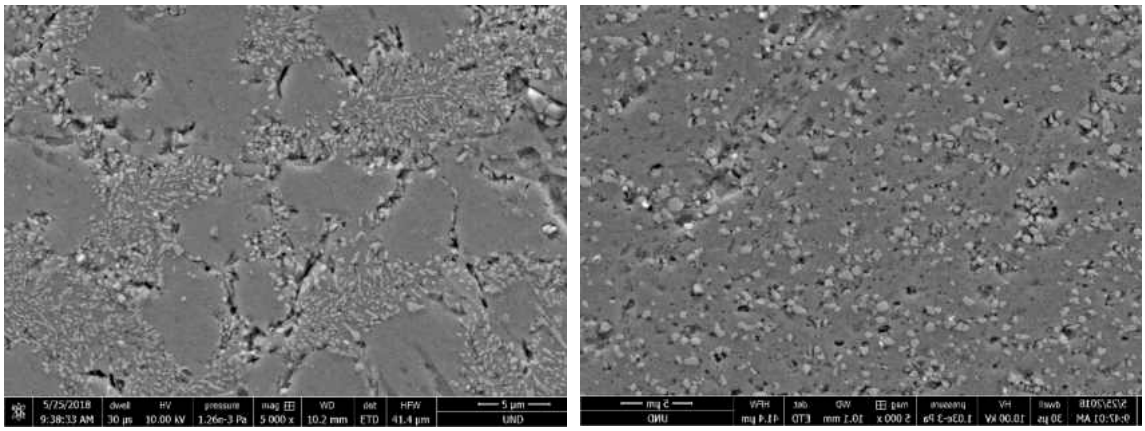

Figure 4-58: SEM micrograph of A1-10% Si showing a) as received microstructure with Si colony precipitated on the α-Mg grain boundaries b) FSWed microstructure with Si particles uniformly distributed in the matrix.

In AM60 Mg alloys there was an improvement in fatigue life when the rotational speed is held constant and the traverse speed was increased. This is opposite to the Al-10%Si alloy where the fatigue life was improved when the traverse speed is slower. With the AM60 alloy when the traverse speed is held constant and the rotational speed in increased the SZ becomes hotter, this promoted grain growth which increases ductility in the alloy and improves fatigue life. Compared to the Al-10%Si alloy where there is no change observed when the traverse speed is held constant there is no change in the fatigue life as the rotational speed is varied. When the thickness of the alloys was varied there was little effect on the fatigue life of the Al-10%Si alloy and an improved fatigue life was detected with the thinner sheets of the AM60 alloy.

CHAPTER V

5 CONCLUSIONS AND FUTURE WORK

The goal of this research was to understand the relationship between hardness, fatigue strength and microstructural features of two FSWed non-ferrous cast alloys (i.e. AM60 and Al-Si10). In this study hardness and fatigue testing was performed on several different as-cast AM60 and Al-Si FSW joints using different parameters (i.e. tool rotational and tool traverse speeds). The fracture surface and microstructural features of the joints were discussed. This chapter presents conclusions of the research results and recommendations for further understanding the relationship between the FSW parameters, the microstructure and the mechanical properties.

5.1 AM60 Mg Alloy

1. The AM60 Mg sheets (thickness of 4 mm) were successfully welded by the FSW process and no macro level defects were found under tool rotational and traveling speeds of 635 rpm (48 mm/min), 1200 rpm (48 mm/min), and 1200 rpm (114 mm/min).

2. With increase in the tool rotational speed, the hardness level decrease in all regions of the weld in both alloys. Also, highest hardness values, in the stir zone, belong to the one with slowest travel speed. Hardness (strength) is directly related to heat input and created temperature in the SZ.

3. Decrease in the heat input results in higher hardness (strength) in the SZ and therefore improved fatigue life.

4. According to the hardness profiles of the FSWed samples, fatigue cracks must initiate in the HAZ and TMAZ due to the coarse and non-uniform microstructure of these regions and therefore lower hardness values.

5. Fatigue life of thinner FSWed sheets is better than thicker ones (statistically speaking there are less number of defects in a smaller volume of material, i.e. thinner sheet). Void initiation, growth, and coalescence (possibly from $Al_{12}Mg_{17}$ phase particles) result in the extensive presence of ductile dimple markings as dominant feature on the fracture surface.

5.2 Al-Si Al Alloy

1. The Al-10% Si sheets (4 mm think) were successfully welded using the FSW process. There were no macro level defects found under tool rotational speed and traverse speed of 635 RPM (114 mm/min, 1200 RPM (114 mm/min), and 1530 RPM (420 mm/min).

2. The microstructure in the SZ changes drastically compared with the base metal. The coarse and non-uniformly distributed Si blades/fibers in the BM are broken down into smaller, spherical shaped particles in a process known as spheroidization. These spheroidized particles are evenly distributed through the SZ.

3. FSW causes the SZ to become softer than the parent material. This is caused by the spheroidization and even distribution of the Si particles through the SZ. Coarse and long Si blades, with sharp tips and corners that are heterogeneously distributed in the as-cast microstructure are converted to small spheroidized particles with aspect ratio ~1.

4. When the rotational speed is held constant at 635 rpm and the traverse speeds are varied, there is not much change seen in the hardness values. When the rotational speed is held constant at 1200 RPM/1530 RPM, and the traverse speed is decreased the SZ structure becomes softer.

5. Hardness profile indicates the crack initiation was either in the SZ or TMAZ due to the low hardness value in these regions.

6. When the traverse speed is held constant there were two separate observations made. At the lower traverse speed as the rotation speed varies there is no changes seen in the hardness but at the higher traverse speed (420 mm/min) as the rotational speed is decreased the alloy becomes softer in the SZ.

7. At lower travel speeds the heat input (temperature) is increased; this caused the Al-10%Si alloy to become more ductile and improve the fatigue life. The rotational speed has no influence on the fatigue profile.

8. The dominant failure method was observed as ductile fracture which was indicated by the dimple markings on the fracture surface. This is in agreement with the Si spheroidization phenomenon in the SZ which provides ductility by removing stress concentration points of eutectic Si fibers in the as cast structure and converting them to spheroidized particles in the SZ.

5.3 Future Work

The following are recommended to develop the relationships between local mechanical properties and microstructural features:

- Use electron back-scattering diffraction (EBSD) to further assess the grain size and morphology of both AM60 and Al-10%Si alloys and evaluate the texture in the SZ of these alloys.
- Study the effects of different tool profiles on the microstructure and fatigue response of the AM60 and Al-10%Si alloys and determine the tool which provides optimum response.

- Use TEM to study the mechanical twinning and investigate how they contribute to the strengthening in the SZ.
- Incorporate other FSW parameters in the study and use DOE to determine the FSW parameters which provide optimum mechanical properties.
- Study the feasibility of FSW dissimilar joint between the AM60 and the Al-10%Si and assess the inter-facial interaction using SEM/TEM

APPENDICES

Appendix A

Formulas

A1. Sum of Squares Equations

$$SS_T = \sum_{i=1}^{a}\sum_{j=1}^{b}\sum_{k=1}^{n} y_{ijk}^2 - \frac{y_{...}^2}{abn} \quad (1)$$

$$SS_{RPM} = \frac{1}{bn}\sum_{i=1}^{a} y_{i..}^2 - \frac{y_{...}^2}{abn} \quad (2)$$

$$SS_{mm/min} = \frac{1}{an}\sum_{j=1}^{b} y_{.j.}^2 - \frac{y_{...}^2}{abn} \quad (3)$$

$$SS_{interactions} = \sum_{i=1}^{a}\sum_{j=1}^{b} y_{ij.}^2 - \frac{y_{...}^2}{abn} - SS_{RPM} - SS_{mm/min} \quad (4)$$

$$SS_E = SS_T - SS_{RPM} - SS_{mm/min} - SS_{interactions} \quad (5)$$

A2. Degreed of Freedom Equations

$$dof_T = abn - 1 \quad (6)$$

$$dof_{RPM} = a - 1 \quad (7)$$

$$dof_{mm/min} = b - 1 \quad (8)$$

$$dof_{interactions} = (a-1)(b-1) \quad (9)$$

$$dof_{error} = ab(n-1) \quad (10)$$

A3. Mean Square Equations

$$MS_{RPM} = \frac{SS_{RPM}}{dof_{RPM}} \quad (11)$$

$$MS_{mm/min} = \frac{SS_{mm/min}}{dof_{mm/min}} \tag{12}$$

$$MS_{interactiona} = \frac{SS_{interactions}}{dof_{interactions}} \tag{13}$$

$$MS_E = \frac{SS_E}{dof_E} \tag{14}$$

A4. F-value Equations

$$F_{RPM} = \frac{MS_{RPM}}{MS_E} \tag{15}$$

$$F_{mm/min} = \frac{MS_{mm/min}}{MS_E} \tag{16}$$

$$F_{interaction} = \frac{MS_{interactions}}{MS_E} \tag{17}$$

Appendix B

Minitab Output

B1. Two-way ANOVA: hardness versus RPM, mm/min

```
Source       DF       SS       MS       F      P
RPM           2   958.06  479.030  158.37  0.000
mm/min        2   561.59  280.794   92.83  0.000
Interaction   4   910.94  227.736   75.29  0.000
Error        36   108.89    3.025
Total        44  2539.48

S = 1.739   R-Sq = 95.71%   R-Sq(adj) = 94.76%
               Individual 95% CIs For Mean Based on
               Pooled StDev
RPM      Mean  --------+---------+---------+---------+-
 635  82.8067                                  (--*-)
1200  75.3867            (-*--)
1530  71.7133  (--*-)
               --------+---------+---------+---------+-
                    73.5      77.0      80.5      84.0
                 Individual 95% CIs For Mean Based on
                 Pooled StDev
mm/min     Mean  ---+---------+---------+---------+------
 48     80.7533                               (--*--)
220     77.0267                   (--*--)
422     72.1267  (--*--)
                 ---+---------+---------+---------+------
                 72.0      75.0      78.0      81.0
```

B2. One-way ANOVA: hardness versus RPM

```
Source  DF      SS     MS      F      P
RPM      2   958.1  479.0  12.72  0.000
Error   42  1581.4   37.7
Total   44  2539.5

S = 6.136   R-Sq = 37.73%   R-Sq(adj) = 34.76%
                         Individual 95% CIs For Mean Based on
                         Pooled StDev
Level   N    Mean  StDev  ---+---------+---------+---------+------
 635   15  82.807  3.845                        (------*-----)
1200   15  75.387  8.127         (------*-----)
```

```
1530   15  71.713  5.668  (-----*------)
                          ---+---------+---------+---------+------
                          70.0      75.0      80.0      85.0

Pooled StDev = 6.136
Grouping Information Using Tukey Method

RPM    N    Mean  Grouping
 635  15  82.807  A
1200  15  75.387    B
1530  15  71.713    B
Means that do not share a letter are significantly different.
Tukey 95% Simultaneous Confidence Intervals
All Pairwise Comparisons among Levels of RPM

Individual confidence level = 98.07%
RPM =  635 subtracted from:

RPM     Lower   Center   Upper  ----+---------+---------+---------+-----
1200  -12.870   -7.420  -1.970        (------*-------)
1530  -16.544  -11.093  -5.643  (-------*-------)
                               ----+---------+---------+---------+-----
                               -14.0      -7.0       0.0       7.0
RPM = 1200 subtracted from:

RPM    Lower  Center  Upper  ----+---------+---------+---------+-----
1530  -9.124  -3.673  1.777             (-------*-------)
                           ----+---------+---------+---------+-----
                           -14.0      -7.0       0.0       7.0
Grouping Information Using Fisher Method
RPM    N    Mean  Grouping
 635  15  82.807  A
1200  15  75.387    B
1530  15  71.713    B

Means that do not share a letter are significantly different.
Fisher 95% Individual Confidence Intervals
All Pairwise Comparisons among Levels of RPM

Simultaneous confidence level = 87.97%
```

```
RPM =  635 subtracted from:

RPM     Lower   Center   Upper  ------+---------+---------+---------+---
1200  -11.942   -7.420  -2.898        (-------*------)
1530  -15.615  -11.093  -6.572  (-------*------)
                               ------+---------+---------+---------+---
                                 -12.0      -6.0       0.0       6.0
RPM = 1200 subtracted from:

RPM    Lower  Center  Upper  ------+---------+---------+---------+---
1530  -8.195  -3.673  0.848              (-------*------)
                            ------+---------+---------+---------+---
                              -12.0      -6.0       0.0       6.0
```

B3. One-way ANOVA: hardness versus mm/min

```
Source  DF      SS     MS     F      P
mm/min   2   561.6  280.8  5.96  0.005
Error   42  1977.9   47.1
Total   44  2539.5

S = 6.862   R-Sq = 22.11%   R-Sq(adj) = 18.41%
                          Individual 95% CIs For Mean Based on
                          Pooled StDev
Level   N    Mean  StDev  ---------+---------+---------+---------+
 48    15  80.753  8.695                       (--------*--------)
220    15  77.027  4.153              (--------*--------)
422    15  72.127  6.960  (--------*--------)
                          ---------+---------+---------+---------+
                                72.0      76.0      80.0      84.0

Pooled StDev = 6.862

Grouping Information Using Tukey Method

mm/min   N    Mean  Grouping
 48     15  80.753  A
220     15  77.027  A B
422     15  72.127    B

Means that do not share a letter are significantly different.


Tukey 95% Simultaneous Confidence Intervals
```

All Pairwise Comparisons among Levels of mm/min

Individual confidence level = 98.07%

mm/min = 48 subtracted from:

```
mm/min    Lower  Center   Upper     -+---------+---------+---------+--------
220      -9.822  -3.727   2.369             (--------*-------)
422     -14.722  -8.627  -2.531      (--------*-------)
                                     -+---------+---------+---------+--------
                                  -14.0      -7.0       0.0       7.0
```

mm/min = 220 subtracted from:

```
mm/min    Lower  Center  Upper     -+---------+---------+---------+--------
422     -10.995  -4.900  1.195           (--------*--------)
                                     -+---------+---------+---------+--------
                                  -14.0      -7.0       0.0       7.0
```

Grouping Information Using Fisher Method

mm/min	N	Mean	Grouping
48	15	80.753	A
220	15	77.027	A B
422	15	72.127	B

Means that do not share a letter are significantly different.

Fisher 95% Individual Confidence Intervals
All Pairwise Comparisons among Levels of mm/min

Simultaneous confidence level = 87.97%

mm/min = 48 subtracted from:

```
mm/min    Lower  Center   Upper   ---+---------+---------+---------+------
220      -8.784  -3.727   1.330           (--------*-------)
422     -13.684  -8.627  -3.570   (--------*-------)
```

```
                                  ---+---------+---------+---------+------
                                 -12.0       -6.0        0.0        6.0

mm/min = 220 subtracted from:

mm/min   Lower  Center  Upper   ---+---------+---------+---------+------
422     -9.957  -4.900  0.157          (---------*-------)
                                 ---+---------+---------+---------+------
                                -12.0       -6.0        0.0        6.0
```

REFERENCES

[1] P. Asadi, K. Kazemi-Choobi and A. Elhami, "Welding of Magnesium Alloys, New Features on Magnesium Alloys, Dr. Waldemar A. Monteiro (Ed.)," InTech, 2012.

[2] H. Rao, J. Jordon, S. Boorgu, H. Kang, W. Yuan and X. Su, "Influence of the key-hole on fatigue life in friction stir linear welded aluminum to magnesium," International Journal of Fatigue 105, pp. 16-26, 2017.

[3] Y. Zhang, C. Pan and A. Male, "Improved microstructure and properties of 6061 aluminum alloy weldments using a double-sided arc welding process," Metall and Mat Trans A, p. 31: 2537, 2000.

[4] K. Máthis, F. Chmelík, M. Janeček, B. Hadzima, Z. Trojanová and P. Lukáč, "Investigating deformation processes in AM60 magnesium alloy using the acoustic emission technique," Acta materialia 54, pp. 5361-5366, 2006.

[5] S. M. Chowdhury, D. L. Chen, S. D. Bhole and X. Cao, "Tensile properties of a friction stir welded magnesium alloy: Effect of pin tool thread orientation and weld pitch," Materials Science and Engineering, vol. 527, no. 21-22, pp. 6064-6075, 2010.

[6] R. Rodriguez, J. Jordon, M. Rao, H. Badarinarayan, W. Yuan and H. E. Kadiri, "Microstructure, texture, and mechanical properties of friction stir spot welded rare-earth containing ZEK100 magnesium alloy sheets," Mater Sci Eng, vol. 618, pp. 637-644, 2014.

[7] M. Rao, R. Rodriguez, J. Jordon, M. Barkey, Y. Guo and H. Badarinarayan, "Friction Stir Spot Welding of Rare-Earth Containing ZEK100 Magnesium Alloy Sheets," Material Design, vol. 56, pp. 750-754, 2014.

[8] W. Yuan, B. Carlson, R. Verma and R. Szymanski, "Study of top sheet thinning during friction stir lap welding of AZ31 magnesium alloy," Sci Technol Weld Join, vol. 17, pp. 375-380, 2012.

[9] N. Afrin, D. Chen, C. Cao and M. Jahazi, "Microstructure and tensile properties of friction stir welded AZ31B magnesium alloy," Materials Science and Engineering: A, vol. 472, no. 1-2, pp. 179-186, 2008.

[10] ASM International, Chapter 14 - fatigue. Elements of Metallurgy and Engineering Alloys, 2008.

[11] S. Pappas, "Facts about Magnesium," LIVESCIENCE, 16 Dec. 2014. [Online]. Available: https://www.livescience.com/28862-magnesium.html. [Accessed 1 Jun 2018].

[12] J. I. Skar and D. Albright, "Emerging Trends In Corrosion Protection Of Magnesium Die Castings," Magnesium Tech., pp. 255-261, 2002.

[13] M. M. Avedesian and H. Baker, "Magnesium and Magnesium Alloys," ASM International. Handbook Committee, 1999.

[14] "Magnesium and Magnesium Alloys," in Metals Handbook, Desk ed.; 2nd ed., ASM International, 1998, pp. 599-574.

[15] P. Sharifi, "Structure-Property Relationships of Magnesium Alloys," Electronic Thesis and Dissertation Repository. 816, 2012.

[16] A. K. Dahle, Y. C. Lee, M. D. Nave, P. L. Schaffer and D. H. StJohn, "Development of the as-cast microstructure in magnesium–aluminium alloys," Journal of Light Metals, vol. 1, no. 1, pp. 61-72, 2001.

[17] A. A. Luo, "Magnesium casting technology for structural applications," Journal of Magnesiul and Alloys, vol. 1, no. 1, pp. 2-22, 2013.

[18] M. P. Groove, Fundamentals of Modern Manufacturing: Materials, Processes, and Systems, 6th Edition, Wiley, 2016.

[19] L. Chen, C. Wang, W. Wu, Z. Liu, G. M. Stoica, L. Wu and P. K. Liaw, "Low-cycle fatigue behavior of an as-extruded AM50 magnesium alloy," Metallurgical and Materials Transactions A, vol. 38, no. 13, pp. 2235-2241, 2007.

[20] AZoM, "Magnesium AM60B Cast Alloy," AZO Materials, 29 Jul 2013. [Online]. Available: https://www.azom.com/article.aspx?ArticleID=9237.

[21] R. Mishra and Y. Ma, "Friction stir welding and processing," Material Science and Engineering R 50, pp. 1-78, 2005.

[22] J. A. Esparza, W. C. Davis and L. E. Murr, "Microstructure-property studies in friction-stir welded, Thixomolded magnesium alloy AM60," Journal of Materials Science, vol. 38, no. 5, pp. 941-952, 2003.

[23] R. Brown, "Future of Magnesium Developments in 21st Century," in Materials Science & Technology Conference, Pittsburgh, PA, USA, 2008.

[24] G. Wardlow, "A Changing World with Different Rules – New Opportunities for Magnesium Alloys?," in 64th Annual World Magnesium Conference, Vancouver, BC, Canada, 2007.

[25] O. Pashkova, I. Ostrovsky and Y. Henn, "Present State and Future of Magnesium Application in Aerospace Industry," in New Challenges in Aeronautics, Moscow, 2007.

[26] C. D. Lee, "Dependence of tensile properties of AM60 magnesium alloy on microporsity and grain size," Materials Science and Engineering: A, Vols. 454-455, pp. 575-580, 2007.

[27] N. Dziubińska, A. Gontarz, M. Dziubiński and M. Barszcz, "The Forming of Magnesium Alloy Forgings for Aircraft and Automotive Applications," Advances in Science and Technology Research Journal 10, pp. 158-168, 2016.

[28] C. Blawert, N. Hort and K. Kainer, "Automotive Applications of Magnesium and its Alloys," Trans. Indian Inst. Met, vol. 57, no. 4, pp. 397-408, 2004.

[29] X. Zhang, M. Wang, Z. Sun and H. Hu, "Section thickness-dependent tensile properties of squeeze cast magnesium alloy AM60," China Foundry, vol. 9, no. 2, pp. 179-183, 2011.

[30] B. Powell, P. Krajewski and A.A. Luo, "Materials Design and Manufacturing for Lightweight Vehicles," in Chapter 4: Magnesium Alloys, book chapter, Cambridge, UK, Woodhead Publishing Ltd, 2010, pp. 114-116.

[31] S. G. Lee, G. R. Patel, A. M. Gokhale, A. Sreeranganathan and M. F. Horstemeyer, "Quantitative fractographic analysis of variability in the tensile ductility of high-pressure die-cast AE44 Mg-alloy," Materials Science and Engineering: A, vol. 427, no. 1-2, pp. 255-262, 2006.

[32] F. Zheng, Y. Wu, L. Peng, X. Li, P. Fu and W. Ding, "Microstructures and mechanical properties of friction stir processed Mg–2.0Nd–0.3Zn–1.0Zr magnesium alloy," Journal of Magnesium and Alloys, vol. 1, no. 2, pp. 122-127, 2013.

[33] B. Gwynne and B. Lyon, "Magnesium alloys in aerospace applications, Past Concerns, Current Solutions," in Triennial International Aircraft Fire & Cabin Safety Research Conference, 2007.

[34] International Magnesium Association, Magnesium's Tough Strength Endures Abuse to Protect Portable Electronic Devices, Wauconda, IL, USA: International Magnesium Association, 2008.

[35] N. Li, P. Tsung-Yu, R. Cooper, D. Houston, Z. Feng and M. Santella, "Friction stir welding of magnesium AM60 alloy," Magnesium Technology, pp. 19-23, 2004.

[36] K. Gall, G. Biallas, H. Maier, P. Gullett, M. Horstemeyer, D. McDowell and J. Fan, "In-situ observations of high cycle fatigue mechanisms in cast AM60B magnesium in vacuum and water vapor environments," International Journal of Fatigue, vol. 26, no. 1, pp. 59-70, 2004.

[37] The Minerals, Metals & Materials Society, "Magnesium Alloys for Automotive Applications," The Minerals, Metals & Materials Society, [Online]. Available: http://www.tms.org/Communities/FTAttachments/Mg%20Alloys%20for%20Automotive.pdf.

[38] M. K. Kulekci, "Magnesium and its alloys applications in automotive industry," Int J Adv Manuf Technol, vol. 39, pp. 851-865, 2008.

[39] J. Weiler, J. Wood, R. Klassen, R. Berkmortel and G. Wangb, "Variability of skin thickness in an AM60B magnesium alloy die-casting," Materials Science and Engineering: A, vol. 419, no. 1-2, pp. 297-305, 2006.

[40] S. Pappas, "Facts About Aluminum," LiveScience, 28 Sept. 2014. [Online]. Available: https://www.livescience.com/28865-aluminum.html. [Accessed 1 June 2018].

[41] Metalex, "35 facts about Aluminium – the planet's most abundant metal," Metalex, 2018. [Online]. Available: http://www.metalex.co.uk/35-facts-aluminium-planets-abundant-metal/.

[42] H. Brown, Aluminum and its Applications, Pitman Publishing Corporation, 1948.

[43] J. E. Hatch, Aluminum: Properties and Physical Metallurgy, American Society for Metals, 1984.

[44] Royal Society of Chemistry, "Periodic table," Royal Society of Chemistry, 2017. [Online]. Available: http://www.rsc.org/periodic-table/element/13/aluminium.

[45] Wolfram Research, Inc., "Technical data for Aluminum," PeriodicTable, 28 Oct 2017. [Online]. Available: http://periodictable.com/Elements/013/data.html.

[46] D. Segal, Materials for the 21st Century, Oxford University Press, 2017-05-18.

[47] ASM International, "Aluminum and Aluminum Alloys," in Metals Handbook, Desk ed.; 2nd ed., ASM International, 1998, pp. 417-505.

[48] AlcoTac, "How and why alloying elements are added to aluminum," AlcoTac, 2015. [Online]. Available: http://www.alcotec.com/us/en/education/knowledge/qa/How-and-why-alloying-elements-are-added-to-aluminum.cfm.

[49] Total Materia, "Aluminum Alloys – Effects of Alloying Elements," Total Materia, 2002. [Online]. Available: http://www.totalmateria.com/Article55.htm.

[50] J. G. Kaufman and E. L. Rooy, Aluminum Alloy Castings: Properties, Processes, and Applications, ASM International, 2004.

[51] ME Mechanical, "Die Casting Process," ME Mechanical, 15 Mar. 2016. [Online]. Available: https://me-mechanicalengineering.com/die-casting-process/. [Accessed 08 Jun. 2018].

[52] M. Zanani, "Al-Si Cast Alloys - Microstructure and Mechanical Properties at Ambient and Elevated Temperature," School of Engineering, Jönköping University , Jönköping, Sweden, 2015.

[53] F. Paray and J. Gruzleski, "Microstructure—mechanical property relationships in a 356 alloy. Part I: Microstructure," Cast Met., vol. 7, pp. 29-40, 2016.

[54] EOS GmbH - Electro Optical Systems, "Material data sheet: Aluminum AlSi10Mg," 2009. [Online]. Available: http://www.agile-manufacturing.com/files/materials/aluminum.pdf.

[55] H. Fredriksson and U. Åkerlind, Materials Processing During Casting, Chichester: John Wiley & Sons Ltd, 2006.

[56] M. Haghshenas and J. Jamali, "Assessment of circumferential cracks in hypereutectic Al-Si clutch housings," Case Studies in Engineering Failure Analysis 8, pp. 11-20, 2017.

[57] N. Saini, D. Dwivedi, P. Jain and H. Singh, "Surface Modification of Cast Al-17%Si Alloys Using Friction Stir Processing," Procedia Engineering, vol. 100, pp. 1522-1531, 2015.

[58] E. Starke and J. Staley, "Application of modern aluminum alloys to aircraft," Progress in Aerospace Sciences, vol. 32, no. 2-3, pp. 131-172, 1996.

[59] W. Miller, L. Zhuang, J. Bottema, A. Wittebrood, P. D. Smet, A. Haszler and A. Vieregge, "Recent development in aluminium alloys for the automotive industry," Materials Science and Engineering A, vol. 280, pp. 37-49, 2000.

[60] J. Hirsch, "Aluminium in Innovative Light-Weight Car Design," Materials Transactions, vol. 52, no. 5, pp. 818-824, 2011.

[61] H. Ye, "An overview of the development of Al-Si-Alloy based material for engine applications," Journal of Materials Engineering and Performance, vol. 12, no. 3, pp. 288-297, 2003.

[62] K. J. Colligan, P. J. Konkol, J. J. Fisher and J. R. Pickens, "Friction Stir Welding Demonstrated for Combat Vehicle Construction," American Welding Society, 2003.

[63] O. Unal and M. Tiryakioğlu, "On the Ductility Potential and Assessment of Structural Quality in Mg Alloy Castings," Mater. Sci. Eng. A, vol. 643, pp. 51-54, 2015.

[64] R. Islamgaliev, O. Kulyasova, B. Mingler, M. Zehetbauer and A. Minkow, "Structure and Fatigue Properties of the Mg Alloy AM60 Processed By ECAP," Materials Science Forum, Vols. 584-586, pp. 584-586, 2008.

[65] O. Kulyasova, R. Islamgaliev, B. Mingler and M. Zehetbauer, "Microstructure and fatigue properties of the ultrafine-grained AM60 magnesium alloy processed by equal-channel angular pressing," Materials Science and Engineering: A, vol. 503, no. 1-2, pp. 176-180, 2009.

[66] J. Gou, A. T. Tang, F. S. Pan, J. She, S. Q. Luo, J. H. Ye, D. W. Shi and M. Rashad, "Influence of Sn addition on mechanical properties of gas tungsten arc welded AM60 Mg alloy sheets," Trans. Nonferrous Met. Soc. China, vol. 26, no. 8, pp. 2051-2057, 2006.

[67] A. Kiełbus, T. Rzychoń and R. Cibis, "Microstructureof AM50 die casting magnesium alloy," Journal of Achievements in Materials and Manufacturing Engineering, vol. 18, no. 1-2, pp. 135-138, 2006.

[68] J. Seo and S. Kim, "Mechanical Properties of 0.25-0.65wt% Ca0 Added AM60B Eco-Mg Diecastings at Room and Elevated Temperatures," Journal of Korea Foundry Society;, vol. 31, no. 1, pp. 11-17, 2011.

[69] M. Węglowski, "Microstructure of cast aluminium alloy AlSi9Mg after FSP proces," Archives of Foundary Engineering, vol. 14, no. 3, pp. 75-78, 2014.

[70] S. M. Aktarer, D. M. Sekban, H. Yanar and G. Purçek, "Effect of friction stir processing on tribological properties of Al-Si alloys," 2017 IOP Conf. Ser.: Materials Science and Engineering, vol. 174, 2017.

[71] B. Białobrzeska, Ł. Konat and R. Jasiński, "The Influence of Austenite Grain Size on the Mechanical Properties of Low-Alloy Steel with Boron," Metals, vol. 7, no. 1, p. 26, 2017.

[72] Y. Birol, "Impact of grain size on mechanical properties of AlSi7Mg0.3 alloy," Materials Science and Engineering: A, vol. 559, no. 1, pp. 394-400, 2013.

[73] C. D. Lee and K. S. Shin, "Effects of precipitate and dendrite arm spacing on tensile properties and fracture behavior of As-Cast magnesium-aluminum alloys," Metals and Materials International, vol. 9, no. 1, pp. 21-27, 2003.

[74] L. Ceschini, A. Morri, S. Toschi, S. Johansson and S. Seifeddine, "Microstructural and mechanical properties characterization of heat treated and overaged cast A354 alloy with various SDAS at room and elevated temperature," Materials Science and Engineering: A, vol. 648, pp. 340-349, 2015.

[75] C. Caceres, "On the effect of macroporosity on the tensile properties of the Al-7%Si-0.4%Mg casting alloy," Scripta Metallurgica et Materialia, vol. 32, no. 11, pp. 1851-1856, 1995.

[76] J. A. Francis and G. D. Cantin, "The role of defects in the fracture of an Al–Si–Mg cast alloy," Materials Science and Engineering: A, vol. 407, no. 1-2, pp. 322-329, 2005.

[77] M. Surappa, E. Blank and J. Jaquet, "Effect of macro-porosity on the strength and ductility of cast Al-7Si-0.3Mg alloy," Scripta METALLURGICA, vol. 20, pp. 1281-1286, 1986.

[78] S. Biswas, F. Sket, M. Chiumenti, I. Gutiérrez-Urrutia, J. M. Molina-Aldareguía and M. T. Pérez-Prado, "Relationship between the 3D porosity and β-phase distributions and the mechanical properties of a high pressure die cast AZ91 Mg alloy," Metallurgical and Materials Transactions A, vol. 44, no. 9, pp. 4391-4403, 2013.

[79] H. Hu, M. Zhou, Z. Sun and N. Li, "Tensile behaviour and fracture characteristics of die cast magnesium alloy AM50," Journal of Materials Processing Technology, vol. 201, no. 1-3, pp. 364-368, 2008.

[80] M. Grujicic, G. Arakere, H. V. Yalavarthy, T. He, C. F. Yen and B. A. Cheeseman, "Modeling of AA5083 Material-Microstructure Evolution During Butt Friction-Stir Welding," Journal of Materials Engineering and Performance, vol. 19, pp. 672-684, 2010.

[81] G. Çam, G. İpekoğlu, T. Küçükömeroğlu and S. Aktarer, "Applicability of Friction Stir Welding," Journal of Achievements in Materials and Manufacturing Engineering, vol. 80, no. 2, pp. 65-85, 2017.

[82] "Chapter 14 - Fatigue," in Elements of Metallurgy and Engineering Alloys, ASM International, 2008.

[83] A. Halfpenny, "A practical discussion on fatigue," in Managing Durability, 2008.

[84] K. A. Fraser, L. St-Georges and L. I. Kiss, "Optimization of Friction Stir Welding Tool Advance Speed via Monte-Carlo Simulation of the Friction Stir Welding Process," Materials, vol. 7, no. 5, pp. 3435-3452, 2014.

[85] S. Sattari, H. Bisadi and M. Sajed, "Mechanical Properties and Temperature Distributions of Thin Friction Stir Welded Sheets of AA5083," International Journal of Mechanics and Applications, vol. 2, no. 1, pp. 1-6, 2012.

[86] L. Trueba, G. Heredia, D. Rybicki and L. Johannes, "ffect of tool shoulder features on defects and tensileproperties of friction stir welded aluminum 6061-T6," Journal of Materials Processing Technology 219, vol. 219, pp. 271-277, 2015.

[87] F. G. Basmaji, Cyclic Fatigue Behavior of Friction Stir Welded AZ-Series Magnesium Alloys: MSc. Thesis, Hamilton, ON: McMaster University, 2016.

[88] M. Ericsson and R. Sandstrom, "Influence of welding speed on the fatigue of friction stir welds, and comparison with MIG and TIG," International Journal of Fatigue 25, pp. 1379-1387, 2003.

[89] D. E. Dilger, "AppleInsider," 24 Oct. 2012. [Online]. Available: https://appleinsider.com/articles/12/10/24/apple-slims-down-imac-40-with-friction-stir-welding-ditching-the-disc-drive. [Accessed 25 Nov. 2016].

[90] Sivakumar, V. Bose, D. Raguraman and D. Muruganandam, "Review Paper on Friction Stir Welding of various Aluminium Alloys," IOSR Journal of Mechanical and Civil Engineering, pp. 46-52, 2014.

[91] M. Hiten and M. Shalin, "A Review Paper on: Friction Stir Welding (FSW)," International Journal of Advanced Research in Engineering Science & Management, pp. 1-13, 2017.

[92] P. Cavaliere and P. D. Marco, "Friction stir processing of AM60B magnesium alloy sheets," Materials Science and Engineering A 462, pp. 393-397, 2007.

[93] J. Iwaszko, K. Kudła, K. Fila and M. Strzelecka, "The Effect of Friction Stir Processing (FSP) on the Microstructure and Properties of AM60 Magnesium Alloy," Arch. Metall. Mater., vol. 61, no. 3, pp. 1555-1560, 2016.

[94] S. Jana, R. S. Mishra, J. B. Baumann and G. Grant, "Effects of friction stir processing on fatigue behavior of an investment cast Al-7Si-0.6 Mg alloy," Acta Mater, vol. 58, pp. 989-1003, 2010.

[95] V. Sharma, S. Singh, C. Sharma and V. Upadhyay, "Mechanical and Microstructural Characterization of Friction Stir Welded Al-Si-Mg Alloy," All India Manufacturing Technology, Design and Research Conference 475, pp. 1-6, 2014.

[96] A. International, "ASTM E1823-13, Standard Terminology Relating to Fatigue and Fracture Testing," ASTM International, West Conshohocken, PA, 2013.

[97] H. Boyer, "Chapter: Fatigue Testing," in Atlas of Fatigue Curvers, American Society of Materials, 1986, p. 10.

[98] J. Li, "The Effect of Microstructure and Texture on High Cycle Fatigue Properties of Al Alloys," University of Kentucky Doctoral Dissertations. 522, 2007.

[99] M. Tsushida, K. Shikada, H. Kitahara, S. Ando and H. Tonda, "Relationship between Fatigue Strength and Grain Size in AZ31 Magnesium Alloys," Materials Transactions 49, pp. 1157-1161, 2008.

[100] Y. Uematsu, K. Tokaji, K. Fujiwara, Y. Tozaki and H. Shibata, "Fatigue behaviour of cast magnesium alloy AZ91 microstructurally modified by friction stir processing," Fatigue and Fracture of Engineering Materials and Structures, vol. 32, no. 7, pp. 541-551, 2009.

[101] A. International, "ASTM E466 - 15: Standard Practice for Conducting Force Controlled Constant Amplitude Axial Fatigue Tests of Metallic Materials," ASTM International, 2015.

[102] S. Chainarong, P. Muangjunburee and S. Suthummanon, "Friction Stir Processing of SSM356 Aluminium Alloy," Procedia Engineering, vol. 97, pp. 732-740, 2014.

[103] H. J. Liu, H. Fujii and K. Nogi, "Microstructure and mechanical properties of friction stir welded joints of AC4A cast aluminium alloy," Materials Science and Technology, vol. 20, pp. 399-402, 2004.

[104] P. Asadi, M. K. B. Givi and M. Akbari, "Simulation of dynamic recrystallization process during friction stir welding of AZ91 magnesium alloy," The International Journal of Advanced Manufacturing Technology, vol. 83, no. 1-4, pp. 301-311, 2016.

[105] G. K. Padhy, C. S. Wu and S. Gao, "Friction stir based welding and processing technologies - processes, parameters, microstructures and applications: A review," Journal of Material Science & Technology, vol. 34, no. 1, pp. 1-38, 2018.

[106] G. K. Padhy, C. S. Wu, S. Gao and L. Shi, "Local microstructure evolution in friction stir weld nuggets of 6061-T6 alloy enhanced by ultrasonic energy," Mater. Des., vol. 92, pp. 710-723, 2016.

[107] G. K. Padhy, C. S. Wu and S. Gao, "Subgrain formation in ultrasonic enhanced friction stir welding of aluminium alloy," Mater. Des., vol. 183, pp. 34-39, 2016.

[108] G. K. Padhy, C. S. Wu and S. Gao, "Improved microstructure in ultrasonic vibration enhanced FSW," Mater. Des. , vol. 116, pp. 207-218, 2017.

[109] S. Gourdet and F. Montheillet, "A model of continuous dynamic recrystallization," Acta Mater., vol. 51, pp. 2685-2699, 2003.

[110] R. Fonda and K. Knipling, "Texture development in friction stir welds," Sci. Technol. Weld. Join., vol. 16, no. 4, pp. 288-294, 2011.

[111] R. Fonda, J. Bingert and K. Colligan, "Development of grain structure during friction stir welding," Scr. Mater., vol. 51, no. 3, pp. 243-248, 2004.

[112] P. Prangnell and C. Heason, "Grain structure formation during friction stir welding observed by the ‘stop action technique’," Acta Mater., vol. 53, no. 11, pp. 3179-3192, 2005.

[113] B. Heinz and B. Skrotzki, "Characterization of a friction-stir-welded aluminum alloy 6013," Metall. Mater. Trans. B , vol. 33, no. 3, pp. 489-498, 2002.

[114] W. Arbegast and P. Hartley, "Friction Stir Weld Technology Development at Lockheed Martin Michoud Space System - An Overview," in Proceedings of the Fifth International Conference on Trends in Welding Research, Pine Mountain, GA, USA, June 1-5, 1998..

[115] T. Sakai, A. Belyakov, R. Kaibyshev, H. Miura and J. Jonas, "Dynamic and post-dynamic recrystallization under hot, cold and severe plastic deformation conditions," Progress in Materials Science, vol. 60, pp. 130-207, 2014.

[116] A. Ozer, A. Sik, B. Cevik and M. Ozer, "The effect of friction stir welding parameters on microstructure and fatigue strength of CuZn37 brass alloys," Kovove Mater., vol. 55, no. 2, pp. 107-114, 2017.

[117] P. Mashinini, D. Hattingh and H. Lombard, "Influence of Process Heat Input on Static and Dynamic Properties of Friction Stir Welded 3mm Ti6Al4V Alloy," Advanced Materials Research, vol. 1019, pp. 287-293, 2014.

[118] A. P. Gerlich and T. Shibayanagi, "Liquid film formation and cracking during friction stir welding," Science and Technology of Welding and Joining, vol. 16, no. 4, pp. 295-299, 2011.

[119] U. Alfaro-Mercado and G. Biallas, "Incipient Melting and Corrosion Properties of Friction Stir Welded AA2024-T3 Joints," in Proceedings of the 12th International Conference on Aluminum Alloys, Yokohama, Japan, September 5-9, 2010.

[120] K. Hassan, P. Prangnell, A. Norman, D. Price and S. Williams, "Effect of welding parameters on nugget zone microstructure and properties in high strength aluminium alloy friction stir welds," Science and Technology of Welding and Joining, vol. 8, no. 4, pp. 257-268, 2003.

[121] Y. Li, F. Qin, C. Liu and Z. Wu, "A Review: Effect of Friction Stir Welding on Microstructure and Mechanical Properties of Magnesium Alloys," Metals, vol. 7, no. 12, p. 524, 2017.

[122] M. Razmpoosh, A. Zarei-Hanzaki and A. Imandoust, "Effect of the Zener–Hollomon parameter on the microstructure evolution of dual phase TWIP steel subjected to friction stir processing," Materials Science and Engineering A, vol. 368, pp. 15-19, 2015.

[123] R. Henson, "Analysis of variance (ANOVA). In W. Arthur Toga (Ed.)," Brain Mapping: An Encyclopedic Reference, vol. 1, pp. 477-481, 2015.

[124] S. F. Sawyer, "Analysis of Variance: The Fundamental Concepts," Journal of Manual & Manipulative Therapy, vol. 17, no. 2, pp. 27-38, 2009.

[125] D. Montgomery, Design and analysis of experiments, New York: John Wiley & Sons, 2013.

[126] B. Li, Y. Shen and W. Hu, "The study of defects in aluminium 2219-T6 Thick butt friction stir welds with the application of multiple nondestructive Testing methods," Materials and Design, vol. 32, pp. 2073-2084, 2011.

[127] G. Bussu and P. Irving, "The role of residual stress and heat affected zone properties on fatigue crack propagation in friction stir welded 2024-T351 aluminium joints," Int. J. Fatigue, vol. 25, no. 1, p. 77, 2003.

[128] K. Jata, K. Sankaran and J. Ruschau, "Friction-stir welding effects on microstructure and fatigue of aluminum alloy 7050-T7451," Metall. Mater. Trans. A, vol. 31, p. 2181, 2012.

[129] P. Pao, S. Gill, C. Feng and K. Sankaran, "Corrosion-FatigueCrack Growth in Friction Stir Welded Al 7050," Scripta Mater., vol. 45, p. 605, 2001.

[130] R. Kapoor, K. Kandasamy, R. Mishra, J. Baumann and G. Grant, "Effect of friction stir processing on the tensile and fatigue behaviour of a cast A206 alloy," Materials Science and Engineering A, vol. 561, pp. 159-166, 2013.

[131] H. Nelaturu, S. Jana, R. S. Mishra, G. Grant and B. E. Carlson, "Influence of friction stir processing on the room temperature fatigue cracking mechanisms of A356 aluminum alloy," Materials Science and Engineering: A, vol. 716, pp. 165-178, 2018.

[132] M. Haghshenas, M. Gharghouri, V. Bhakhri, R. Klassen and A. Gerlich, "Assessing residual stresses in friction stir welding: neutron diffraction and nanoindentation methods," Int J Adv Manuf Technol., vol. 93, no. 9-12, pp. 3733-3747, 2017.

[133] S. Rajakumar, C. Muralidharan and V. Balasubramanian, "Establishing empirical relationships to predict grain size and tensile strength of friction stir welded AA 6061-T6 aluminium alloy joints," Transactions of Nonferrous Metals Society of China, vol. 20, no. 10, pp. 1863-1872, 2010.

[134] M. A. Mohamed and Y. H. Manurung, "Effect of Friction Stir Welding Parameters on Fatigue Resistance, Weld Quality and Mechanical Properties of Al 6061-T651," Journal of Mechanical Engineering SI 2, vol. 2, no. 1, pp. 83-99, 2017.

[135] T. Gurney, "Some comments on fatigue design rules for offshore structures,," in Proc. 2nd International Symposium on Integrity of Offshore Structures, Barking, Essex, England, 1981.

[136] H. Patel, "Cyclic Deformation of Semi-solid Processed Magnesium Alloys," Theses and dissertations. Paper 1471, Toronto, Ontario, Canada, 2010.

[137] M. Pokova and M. Cieslar, "Recrystallization of AA3003 Aluminum Alloy After ECAP During Isothermal Annealing," in Metal 2014, Brno, Czech Republic,, 2014.

[138] S. Aktarer, D. Sekban, O. Saray, T. Kucukomeroglu, Z. Ma and G. Purcek, "Effect of two-pass friction stir processing on the microstructure and mechanical

properties of as-cast binary Al–12Si alloy," Materials Science & Engineering A, vol. 636, pp. 311-319, 2015.

[139] D. H. Choi, Y. H. KIM, B. W. Ahn, Y. I. Kim and S. B. Jung, "Microstructure and mechanical property of A356 based composite by friction stir processing," Trans. Nonferrous Met. Soc. China, vol. 23, pp. 335-340, 2013.

[140] AZoM, "Spheroidizing – Metallurgical Processes," AZO Materials, 26 Aug. 2013. [Online]. Available: https://www.azom.com/article.aspx?ArticleID=9708.

[141] S. Meenia, F. MD, S. Babu, R. Immanuel, S. Panigrahi and G. J. Ram, "Particle refinement and fine-grain formation leading to enhanced mechanical behaviour in a hypo-eutectic Al–Si alloy subjected to multi-pass friction stir processing," Materials Characterization, vol. 113, pp. 134-143, 2016.

[142] A. Schanema, "The effects of prior microstructure on spheroidizing," Colorado School of Mines, Golden, CO, 2009.

[143] S. Jana, R. Mishra, J. Baumann and G. Grant, "Effect of stress ratio on the fatigue behavior of a friction stir processed cast Al-Si-Mg alloy," Scripta Materialia, vol. 61, no. 10, pp. 992-995, 2009.

[144] P. Guru, F. Khan, S. Panigrahi and G. Ram Janaki, "Enhancing strength, ductility and machinability of a Al–Si cast alloy by friction stir processing," Journal of Manufacturing Processes, vol. 18, pp. 67-74, 2015.

[145] D. Klobčar, A. Nagode, A. Smolej and J. Tušek1, "FSW of aluminium alloy AlSi12," RMZ – M&G, vol. 60, pp. 183-189, 2013.

[146] S. Tutunchilar, M. B. Givi, M. Haghpanahi and P. Asadi, "Eutectic Al–Si piston alloy surface transformed to modified hypereutectic alloy via FSP," Materials Science and Engineering: A, vol. 534, pp. 557-567, 2012.

[147] P. Pao, E. Lee, C. Feng, H. Jones and D. Moon, in K.V. Jata, M.W. Mahoney, R.S. Mishra, S.L. Semiatin, T.Lienert (Eds.), Friction Stir Welding and Processing II, TMS, Warrendale, PA, USA, 2003.